PHYSICAL REVIEW ACCELERATORS AND BEAMS **27,** 084802 (2024)

Review Article

The Continuous Electron Beam Accelerator Facility at 12 GeV

P. A. Adderley,[1] S. Ahmed,[1,k] T. Allison,[1,c] R. Bachimanchi,[1] K. Baggett,[1] M. BastaniNejad,[1]
B. Bevins,[1] M. Bevins,[1] M. Bickley,[1] R. M. Bodenstein,[1] S. A. Bogacz,[1] M. Bruker,[1]
A. Burrill,[1,l] L. Cardman,[1] J. Creel,[1] Y.-C. Chao,[1,a] G. Cheng,[1] G. Ciovati,[1,2]
S. Chattopadhyay,[1,a,e] J. Clark,[1] W. A. Clemens,[1] G. Croke,[1] E. Daly,[1] G. K. Davis,[1]
J. Delayen,[1,2] S. U. De Silva,[1,2] M. Diaz,[1] R. Dickson,[1,b] L. Doolittle,[1,f] D. Douglas,[1]
M. Drury,[1] E. Feldl,[1] J. Fischer,[1] A. Freyberger,[1,g] V. Ganni,[1,h] R. L. Geng,[1]
C. Ginsburg,[1,g] J. Gomez,[1] J. Grames,[1] J. Gubeli,[1] J. Guo,[1] F. Hannon,[1,d] J. Hansknecht,[1]
L. Harwood,[1] J. Henry,[1] C. Hernandez-Garcia,[1] T. Hiatt,[1] D. Higinbotham,[1] S. Higgins,[1]
A. S. Hofler,[1] J. Hogan,[1] C. Hovater,[1] A. Hutton,[1] C. Jones,[1] K. Jordan,[1] M. Joyce,[1]
R. Kazimi,[1] M. Keesee,[1] M. J. Kelley,[1] C. Keppel,[1] A. Kimber,[1,c] L. King,[1] P. Kjeldsen,[1]
P. Kneisel,[1] J. Kowal,[1] G. A. Krafft,[1,2] G. Lahti,[1] T. Larrieu,[1] R. Lauze,[1] C. Leemann,[1]
R. Legg,[1,l] R. Li,[1] F. Lin,[1,b] D. Machie,[1] J. Mammosser,[1,b] K. Macha,[1] K. Mahoney,[1,b]
F. Marhauser,[1,m] B. Mastracci,[1] J. Matalevich,[1] J. McCarter,[1] M. McCaughan,[1]
L. Merminga,[1,a] R. Michaud,[1] V. Morozov,[1,b] C. Mounts,[1] J. Musson,[1] R. Nelson,[1] W. Oren,[1]
R. B. Overton,[1] G. Palacios-Serrano,[1] H.-K. Park,[1,a] L. Phillips,[1] S. Philip,[1] F. Pilat,[1,b]
T. Plawski,[1] M. Poelker,[1] P. Powers,[1] T. Powers,[1] J. Preble,[1] T. Reilly,[1] R. Rimmer,[1]
C. Reece,[1] H. Robertson,[1] Y. Roblin,[1] C. Rode,[1] T. Satogata,[1,2] D. J. Seidman,[1]
A. Seryi,[1,2] A. Shabalina,[1,i] I. Shin,[1,3,j] C. Slominski,[1] R. Slominski,[1] M. Spata,[1] D. Spell,[1]
J. Spradlin,[1] M. Stirbet,[1] M. L. Stutzman,[1] S. Suhring,[1] K. Surles-Law,[1] R. Suleiman,[1]
C. Tennant,[1] H. Tian,[1] D. Turner,[1] M. Tiefenback,[1] O. Trofimova,[1] A.-M. Valente,[1]
H. Wang,[1] Y. Wang,[1] K. White,[1,b] C. Whitlatch,[1] T. Whitlatch,[1] M. Wiseman,[1]
M. J. Wissman,[1] G. Wu,[1,a] S. Yang,[1] B. Yunn,[1] S. Zhang,[1] and Y. Zhang[1,*]

[1] *Thomas Jefferson National Accelerator Facility, Newport News, Virginia 23606, USA*
[2] *Department of Physics, Center for Accelerator Science,*
Old Dominion University, Norfolk, Virginia 23529, USA
[3] *Department of Physics, University of Connecticut, Storrs, Connecticut 06269, USA*

(Received 8 November 2023; accepted 1 May 2024; published 15 August 2024; corrected 13 September 2024)

This review paper describes the energy-upgraded Continuous Electron Beam Accelerator Facility (CEBAF) accelerator. This superconducting linac has achieved 12 GeV beam energy by adding 11 new high-performance cryomodules containing 88 superconducting cavities that have operated cw at an average accelerating gradient of 20 MV/m. After reviewing the attributes and performance of the previous 6 GeV CEBAF accelerator, we discuss the upgraded CEBAF accelerator system in detail with particular attention paid to the new beam acceleration systems. In addition to doubling the acceleration in each linac, the

---

[*] krafft@jlab.org
[a] Present address: Fermi National Accelerator Laboratory, Batavia, IL 60510, USA.
[b] Present address: Oak Ridge National Laboratory, Oak Ridge, TN 37830, USA.
[c] Present address: European Spallation Source, Lund, Sweden.
[d] Present address: Phase Space Tech, Lund, Sweden.
[e] Present address: Northern Illinois University, DeKalb, IL 60115, USA.
[f] Present address: Lawrence Berkeley National Laboratory, Berkeley, CA 94720, USA.
[g] Present address: U.S. Department of Energy, Germantown, MD 20874, USA.
[h] Present address: Facility for Rare Isotope Beams, Michigan State University, East Lansing, MI 48824, USA.
[i] Present address: Daresbury Laboratory, Warrington, WA4 4AD, United Kingdom.
[j] Present address: Institute of Basic Science, Daejeon, 34047, Republic of Korea.
[k] Present address: ANSYS.
[l] Present address: xLight Inc., Palo Alto, CA 94306, USA.
[m] Present address: Belgian Nuclear Research Centre - SCK CEN, 2400 Mol, Belgium.

upgrade included improving the beam recirculation magnets, adding more helium cooling capacity to allow the newly installed modules to run cold, adding a new experimental hall, and improving numerous other accelerator components. We review several of the techniques deployed to operate and analyze the accelerator performance and document system operating experience and performance. In the final portion of the document, we present much of the current planning regarding projects to improve accelerator performance and enhance operating margins, and our plans for ensuring CEBAF operates reliably into the future. For the benefit of potential users of CEBAF, the performance and quality measures for the beam delivered to each of the experimental halls are summarized in the Appendix.

DOI: 10.1103/PhysRevAccelBeams.27.084802

I. INTRODUCTION

During the years 1986–1995, the Continuous Electron Beam Accelerator Facility (CEBAF) was built in Newport News, Virginia, USA, supporting research in nuclear physics. The main unique features of this accelerator are the combination of 100% duty factor with high average beam current but low bunch charge, very high-quality electron beam, and high energy, permitting coincident electron scattering and photon induced reactions probing both nuclear and nucleon structure. CEBAF was the first large-scale deployment of superconducting rf beam acceleration and the first large-scale application of multipass beam recirculation [1]. Although originally designed to achieve 4 GeV, by 2009, CEBAF produced beam energies of 6 GeV, allowing world-class electron scattering experiments to be performed in three experimental halls.

In the three decades since the original design parameters of CEBAF were defined, the understanding of the behavior of strongly interacting matter has evolved significantly, and important new classes of experimental questions have been identified that can be addressed optimally by a CEBAF-type accelerator at higher energy. The original design of the facility, coupled with developments in superconducting rf technology, made it feasible to double CEBAF's beam energy to 12 GeV in a cost-effective manner, providing a new research tool capable of addressing the science. The science motivating the 12 GeV Upgrade included breakthrough programs launched in four main areas [2]: (i) probing potential new physics through high precision tests of the Standard Model using precision, parity-violating electron scattering experiments; (ii) discovering the quark structure of nuclei and identifying hidden flavors; (iii) understanding the spin and flavor dependence of valence parton distributions; and (iv) by measuring generalized parton distributions with high precision, discovering the three-dimensional structure of nuclei.

In addition, this project was exciting as it allows one to experimentally study the physical origins of quark confinement. A theoretical explanation, supported by lattice QCD calculations, is that quark confinement stems from the formation of a stringlike "flux tube" between quarks. This idea, and the proposed mechanisms for flux tube formation, can be tested by determining the spectrum of the gluonic excitations of mesons, sometimes referred to as "hybrid" mesons. In order to provide the requisite excitation energy, the most basic requirement of the new project was to achieve 12 GeV electron beam energy after 5 $1/2$ passes through the recirculated linacs. The beam generated photons in a new experimental hall, allowing here-to-fore impossible experiments in precision QCD spectroscopy to be performed. The major construction of the accelerator upgrade to 12 GeV was completed in a 6-month shutdown at the end of 2011 and a long shutdown throughout 2013. Since 2016, nuclear physics experiments at the higher beam energy have been performed. For reference, tables giving the beam performance requirements for the delivery of beam to each of the experimental halls is found in the Appendix.

This paper begins with a review of the main technical features of the accelerator as it was configured and operated in the 6 GeV era. The main body of the paper consists of technical descriptions of the upgrades to the accelerator allowing CEBAF to operate at 12 GeV. In the following sections, we present information about the accelerator performance in the new configuration, as well as a review of some of the significant technical systems allowing the recirculated linacs to operate properly and with high efficiency. We conclude with a forward-looking discussion on CEBAF's future.

II. 6 GEV CEBAF

Before the upgrade activity, CEBAF was a five-pass, recirculating cw electron linac operating at up to 6 GeV. The layout appears in Fig. 1 and Table I summarizes the principal accelerator parameters.

Beams of high average current up to 200 μA with 90% polarization, of low geometric emittance less than 10^{-9} m rad and of low relative momentum spread less than 3×10^{-5}, were produced. By combining five-pass recirculation, a three-laser photocathode source and subharmonic-rf-separator-based extraction, three beams at different energies could simultaneously be delivered to three end stations (halls A, B, and C). The operating hall-to-hall current ratios could approach 10^6 and the beam delivered with a specified orientation of the beam polarization. The linacs were built up from cryomodules, each of which contained eight CEBAF/Cornell [3] five-cell superconducting rf (SRF) cavities. Originally designed as a four-pass 4 GeV recirculating linac

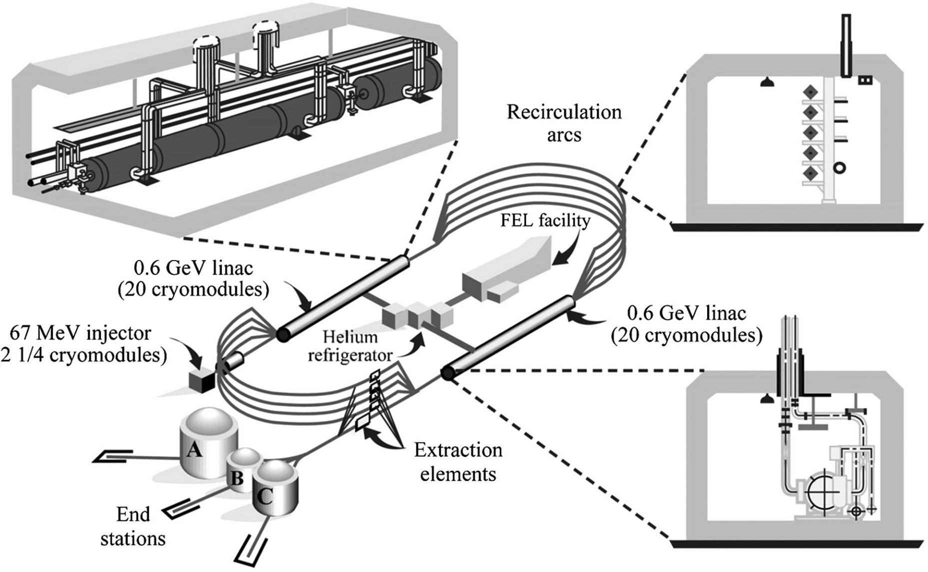

FIG. 1. Schematic of the 6 GeV CEBAF (from [1]).

with 50 cryomodules [4], five-pass recirculation with 40 cryomodules was adopted as a cost control and optimization measure in 1988. Because the CEBAF tunnel layout and construction had already started, during the 6 GeV era, five cryomodule slots in each linac were left vacant. These slots were filled with high-performance cryomodules as part of the upgrade.

TABLE I. Principal parameters for CEBAF in the 6 GeV era (from [1]).

Energy	6 GeV
Average current (halls A and C)	1–150 μA
Average current (hall B)	1–100 nA
Bunch charge	<0.3 pC
Repetition rate	499 MHz at hall
Beam polarization	90%
Beam size (rms transverse)	~80 μm
Bunch length (rms)	300 fs, 90 μm
Energy spread	2.5×10^{-5}
Beam power	<1 MW
Beam loss	<1 μA
Number of passes	5
Number of accelerating cavities	338
Fundamental mode frequency	1497 MHz
Accelerating cavity effective length	0.5 m
Cells/cavity	5
Average Q_0	4.0×10^9
Implemented Q_{ext}	5.6×10^6
Cavity impedance (R/Q)	480 Ω
Average cavity accelerating gradient	7.5 MV/m
rf power	<3.5 kW/cavity
Amplitude control	1×10^{-4}
Phase control	0.1° rms
Cavity operating temperature	2.1 K
Liquifier 2 K cooling power	5 kW
Liquifier operating power	5 MW

A. Design summary

Many considerations went into the design of CEBAF. For example, increased siting flexibility of the more compact design and cost drove the decision to deploy two antiparallel linacs instead of one long linac. Many of CEBAF's features derived from the high cost of superconducting beam acceleration. In order to take maximum advantage of the accelerating gradient possible from each cavity, CEBAF was run as a linac, with the electron bunches close to the peak of the accelerating voltage. This possibility exists because phase focusing was not needed for the highly relativistic beam, but this choice implies that the recirculation arcs be designed to be isochronous ($M_{56} < 10$ cm). The pass-to-pass requirement for phase control dictated that the recirculation path length be within 100 μm of an integer number of rf wavelengths. In practice, this requirement was accomplished by measuring the path length (see Sec. IV C 4) and varying the path through individual "path length" chicanes placed in each recirculation arc.

Vertical stacking of the various energy beamlines was chosen largely for practical reasons. Vertical dispersion was introduced, and the choice must be made between constructing individually achromatic vertical bends or correcting vertical dispersion only at the end of the complete arc. At CEBAF, the vertical dispersion was corrected locally [5]. This choice made operational, real-time analysis of beam behavior through the arcs as transparent as possible and avoids vertical phase space growth driven by synchrotron radiation. For the same reasons, a philosophy of functional modularity in the optics design was adopted, resulting in the following breakdown of transport sections from linac to linac [5,6]: achromatic vertical bend to separate different energies, matching section, 180° horizontal achromatic bend based on a regular lattice operated with matched beam-envelope functions, matching section, achromatic vertical bend back to linac level, with the whole system globally isochronous. The two matching sections downstream of the linacs were long, one containing path length-adjusting doglegs, the other containing doglegs and beam extraction elements, while the matching regions immediately upstream of the linac sections were short and had no additional functions.

A decision was made to keep the recirculation arc radii large enough to allow later upgrades in energy by avoiding excessive degradation of beam emittance and energy spread from synchrotron radiation. Magnets were designed as low-field, low-current-density devices to minimize power consumption. As a consequence, the 6 GeV beam transport system could be upgraded to 12 GeV by merely replacing power supplies, increasing the saturated field strength in the recirculation arc dipoles, and exchanging a small number of other magnets. With a completely new lattice and magnets, the arc tunnel radius is large enough to allow a future upgrade to about 25 GeV [1,7].

Operating the three end stations simultaneously was a desideratum, and with the use of multipass beam recirculation, additional degrees of freedom became available to achieve this goal. Three-beam operation was implemented by creating three interlaced 499 MHz beams at the source. The bunches going to each of the separate halls were spaced apart by 120° of rf phase at 499 MHz. Together, they form a 1497 MHz beam in which each bunch has properties, particularly charge, that may differ from its immediately preceding and trailing pair of neighbors, but which repeated every third bunch. Such a current profile was achieved by using three independent rf-gain-switched lasers [8,9] directed at a single photocathode, each laser with a third subharmonic 499 MHz bunch repetition frequency.

Extracting the beams to each of the three end stations was achieved by using properly phased rf deflecting cavities ("rf separators") operating at 499 MHz. For example, rf separators were installed in the various recirculation paths downstream of each full pass making it possible to serve different halls simultaneously with beams of different but correlated energies. In addition, distributing three full-energy beams at the same time was possible using a single separator located after the fifth pass through the accelerator. In contrast to the cylindrically symmetrical rf deflector designs available at the time, the Jefferson Lab separators were ahead of their time in being fully three dimensional [10].

B. CEBAF injector and its upgrade

The CEBAF photoinjector provided independent beam delivery of spin-polarized electron beams to each experiment hall simultaneously over a wide range of requested current: from 100 pA to 180 μA. The design of the CEBAF injector was based on an injector for a microtron accelerator [11,12], and CEBAF's injector design and layout [12,13] have not changed materially since the injector was initially installed for 4 GeV CEBAF. The injector started with a dc electron gun producing electrons that are transported to a chopper system. The chopper system constrained the longitudinal beam extent (bunch length) to ensure proper bunching is initiated in a downstream single-cell reentrant rf cavity (buncher). Next, a five-cell side-coupled graded-beta rf cavity (capture section) accelerated the bunched beam from the gun energy to 500 keV [12,13]. See Fig. 1 in [14] for a photo and simulation model. A booster (quarter cryomodule) with two 5-cell SRF cavities accelerated the captured beam to 5–6 MeV. Along a 6 m optics transport line, the near relativistic beam continued to drift and bunch while being transported to two full cryomodules, each with eight 5-cell cavities. The full modules accelerated the beam to the required injection energy for the target machine energy. An injection chicane merged the injector beam into the main accelerator [15]. The injector included several spectrometer dump lines for cavity phasing and energy measurements. The initial design proved to be robust and flexible as it has been easily adapted to the increasing demands of the 6 and 12 GeV eras.

During the 6 GeV era, the injector changed in four ways [16–18]. The first was installing the 499 MHz three-beam chopper system, which supported operating three experimental halls concurrently. The second was installing improved full cryomodules capable of accelerating the beam to 67.5 MeV, needed to operate at 6 GeV. The third was transitioning from 100 kV thermionic gun operations [12] to 100 kV polarized source operations. The polarized source was a dc photocathode gun capable of producing three interleaved polarized electron beams at 499 MHz which is thoroughly discussed in the next section [19,20]. The fourth was installing a two-wien and solenoid system to set the spin delivered to the experimental halls. The Wien system was installed between the gun and the chopper system, so the polarized source is further away from the chopper system than in the original injector design. To compensate for bunch lengthening of high current bunches and ensure the polarized electron bunches match the longitudinal acceptance of the chopper system, an additional buncher cavity (prebuncher) was installed between the gun and the chopper system. Also, solenoids between the Wien system and the quarter cryomodule were changed from single-wound to counter-wound solenoids to preserve the spin of the electrons set by the Wien system.

The CEBAF injector was very capable, and considerable effort in the 6 GeV era was dedicated to standardizing the injector setup process to produce the small bunch length, small energy spread, and suitable transverse phase space required for both routine and challenging beam operations to support nuclear physics operations. A summary of the main beam parameters from the injector at the close of the 6 GeV era appears in Table II. Conditions for a CEBAF energy of 6 GeV are assumed.

TABLE II. Principal beam parameters for the CEBAF injector when operating at 6 GeV [1].

Energy	67.5 MeV
Average current (halls A and C)	1–150 μA
Average current (hall B)	0.1–100 nA
Bunch charge	<0.3 pC
Repetition rate	499 MHz at hall
Beam polarization	90%
Transverse beam size (rms)	~500 μm
Beam normalized rms emittance	~0.5 mm mrad
Bunch length (rms)	300 fs, 90 μm
Relative energy spread	1×10^{-3}
Beam longitudinal rms emittance	~20 keV–ps
Number of SRF accelerating cavities	18

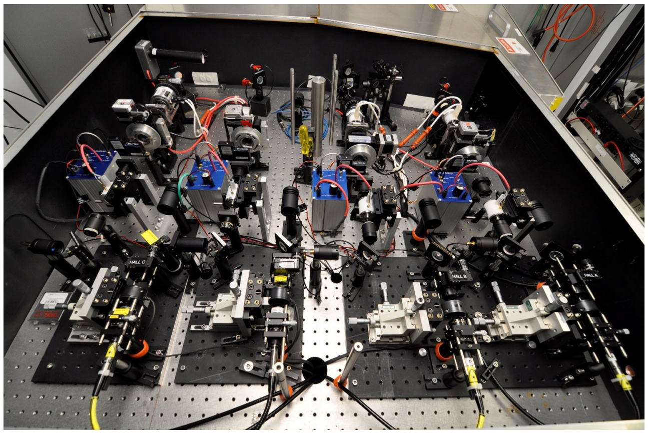

FIG. 2. Photograph of the four-laser system used to create interleaved electron beams, one laser for each experiment hall. Laser beams are combined using partially reflective mirrors and polarization-sensitive optical elements.

1. Injector improvements for 12 GeV CEBAF

Most components of the 12 GeV CEBAF photoinjector are located as in the 6 GeV CEBAF photoinjector, but the layouts of the injection chicane and full energy injector spectrometer are adjusted to accommodate the new beamline that is part of the upgrade. The main improvements to the injector are as follows: (i) to increase the gun voltage to 130 kV dc, (ii) to increase the overall injector energy capability to 123 MeV [21], and (iii) to add a fourth drive laser and required rf equipment to allow four beams to be produced simultaneously, for delivery to four experiments. Here, we briefly discuss the changes. More detail will be found in the referenced sections in the main body of this paper.

The first change reduces space charge effects and results in more consistent beam setups in cases when the bunch charge to the different halls is very different (e.g., when the hall B charge is 0.01 fC provided simultaneously with 0.2 pC to hall A). It is the first step in a longer term project to achieve 200 kV electron kinetic energy from the gun, described in greater detail in Sec. V C.

The second change follows directly from the desire to have the beam on the same orbits at 12 GeV as it had operating at 6 GeV. For this desire to be achieved, throughout CEBAF, the beam energies in the various passes and arcs must be at nearly the same energy ratios. In the 12 GeV CEBAF design, when hall D is operating at 12 GeV, the maximum beam energy to the original halls A–C is 10.9 GeV. Therefore, the beam energy at injection must be scaled up by a factor of 1.82 (10.9/6) going from 6 GeV in halls (A–C) to 12 GeV in hall D or from 67.5 to 123 MeV. Such an energy increase is comfortably accomplished by replacing the final cryomodule in the injector with a cryomodule of the new upgrade design. As discussed in Sec. III A 3, the specific new cryomodule in the injector, called "R100" [22], is built with capabilities largely equivalent to the cryomodules placed in the linacs for the upgrade. Because there is no recirculation in the injector, the rf power required to accelerate the beam load in the injector is much less than in the main linacs, meaning the rf systems driving the R100 can be largely reused after the upgrade.

Third, a major difference between the 6 and 12 GeV CEBAF photoinjectors is that now four halls can receive beams simultaneously instead of just three. This upgrade is accomplished by adding a fourth drive laser (Fig. 2) and by modifying the extraction/separator system [23]. Whereas during 6 GeV CEBAF operation, interleaved laser pulse trains at 499 MHz were used, now lasers can operate at 249.5 MHz, the sixth subharmonic of 1497 MHz. Interleaved pulse trains at 249.5 MHz permit simultaneous four-hall operation, albeit with "empty buckets" that pose no problems for the nuclear physics program (Fig. 3). The required modifications to the rf extraction/separator system are described further in Sec. III H.

C. Polarized source and polarization to halls

All polarized beams originate from a single photocathode inside a dc high voltage photogun biased at 130 kV [25]. Successful uninterrupted production of polarized electron beams requires expertise with GaAs-based photocathodes,

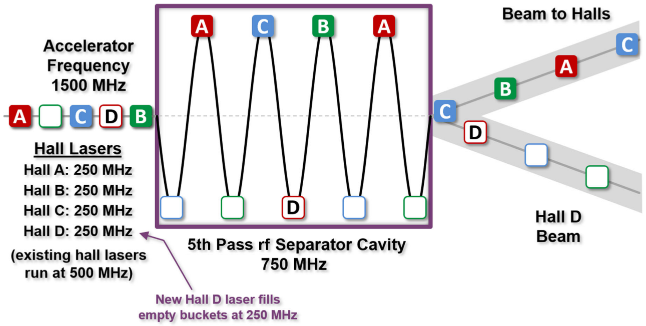

FIG. 3. Schematic showing how beams are interleaved, separated, and delivered to each experiment hall (from [24]).

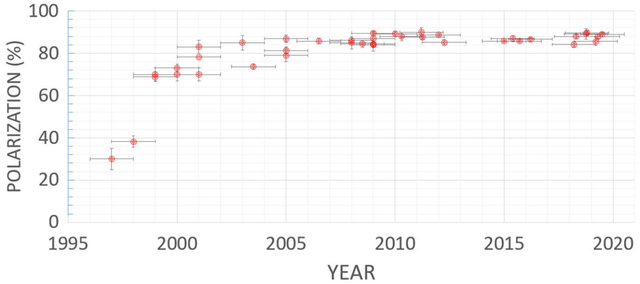

FIG. 4. Evolution of beam polarization provided to experiment halls at CEBAF using three different types of photocathodes: bulk GaAs, strained GaAs/GaAsP, and strained superlattice GaAs/GaAsP.

high voltage, ultrahigh vacuum, and drive laser technology. Over more than two decades, a wide variety of technologies and improvements have been implemented to improve beam quality and decrease downtime.

1. Polarized electron source

Bulk GaAs is very inexpensive and provides very high quantum efficiency (QE), but unfortunately, polarization is just 35% [26] due to degenerate energy levels in the valence band. The nuclear physics program benefits from significantly higher polarization obtained by introducing an axial strain within the GaAs crystal lattice, accomplished by growing GaAs on a substrate with different lattice constants [27]. The evolution of beam polarization at CEBAF is shown in Fig. 4, where over the span of 23 years, beam polarization has increased from 35% to 90%, with beams produced today using a strained-layer GaAs/GaAsP superlattice photocathode [28]. New photocathodes including the strained-layer GaAs/GaAsP superlattice photocathode grown atop a distributed Bragg reflector [29] and strained-layer GaAs/GaAsP superlattice photocathode manufactured using a nanopillar array [30,31] promise high polarization but with significantly higher QE that is needed for proposed high current applications, such as polarized positron generation [32].

One of the biggest obstacles to successful polarized beam production is field emission and high voltage breakdown within the dc high voltage photogun. Field emission at even picoAmpere levels [33] can degrade the photogun operating lifetime. A photogun with inverted-insulator geometry provides the electron beams at 12 GeV CEBAF [25]. With this design, there is no exposed high voltage because the ceramic insulator extends into the vacuum chamber and serves as the support structure for the cathode electrode in which the photocathode is housed. This design helps to minimize the amount of metal biased at high voltage, which in turn helps to minimize field emission. Another innovation employed at Jefferson Lab relates to electrode polishing. To prevent field emission and breakdown, electrodes must possess an extremely smooth surface free of embedded contamination. Electrodes are no longer polished by hand using diamond paste, which is a very laborious and time-consuming process. Now, electrodes are barrel polished, with a smooth surface achieved in only hours [34].

The operating lifetime of the photocathode is limited by ion bombardment, the process whereby residual gas becomes ionized by the extracted electron beam, with ions attracted to the negatively biased photocathode. Ions that bombard the photocathode can sputter away the thin layer of chemicals applied to the surface used to create the required negative electron affinity condition, or they can become implanted within the photocathode material reducing the electron diffusion length [35]. The best way to minimize ion bombardment is to operate the photogun under the best vacuum conditions possible. At 12 GeV CEBAF, this is accomplished using a photogun with load-lock design, where photocathode heating and activation steps are performed outside the photogun high voltage chamber behind a closed valve. In addition, photogun vacuum chamber components are prebaked at 400 °C to reduce material outgassing [36], and some surfaces are coated with nonevaporable getter material to provide distributed pumping [37]. These steps (and others) result in an extremely good photogun vacuum, in the low 10^{-12} torr range, such that hundreds of coulombs of charge can be delivered before the photocathode must be heated and reactivated. Typically once or twice a year the entire photocathode emission area is activated to support physics running and always during planned accelerator down periods.

The drive lasers used to generate interleaved optical pulse trains are composed of 1560 nm gain-switched, fiber-coupled telecom diode lasers followed by fiber amplifiers that produce 35 ps optical pulses at 249.5 or 499 MHz repetition rates. This light is then frequency doubled to produce watts of power at 780 nm [38]. Gain switching is a purely electrical pulse–forming technique that does not depend on the laser optical cavity length. As a result, the optical pulse trains never lose phase lock to the accelerator rf frequency. Although gain-switched lasers possess unique characteristics such as great simplicity, high stability, and easy tuning of frequency and pulse width, their relatively low pulse contrast tends to produce a low level of dc light that complicates beam delivery to experiment halls when operating at low current.

2. Polarization to halls

Parity-violating electron scattering experiments represent one class of physics experiments performed at 12 GeV CEBAF [39] that place challenging demands on the accelerator. These experiments study the parity violation phenomenon or they use the phenomenon to explore the nuclear structure. Since the measured scattering

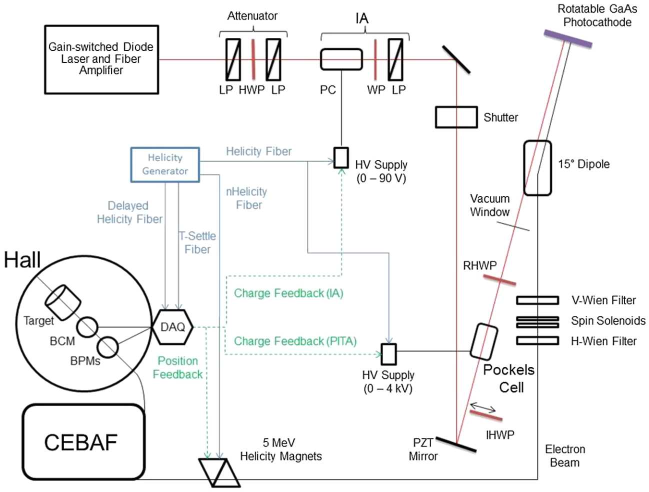

FIG. 5. Schematic diagram showing the devices used to measure helicity-correlated beam asymmetries and the accelerator systems used to minimize these asymmetries with feedback algorithms (LP: linear polarizer, HWP: half-wave plate, PC: pockels cell, WP: waveplate, RHWP: rotatable halfwave plate, IHWP: insertable halfwave plate, IA: charge asymmetry controller, V and H Wien: vertical and horizontal Wien filters, BCM: beam current monitor, BPM: beam position monitor).

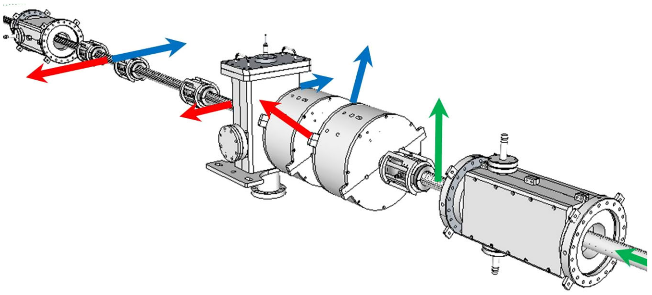

FIG. 6. Schematic view of the 4π spin manipulator used at 12 GeV CEBAF, composed of two Wien filters and intervening spin-rotator solenoids (beam traveling left to right). The colored arrows denote the spin direction after passage through each element.

asymmetries of parity violation experiments are very small (ppm, ppb), it is important that beam properties be identical in the two helicity spin states. Minimizing so-called helicity-correlated beam asymmetries [40] was an important R&D focus for 12 GeV CEBAF and necessary for the successful completion of new, proposed parity-violating electron scattering experiments [41]. All helicity-correlated beam asymmetries originate from the Pockels cell, the electro-optical element used to create circularly polarized laser light which is required to produce polarized electron beams from GaAs-based photocathodes. Charge asymmetry, beam position asymmetry, and beam size asymmetry are the most frequently cited metrics. If the laser light polarization could be made perfectly circular, helicity-correlated beam asymmetries would vanish, but small imperfections in the optical devices on the laser table, and birefringence of the vacuum window through which the laser light passes en route to the photocathode, result in some small amount of linear polarization within the laser light. This residual linearly polarized light combined with the QE anisotropy of the photocathode [28], produces nonzero helicity-correlated beam asymmetries that must be minimized using precise alignment techniques performed at the photoinjector and feedback algorithms that rely on laser table components depicted in Fig. 5. In addition, there are methods to flip the polarization of the electron beam to provide a systematic check on the physics measurement [18].

For electrons leaving the photocathode, the electron spin direction is parallel (antiparallel) to the beam trajectory, but the spin direction rotates in the magnetic field of the arc magnets en route to the experiment halls. Since most polarized-beam experiments require longitudinal polarization at the target, a means to counter this spin precession is required. At 6 GeV CEBAF, a “Z”-style spin manipulator [42] was first employed—it provided full 4π spin rotation capability, but it was composed of many short-focal length elements and was difficult to use in practice. The 12 GeV CEBAF photoinjector employs a “Two Wien” spin manipulator as shown in Fig. 6 [18]. It provides full 4π manipulation of the spin direction but is compact and much easier to use. For parity violation experiments, it provides a comparatively simple means of introducing a 180° spin flip that is required to reduce multiple systematic effects that cannot be directly measured.

A Mott-scattering polarimeter located in the 5 MeV region of the 12 GeV CEBAF photoinjector is used to measure beam polarization (Fig. 7) and provides a valuable cross-check of polarization measurements made at the experiment halls [43]. The polarimeter was recently assigned a level of precision/accuracy by performing the

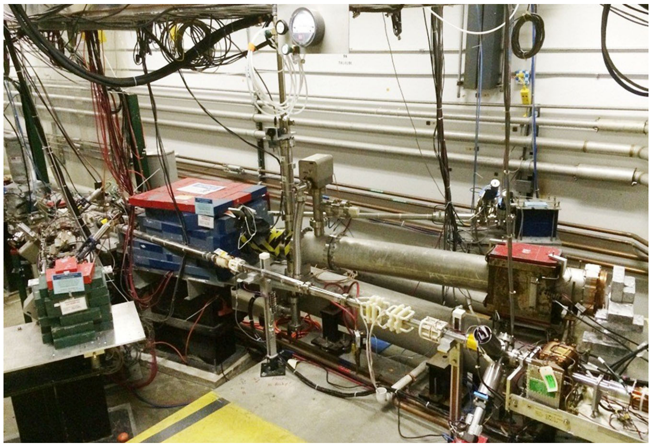

FIG. 7. The 5 MeV Mott-scattering electron polarimeter, positioned between the “straight ahead” beamline leading to the injector linac and a spectrometer beamline.

so-called foil thickness extrapolation, with Mott scattering asymmetries measured from multiple gold target foils of different foil thickness. Extrapolating to "zero thickness" provides a measurement of single-scattering asymmetry which can be compared to theoretical predictions. The statistical precision of the polarimeter is less than 0.25%, with the measured asymmetry unaffected by ±1 mm shifts in the beam position on the target foil and by beam current changes and dead time effects over a wide range of beam currents. The overall uncertainty of a beam polarization measurement at the injector is 0.61% and is dominated by the uncertainty in the foil thickness extrapolation as determined from fits to the measured asymmetries versus foil thicknesses; the estimated systematic effects; and the dominant uncertainty from the calculation of the theoretical Sherman function [44].

What distinguishes CEBAF from almost all other accelerators in terms of beam transport quality is the exacting demand imposed by parity-violation (PV) experiments discussed in Sec. I. These experiments aim to discern tiny asymmetries in scattering cross sections between opposite spin directions, or helicities, of the electron beam and are extremely prone to contamination by false signals from other helicity-dependent inputs, such as beam coordinates (offset and angle) entering the detector. As CEBAF parity-violating experiments probe such asymmetries down to a few ppm, false signals must be controlled to well below this level. Nominally due to phase space conservation, beam coordinate dependence on helicity, originating from the injector at 335 keV/c (momentum), is damped down by about a factor of 100 when it reaches the detector at 3 GeV/c for PV experiments. This effect, known as adiabatic damping, is however realized only if the beam is transported exactly as designed over almost 4 orders of magnitude in momentum. Small deviations from design transport, such as minor coupling or local near singularity tolerable to other applications, can lead to helicity-dependent contamination overwhelming PV signatures. At CEBAF, an initiative was launched to ensure global adherence to design transport for PV experiments across the entire momentum range [45]. Efforts were focused on three fronts: (i) Ensuring close adherence to design transport using existing diagnostic and control provisions from the injector exit to the experimental halls, (ii) installing additional diagnostic and control elements as needed to correct for deviation from the four-dimensional transverse design transport in the injector complex, with special attention to off-diagonal coupling and on-diagonal near singular transport, both of which can translate into gross magnification of helicity-dependent coordinates not correctable at higher energy, and (iii) using a global signal activated with 30 Hz piezo kickers (PZT) from the injector to the experimental halls as an end-to-end tuning guide for real-time global transport correction. It is important to ensure the absence of near singular transport at any point along the entire transport path, as it increases beam sensitivity, complicates correction efforts, and can magnify otherwise benign projected emittance growth beyond repair. Successful execution of this program has eventually resulted in adiabatic damping of helicity-dependent beam coordinates at 3 GeV as expected, and unprecedented precision of CEBAF-based PV experiments, with asymmetry determined to better than 100 ppb in some cases.

D. 6 GeV CEBAF performance summary

At the end of operations at 6 GeV, the CEBAF accelerator performed as designed. In this section of the paper, two specific aspects of the performance of technical systems that were instrumental in achieving the desired performance are summarized.

1. Performance and control of SRF cavities

When CEBAF was originally designed, obtaining 4 GeV from four passes required 1 GeV from $50 \times 8 = 400$ cavities or 2.5 MV per cavity. An SRF cavity modified from one run with a high current beam at Cornell University's CESR collider [3,46] was adopted very early in the CEBAF project [47]. Operating at 1497 MHz and with five 10 cm long elliptical cells, the initial accelerating gradient requirement for the CEBAF accelerating cavities was 5 MV/m, on average. Similarly, in order to fall comfortably within the cooling capacity of a 5 kW (at 2 K) helium cooling plant, the Q_0 requirement for the cavities was 2.4×10^9. At 5 MV/m, each cavity would dissipate 5.4 W of dynamic heat. As an eight-cavity cryomodule was expected to produce at least 20 MV, the cryomodules in the originally installed complement are now known generically as "C20s."

After the transition of CEBAF to five-pass recirculation, the number of linac cavities was reduced from 400 to 320. However, to still achieve 4 GeV beam energy, these basic performance requirements for individual cavities remained unchanged. During the course of the CEBAF project, the installed cavities significantly exceeded the basic requirements, and cavities installed later in the project performed better than those installed earlier. Figure 8 shows a histogram of the installed gradient capability of the initial

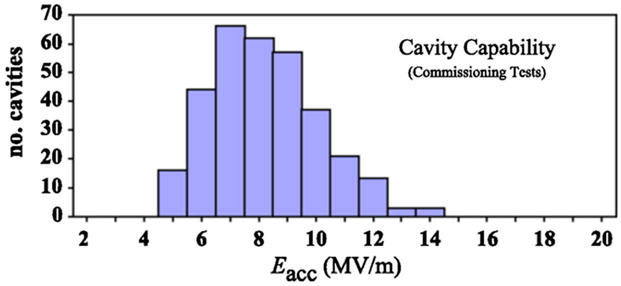

FIG. 8. 6 GeV CEBAF cavity usable gradient after initial complement of cavities installed (from [48]).

complement of CEBAF cavities [48]. The average possible gradient was above 7.5 MV/m, exceeding the project goals by 50%. The average Q_0 of the cavities was also much better than the requirement [48]. Nominally, operating CEBAF above 6 GeV should have been possible. During the years 2001 to 2003, CEBAF was usually run at between 5.5 and 5.8 GeV maximum beam energy, limited by rf trips of the cavities. Presently, 27 of the 40 C20 cryomodules originally installed remain in CEBAF.

The maximum beam current to be delivered to the halls at any one time was 200 μA, and so the maximum beam load in the linacs was 200 × 4 passes = 800 μA in the first project specifications [49]. To minimize the rf power required at this load, the cavity Q_L was specified to be 6.6×10^6, yielding a cavity 3 db bandwidth of 220 Hz. As the maximum anticipated beam load was 2 kW, and margins were required to control against the fluctuations of the cavity resonance frequency away from the rf source frequency (the so-called microphonics), a saturated power of 5 kW for the klystrons was specified. The klystron adopted for CEBAF used a permanent magnet and had a modulating anode. It had four cells so the gain was a modest 40 dB. Cathode voltage and current were typically 11 kV and 1A.

During this early period, the rf controls for CEBAF used analog feedback mated with an x86 Intel processor [50]. As usual at the time, the low-level rf (LLRF) controls were all analog with primitive remote controls. The controls allowed operators to change system gains, observe signals (cavity field, forward and reflected power, etc.), and had built-in health checks. The design used separate phase and amplitude controls, typical for controlling normal conducting (NC) cavities.

The SRF cavities posed new challenges for LLRF control. Unlike NC cavities where the Q_L is much lower, SRF cavities have greatly enhanced susceptibility to any detuning of the cavity frequency, e.g., from microphonics or helium cooling pressure fluctuations. To meet the cavity field control specifications required for the CEBAF LINAC, high feedback gain LLRF controls were needed to suppress the gradient and phase fluctuations produced by detuning. Figure 9 shows a diagram of the CEBAF rf system.

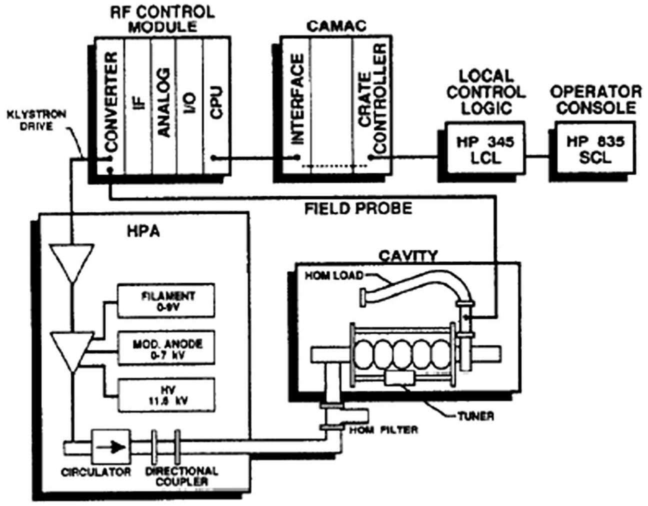

FIG. 9. 6 GeV CEBAF rf system showing cavity, klystron, and controls (from [50]).

One of the modernizations at the time for the rf control system was making it a modular system. The division was made through a crate that supported the different electronic boards. The crate had the following cards, rf, IF (intermediate frequency), analog, digital, and processor board. The rf board converted the cavity frequency from 1497 MHz down to an intermediate frequency (IF) of 70 MHz. The IF board performed the signal processing needed to control phase and amplitude of the cavity. The analog provided separate feedback gain channels for phase and amplitude control, each with the ability to vary the gain. The digital board had analog-to-digital converters, digital-to-analog converters and transistor to transistor logic digital input/output that was used for component on the rf, IF, and analog boards. The digital board talked directly to the processor board which had am 8186 Intel processor. The rf control system communicated through the CAMAC crate with the EPICS controls. Five different control cards made up a C20 LLRF control module [50].

Another novel concept at the time was to calibrate the LLRF system in an automated test stand. All of the rf channels, both receiving and transmitting, were calibrated against a standard reference or power meter. In addition, each LLRF control module was placed inside an environmental chamber and cycled to characterize and correct temperature drifts on its rf channels. rf components were susceptible to both phase and amplitude drifts and the measurements and resulting calculated corrections allowed the LLRF system to operate with minimized drifts [51]. The original LLRF control systems have been very reliable with few issues during their operational life.

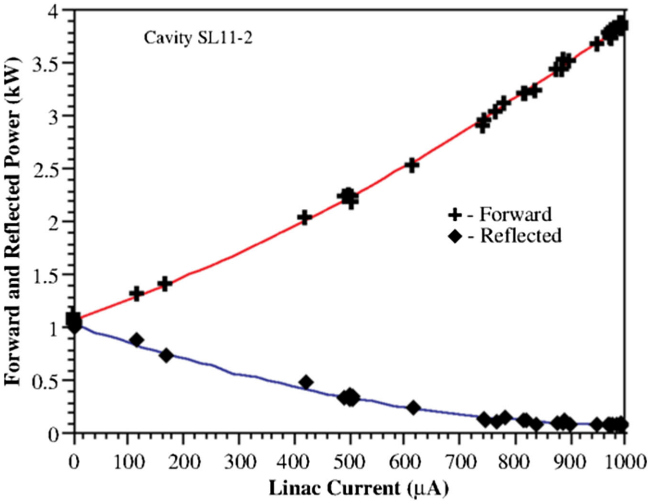

FIG. 10. Forward and reflected power observed in high power beam test in CEBAF (from [52]).

In 1997, CEBAF was run up to the 200 μA maximum cw beam current and demonstrated a full five-pass beam power of 800 kW [47,52]. Figure 10 shows the forward and reflected power measured as a function of beam current in one of the cavities in the South Linac during the test. The cavity was operated at a 6.5 MV/m field gradient accounting for a total five-pass beam load of 3.5 kW. The measurements demonstrated convincingly several significant features of the SRF design: full reflection of the incident rf power at low beam load, near matched beam load at the highest operating current and thus appropriate cavity Q_L, and near unity overall rf to beam conversion efficiency when operating at the matched load.

2. C50 linac improvement program

Starting in 2006, Jefferson Lab initiated a maintenance and upgrade program for cryomodules. The ten worst-performing cryomodules of the original complement were removed and the cavities were reprocessed. The refurbished cryomodules had many improvements: dogleg input waveguide couplers and a revised vacuum window were added which largely eliminated previous gradient limitations due to window charging and arc discharges [53], the Q_L of the input coupler was raised by 20% to 8×10^6 supporting operating at higher accelerating gradient, the mechanical tuners were improved, and any damaged or worn components in the cryomodule were replaced. After the cavities were refurbished, an operating goal of 12.5 MV/m at an increased Q_0 of 6.8×10^9 was established, so an overall energy gain of 50 MV per cryomodule was indicated. Naturally, the cryomodules came to be called “C50s.” After installing the eighth C50 in the spring of 2009, CEBAF could be operated at 6 GeV [54]. The two additional modules served to increase reliability and reduce rf trip rates during 6 GeV operations. Following the end of the official 10-cryomodule C50 program, an 11th C50 module was installed in CEBAF in 2013 and a 12th C50 module was installed in 2019. Only minor changes to the rf drive hardware were made in this program, so at the highest beam loads, the voltage delivered by the C50 cavities had to be lowered.

3. Beam performance

In order to achieve the best beam performance in a CEBAF-like machine, several conditions had to be achieved. As described in the previous section, a beam of appropriate transverse and longitudinal phase space had to be created and injected into the recirculated linacs. Once the bunches were in the linacs, in order to minimize the energy spread of the accelerated bunches, the phase of rf had to be chosen so that the bunches were on the crest of the accelerating wave on the first pass and all subsequent passes. In practice, these conditions were achieved in a two-step process where first the phases of the rf cavities are chosen to maximize the energy after the linacs through a spectrometer measurement, and second, the path lengths of the individual beam passes are adjusted so that the higher pass bunches have the same average rf phase as the first-pass bunch. Spectrometer measurements allow the phase to be set to crest phase to less than a degree (1.9 ps).

The total time for one beam recirculation is 4.2 μs. As described in Sec. IV C 4, by establishing a 4 μs beam macropulse, the phase of the individual higher beam passes was measured using a longitudinal pickup cavity [55] and the path length adjusted so that the pass-to-pass phase difference was under 0.1° (200 fs). By energy modulating the beam, the same type of measurement was used to verify that the individual arcs were isochronous [56].

CEBAF had quadrupoles installed in the warm regions between each cryomodule. Usually, CEBAF was run as a FODO system so that the phase advance through the linacs is constant on the first beam pass through the linac. Therefore, on higher beam passes, the linac beam optics tended to be dominated by free drift optics modulated by the periodicity generated by the linac quadrupoles. Ideally, the beam optical dispersion and its derivative vanished when the beam traverses each beam pass through the linac and at the entrance and exit of each recirculation arc. As discussed in Sec. IV C 1, standard beam optics sets were downloaded into CEBAF, with focusing quadrupoles set proportionally to the beam energy delivered to the experimental hall receiving the highest beam energy.

In CEBAF, the beam optics was verified through a series of toggling measurements [57]. Low average power pulsed beam was established where the beam macropulses are 60 Hz power line synced. For transverse beam optics verifications, air-core magnets were excited with 30 Hz, line-synced current pulses, transversely kicking the beam in both the horizontal and vertical directions at two locations for each direction. The two output locations were measured at all BPMs downstream of the kickers, and the difference orbit so obtained compared to the machine beam optics model. Deviations from the machine model were found when the measured Courant-Snyder invariant for the difference orbit failed to agree with the expectations from the machine model.

Likewise, the dispersion (and implicitly its derivative) was determined simply by modulating the beam energy via the gradient sets in several superconducting cavities, also toggled in a line-synced manner. In this case, the dispersion was simply proportional to the measured difference in orbit. Specific beam optics correction procedures were applied to ensure the dispersion patterns were correct throughout the accelerator.

Early postcommissioning experience [57] revealed serious discrepancies between predictions of the optics model and actual beam displacements in the machine. Major sources of irreproducible behavior in the beam optics were linked to the focusing effects of bending dipoles and several quads exhibiting few percent focusing errors. The effect

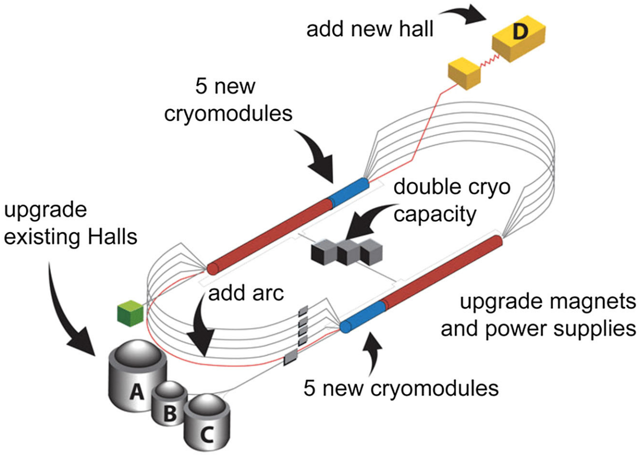

FIG. 11. 12 GeV upgrade project technical scope.

was particularly large for vertical dipoles of the spreaders and the recombiners, which were not measured with sufficient accuracy before installation. Simultaneous fitting of six independent difference orbits by varying the focusing terms of each dipole in the spreaders and recombiners yielded a unique set of body gradients for all dipole magnets. A similar process was performed for the horizontal dipoles of nine arcs. Once understood and corrected, excellent agreement between models and measurements was present throughout 6 GeV running.

III. ELEMENTS OF THE 12 GEV UPGRADE

The 12 GeV upgrade project, a major project sponsored by the DOE Office of Nuclear Physics, substantially expands the research capabilities of CEBAF by doubling the maximum energy and adding a major new experimental apparatus [58]. The technical scope of the upgrade project is illustrated in Fig. 11 and includes doubling the accelerating voltages of the linacs by adding ten new high-performance cryomodules and the rf power systems to support these cryomodules; expanding the 2K cryogenics plant by a factor of 2 as required; upgrading the beam transport system from 6 to 12 GeV through extensive reuse and/or modification of existing hardware; adding one recirculation arc, a new experimental area (hall D), and the beamline to it; constructing the major new experimental equipment for this area; and finally, upgrading the experimental equipment in the preexisting halls A–C. This section provides high-level descriptions of the changes made; many details about the accelerator upgrade are found in the numerous references. The principal parameters for 12 GeV CEBAF are given in Table III.

TABLE III. Principal parameters for CEBAF in the 12 GeV era [59].

Energy (hall D)	12 GeV
Energy (halls A, B, and C)	11 GeV
Average current (halls A and C)	1–90 μA
Average current (hall B)	1–100 nA
Average current (hall D)	0.1–5 μA
Bunch charge	<0.5 pC
Repetition rate	249.5 MHz/hall
Beam polarization	90%
Beam size (rms transverse)	~150 μm
Bunch length (rms)	300 fs, 90 μm
Energy spread	2×10^{-4}
Beam power	<1 MW
Beam loss	<1 μA
Number of passes	5.5
Number of accelerating cavities	418
Fundamental mode frequency	1497 MHz
Amplitude control	1×10^{-4}
Phase control	0.1° rms
Cavity operating temperature	2.1 K
Liquifier 2 K cooling power	10 kW
Liquifier operating power	10 MW

A recent aerial view of CEBAF is given in Fig. 12; the camera is held facing in a roughly easterly direction. The service buildings for the two side-by-side linacs are readily visible, as well as the shielding mounds for the original experimental halls A–C in the lower portion of the photograph. The newer hall D is located in the upper center part of the photo. The linacs lie roughly perpendicular to the

FIG. 12. Aerial view of CEBAF with experiment halls labeled in red text.

earth's longitude line at the CEBAF site. Therefore, the linac left located in the photo is known as the North Linac and the right-located linac is called the South Linac. The recirculation arcs for the accelerator lie under the half-circle roads aligned with the linacs. Analogously, the arcs located on the far side of the photo are called East Arcs and arcs located on the near side are called West Arcs. As in the 6 GeV era, all splitting of the beams for delivery to all the halls occurs at the downstream end of the South Linac. The new splitting procedure allowing all four halls to be fed beam simultaneously is described in Sec. III H.

A. New SRF

Reference [47] and the references therein thoroughly document the development of SRF accelerator systems supporting the operation of CEBAF, and changes to the cavities, cryomodules, and supporting superstructure that have been made. In this section, focus is applied to those developments in the accelerating cavities and cryomodules that were needed to prepare for and build the 12 GeV upgrade project. This section is an edited and condensed version of Sec. XVI of Ref. [47], and the figures in this section appeared in that publication and the given references. In particular, much additional information and additional references on cavity processing that are omitted here may be found in Ref. [47].

1. Developing the upgrade (C100) cryomodule

In the earliest thinking about the 12 GeV upgrade, the fundamental cryomodule component was to be new 70 MV cryomodules. Seventeen were to be built: ten deployed in the vacant zones, six to replace the weakest cryomodules in the 6 GeV CEBAF, and one to upgrade the injector so it could achieve the required injection energy. The cavities were to be driven by nominal 5 kW klystrons but operated at higher voltage and a power of 8 kW. Two prototype cryomodules were built and tested during 2001 and 2002 [60,61]. The second prototype was installed in Jefferson Lab's Free Electron Laser and run at 82 MV total energy gain. However, a lack of complete confidence in this approach, plus an overall cost optimization led to a different solution: build 11 new higher performance cryomodules to fill the vacant zones and upgrade the injector. The 11 new modules were designed to provide over 100 MeV energy gain and were therefore, in analogy to the previous naming conventions, dubbed "C100." As they were to fill spaces left vacant in the 6 GeV CEBAF tunnel, the modules were naturally designed to be the same length as in the old linac; the installed warm transitions between the cryomodules could then be identical to those in the rest of the linacs. A goal of 108 MV per cryomodule was adopted, but achieving this performance required a higher power of 13 kW klystrons [62–65]. The highest level requirements for the new cryomodules and SRF cavities for the 12 GeV upgrade project are summarized in Table IV.

TABLE IV. Requirements for the eight cavity cryomodules in the CEBAF 12 GeV upgrade project. Design requirements for the individual SRF cavities in a C100 cryomodule.

Quantity	Value	Units
Cryomodule requirements		
Number of cryomodules	11	
Cryomodule length	10.4	m
Number of SRF cavities	8	
Average cavity gradient	19.3	MV/m
Energy gain	108	MeV
Static heat (@2 K)	30	W
Dynamic heat (@2 K)	250	W
Cavity requirements		
Frequency	1497	MHz
Cells/cavity	7	
Length	0.7	m
Energy gain	13.5	MeV
Average accelerating gradient	19.3	MV/m
Average Q_0	9×10^9	
Q_L	3×10^7	
3 dB bandwidth	50	Hz
Cavity impedance (R/Q)	670	Ω
Geometric factor	281	Ω
Matched current	465	μA
rf power at matched load	6.4	kW
rf power	<10	kW/cavity
Lorentz detuning	2	$\mathrm{Hz}/(\mathrm{MV/m})^2$

A new cavity was designed to achieve high total voltage within the preexisting cryomodule length. Adopting seven-cell cavities to replace CEBAF/Cornell five-cell cavities maximizes the active length within the footprint [66]. The total volume of the helium vessels was significantly reduced by enclosing each seven-cell cavity closely with a vessel. A new tuner was developed [67–69]. The higher order mode (HOM) damping scheme was modified to coaxial out-coupling of the HOM power. Waveguide coupling of the incident power was retained from the 6 GeV era, but the coupler was modified. The modifications greatly reduced cavity sensitivity to fabrication errors and eliminated a field asymmetry in the original design, thus reducing transverse beam kicks [70,71]. Finally, the nominal Q_{ext} for the input coupler was adjusted up from 6.6×10^6 to 3×10^7 to better match the maximum beam load expected during 12 GeV operations.

2. Renascence prototype C100 cryomodule

A cryomodule prototype project called *Renascence* was designed, built, and installed in CEBAF to prepare for the 12 GeV upgrade project. The basic requirements for *Renascence* were to achieve 108 MV acceleration with a dynamic heat load of less than 250 W at 2.1 K, the specifications adopted for the upgrade project [72,73]. A cross-section diagram of a single 7-cell cavity and its

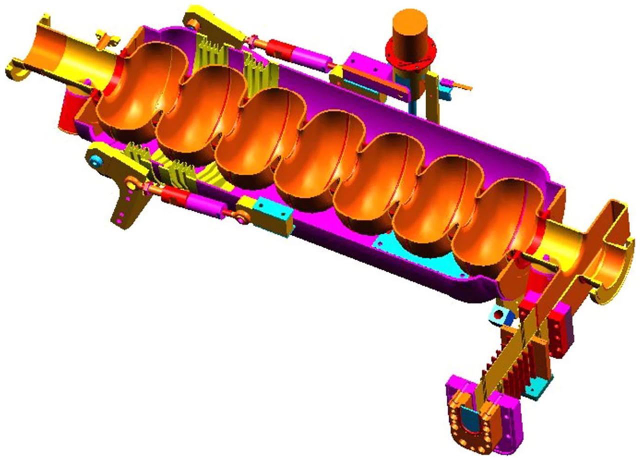

FIG. 13. Cross section of *Renascence* cavity, couplers, helium vessel, and tuner (from [47]).

attachments are shown in Fig. 13. In parallel, two specific cavity shapes were tested in *Renascence*. The "high gradient" (HG) cell shape was optimized to minimize the peak surface electric field. The "low loss" (LL) design was optimized to attain the highest accelerating voltage per cooling power [74]. The cavities achieved a 19.2 MV/m accelerating gradient with less than 29 W heat at 2 K in vertical tests [75]. Cavity performance curves for the 4 LL cavities in *Renascence* are given in Fig. 14.

Several technical improvements deployed in *Renascence* should be noted. A high thermal conductivity rf feedthrough was developed to be used with the DESY-type HOM couplers [77–79], and this achievement has been incorporated into the LCLS-II cryomodules. New beamline flange clamps based on "radial-wedge" geometry were developed and patented [80]. A new clean ultrahigh vacuum seal based on a "serpentine gasket" was developed for attaching the rf input waveguide to the cryomodule [81].

After *Renascence* was installed in CEBAF, multipass beam-breakup instability was observed [82,83]. The beam current was limited to as low as 40 μA due to a 2.156 GHz transverse deflecting mode in cavity 5 (HG002) in this cryomodule. Because the HOM damping in *Renascence* was expected to meet the 12 GeV project specifications, the observation was initially surprising. Subsequent investigation found that, indeed such a HOM in cavity HG002 was not damped to the specified level because of nonstandard conditions as the cavity was fabricated [84]. As a result, additional quality assurance steps were added to the project cavity fabrication procedures, including loaded Q measurements for all relevant HOMs for cavities to be installed in the recirculated linacs. A novel pole-fitting routine was utilized to quickly analyze HOM data [85].

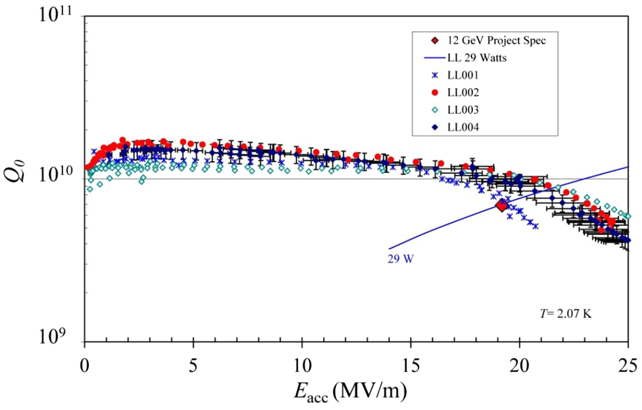

FIG. 14. Qualification tests for the four low loss cavities in *Renascence* (from [76]).

Many other improvements to the C100 were made, both well before and as a result of *Renascence*. For example, there were several significant changes to the cavity assembly procedure [86]. The project was built around the LL cavity structure, but to simplify tuning cavity, stiffening rings were removed. A HOM damping scheme with two couplers located more optimally led to a significant reduction in heat losses at sensitive pickup probes. Stainless steel was substituted for titanium for the helium vessels to save costs and improve reliability [87].

3. Producing the C100 cryomodules and preinstallation performance

The 12 GeV upgrade project formally started in early 2009. Eighty-six C100 cavities were built by Research Instruments (RI) and delivered by March 2011 [88]. High RRR (> 250) fine-grained niobium sheets were provided by Tokyo Denkai and used to fabricate the cavities. These cavities were incorporated into the cryomodules installed in the linacs. In parallel with this activity, and in order to get an early start on the injector upgrade, eight LL cavities were fabricated in-house at Jefferson Lab to include in the injector R100 cryomodule. The R100 cavities were fabricated to higher standards to establish high confidence in the new HOM configuration [22,89]. By April 2011, the R100 cryomodule was finished [90].

The new cryomodules benefited from contemporaneous results obtained from the International Linear Collider (ILC) R&D program [91,92]. In tests using the early cavities, a final surface electropolish was incorporated into the cavity fabrication procedure [76,93]. Figure 15 summarizes the performance of the first twelve 7-cell, in-house-built LL cavities that received a light electropolish as the finishing step, including all of the R100 cavities. The electropolish helped to guarantee excellent cavity performance for all cavities and the project adopted a final 30 μm electropolish followed by 24 h bake at 120 °C just prior to cold testing as a performance risk reduction measure.

Having had plenty of process development time prior to the arrival of the production stream of cavities and the excellent performance of the cavity vendor, the 12 GeV cavity production line ran very smoothly [94–97]. The cavity performance during VTA testing significantly

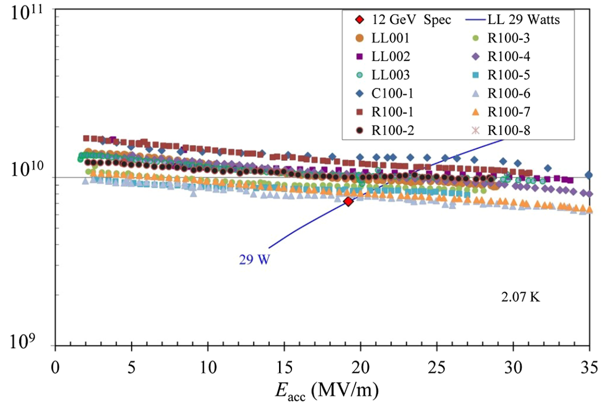

FIG. 15. Performance of 12 CEBAF 7-cell accelerating cavities (from [76]).

exceeded requirements such that most of the cavities were not actually tested to their limits but were only tested to an administratively constrained 27 MV/m. The electropolishing process and cavity performance were so stable and reliable that the decision was made for efficiency to only test the cavities after the helium vessels were welded on. One early production cavity that was tested to its limits was C100-6. Its excellent performance is illustrated in Fig. 16. Subsequently, after the addition of the helium vessel around a cavity, the maximum cooling capacity at the 2.1 K test temperature was ∼70 W.

B. New rf

In order to power and control the cavity fields in each C100 zone, new klystrons are needed for this application and a completely new approach for rf control is necessary. To support the higher gradients and higher Q_L of the 80 newly installed cavities in the 10 linac C100 zones, all have new klystrons, waveguides, rf control systems, and other associated equipment [98,99]. Next, we summarize the performance of the newly installed systems.

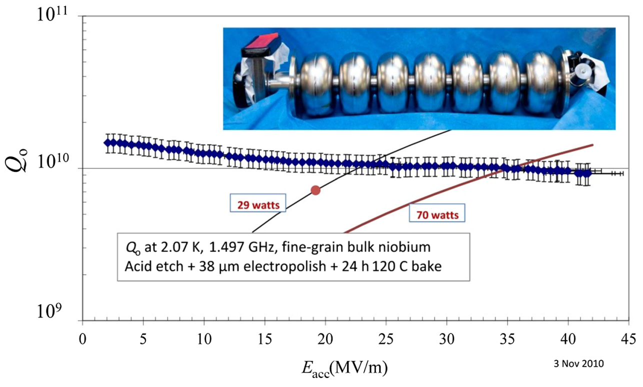

FIG. 16. Performance test of cavity C100-6 without a helium vessel (from [47]).

1. C100 rf system

The C100 cavities are designed to operate cw at a maximum accelerating gradient of 19.3 MV/m. A single klystron powers an individual cavity and its accelerating gradient is controlled by a low-level rf (LLRF) system, as shown schematically in Fig. 17. The upgraded klystrons produce 12 kW of linear power and up to 13 kW saturated. The water-cooled klystron is a five-cavity tube with solenoid focusing, made by L3 Communications. The power requirement includes the power needed to accelerate the beam at the maximum beam load and that needed to compensate for static and microphonic detuning. An rf zone contains four high-voltage power supplies, with each powering two klystrons. The high power amplifier (HPA) system includes additional power supplies necessary for klystron operation as well as multiple interlocks for the protection of these devices. A photo of an installed zone of new klystrons is shown in Fig. 18. Klystrons and the rf control hardware reside in the linac service buildings about 7 m above the linacs.

2. Controls/low-level rf

The rf controls use a traditional heterodyne scheme and digital down conversion at an intermediate frequency. The cavity field and resonance control PID algorithms are contained in one large field-programmable gate array (FPGA). The rf controls are unique in that they incorporate a digital self-excited loop (SEL) that has been implemented at 12 GeV CEBAF with great success [101,102]. Analog SELs had first been used for heavy ion superconducting cavities [103]. Using the SEL allows the cavity to be turned on quickly no matter how far detuned. Interfaces to the controls and interlocks provided by both the HPA and LLRF controls are made via EPICS. The functions that required five cards in the older system now reside in a single chassis, with additional capabilities.

An operational issue, especially relevant for high-gradient low bandwidth superconducting cavities is the radiation pressure detuning (Lorentz detuning) that is

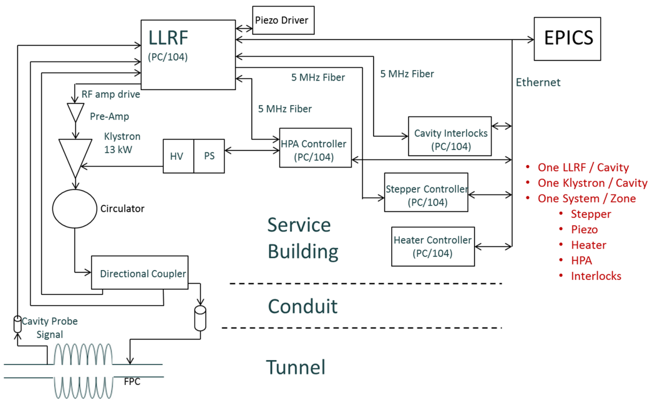

FIG. 17. Schematic diagram of C100 cavity rf system [100].

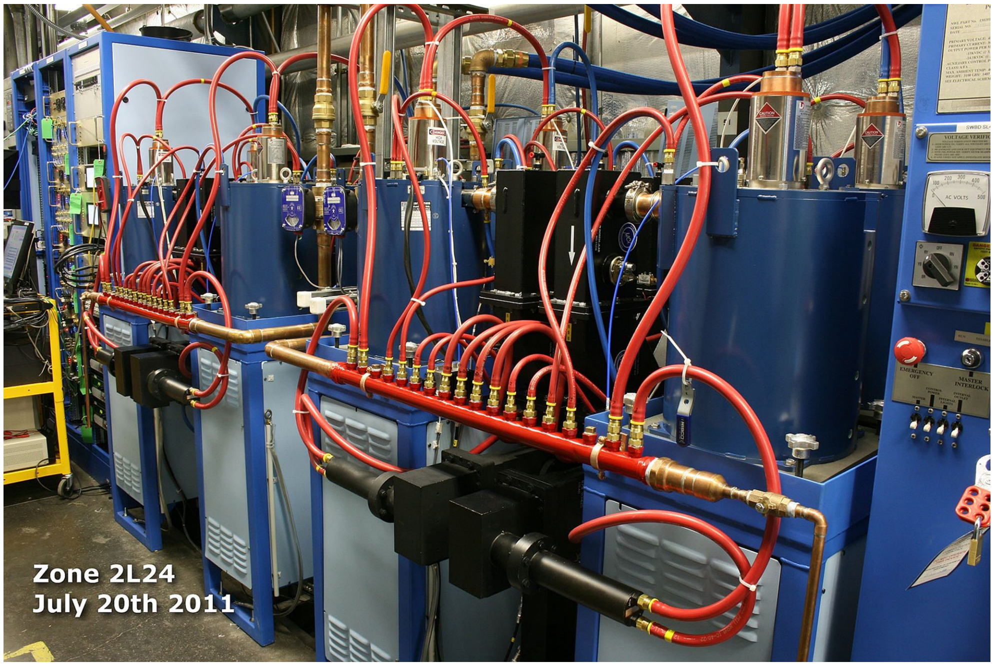

Zone 2L24
July 20th 2011

FIG. 18. Eight 13 kW klystrons installed in the South Linac.

observed at cavity turn-on. The Lorentz detuning is proportional to the square of the cavity gradient and is determined by cavity stiffness. Typically, the detuning is measured during commissioning and a Lorentz coefficient is assigned to the cavity. For the C100 cavities, a Lorentz coefficient of 2 Hz/(MV/m)^2 is typical. For 20 MV/m operating gradient, detuning is 800 Hz from rf off to rf on. The typical method for recovering a Lorentz detuned cavity is to use a piezo actuator and to compensate for the detuning at turn-on. At Jefferson Lab, a different approach is taken. A digital SEL that tracks the cavity up to the operational gradient is employed. Once on frequency and at the requested gradient, a digital firmware application then locks the cavity to the reference. The cavity turn-on sequence utilizes both firmware and EPICS application software.

Cavity faults in the cryomodule present another operational challenge. Mechanical coupling between adjacent cavities is roughly 10%. For example, if a cavity detunes 800 Hz due to the Lorentz effect when faulted, nearby cavities will see 80 Hz of detuning, beyond the nominal 50 Hz bandwidth. The klystron does not have the overhead at higher gradients to compensate for such a detuning. To keep the adjacent cavities at gradient when a cavity trips off, they are immediately switched into SEL excitation. Once the faulted cavity is cleared and brought to gradient, all the cavities are returned to the external lock using an EPICS application.

Cavity microphonics are measured continuously by determining the detuning angle from the cavity signal and the forward power. Both peak and rms tune excursions are displayed for each cavity in EPICS. Figure 19 shows the detuning in Hz for rms and peak for a typical cavity. In addition, the cavity field regulation (phase and amplitude) is also measured continuously. Any excursion is noted on the EPICS rf screen so an operator can investigate.

A useful feature of digital LLRF control systems is the use of data buffers. The hardware allows the operator to catch and postanalyze real-time data from the cavity-control system. This is extremely useful when diagnosing cavity faults or measuring microphonics. Figure 20 is a plot of a cavity fault. The top graph displays the cavity gradient of the faulted cavity and the adjacent cavity. The bottom graph shows each cavity's detuning in Hz. The red curve on the bottom graph shows the sharp reaction (Lorentz contraction from the faulted cavity) of the nonfaulted cavity. The adjacent cavity was operating at a fairly low

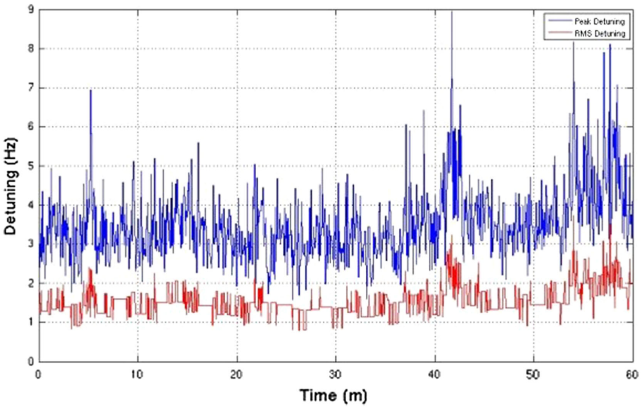

FIG. 19. Peak microphonic detuning (upper) and rms average detuning (lower) of a cavity.

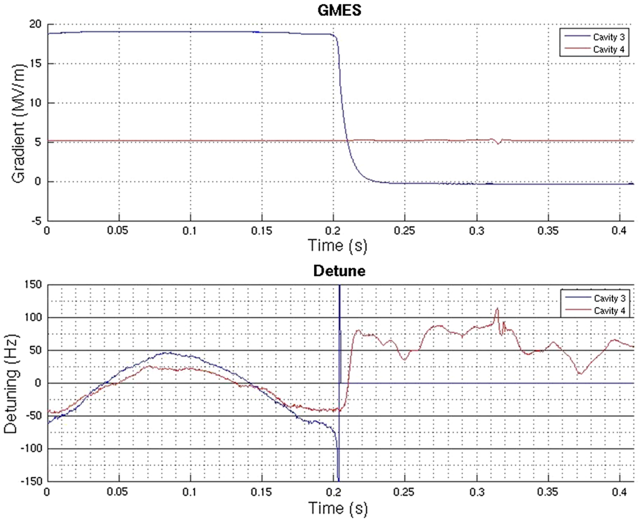

FIG. 20. Graph of gradient and detuning (Hz) as a cavity is faulting (blue). GMES is the measured cavity gradient as the fault progresses.

gradient, 5 MV/m, so the klystron had more than enough overhead to absorb the 77 Hz detuning.

Cavity frequency control is provided by a mechanical stepper motor. The stepper motor can tune the cavity to ±1 Hz of the reference, which meets the requirements for the rf system (control and power). The tuner is automated to keep the cavities close to the master reference. A piezo tuner was included in the design and is available for cavity tuning studies [104]. Activating them has not been needed for CEBAF operations.

The C100 LLRF systems have been in operation for 7 years, and our cavity control methods have been adapted by other newer SRF accelerators including LCLS-II [105,106].

C. Central helium liquefier upgrade CHL II

The original central helium liquefier (CHL), now named CHL I, provides up to 4.8 kW refrigeration at 2.1 K for CEBAF's SRF cavities, 12 kW at 35 K for cryomodule heat intercepts, and an additional 10 g/s liquefaction [107]. A second refrigeration plant of equal capacity is required to meet the refrigeration requirements of the accelerator at 12 GeV [108]. The new refrigerator, CHL II, has nearly identical capacity as CHL I, except for an increased liquefaction rate of 20 g/s. Each plant is capable of supporting one of the two linacs during 12 GeV operations or both linacs simultaneously during 6 GeV operations.

CHL II fully utilizes Jefferson Lab's patented floating pressure—Ganni Cycle process, a constant pressure ratio process wherein the helium pressure in the refrigeration system naturally varies to compensate for changes in the load while the overall thermodynamic efficiency remains constant [109]. The 12 GeV upgrade scope includes a warm helium compression system and a 4.5 K refrigeration system, which comprised two separate cold boxes. A third cold box contains a five-stage cryogenic centrifugal compressor system and 2.1 K subcooler heat exchanger and produces the subatmospheric conditions required to maintain 2.1 K in the Linac. It was originally constructed as a redundant subatmospheric cold box for CHL I [110].

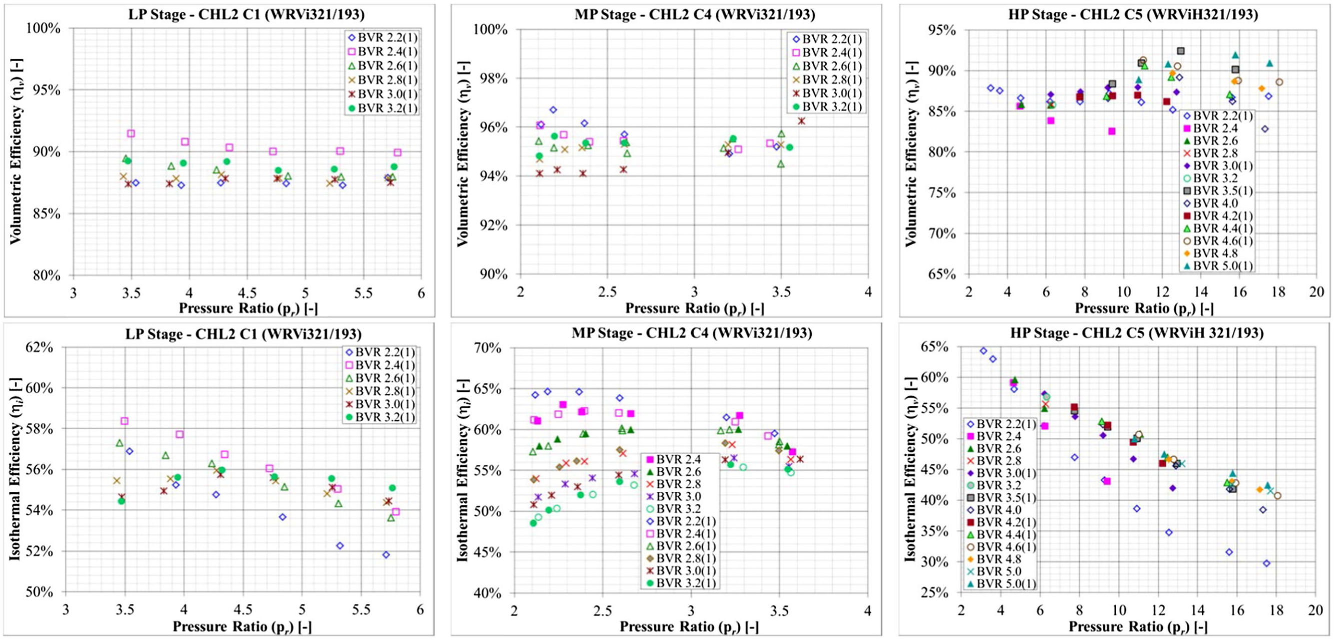

FIG. 21. Measured volumetric (top row) and isothermal (bottom row) efficiency as a function of pressure ratio and built-in volume ratio for the CHL II low (left column), medium (center column), and high (right column) stage compressors, demonstrating good efficiency across a wide operating envelope (from [111]).

The warm helium compression system consists of six oil-flooded screw compressor skids: three 800 horsepower (HP) (597 kW) low-pressure stages, one 800 HP medium pressure stage, one 2500 HP (1864 kW) high-pressure stage, and one 2500 HP swing compressor. The swing compressor can be configured as a low, medium, or high stage and increases system reliability by taking the place of any one of the other machines during routine maintenance or recovery from an unexpected failure. Several key design requirements, particularly a wide operating pressure range and good efficiency, are addressed by the novel design of the oil management systems on the compressor skid [111]. Figure 21 illustrates the operational efficiency (isothermal and volumetric) of the CHL II compressors across a wide range of operating pressures necessary to fully utilize the floating pressure process.

The first of the two cold boxes, the upper cold box, spans 300 to 60 K and incorporates several brazed aluminum plate-fin heat exchangers, a liquid nitrogen precooler, and two 80 K purifiers. The other, lower, cold box spans 60 K to 4.5 K and also incorporates several heat exchangers as well as four turboexpander stages, a 20 K purifier, and a 4.5 K subcooler heat exchanger. Efficiency is optimized by designing each expansion stage with an equal temperature ratio, or Carnot step [112], and compatibility with the floating pressure process is inherent to the design [113]. The CHL II system can be turned down to match load conditions significantly below its maximum capacity, and as shown in Fig. 22, exhibits remarkably little loss of efficiency in the process. This turndown is achieved by varying the helium supply pressure from the warm compressors to the cold box between 19.5 and 6.5 bar, without throttling the turbines and with little to no operator intervention [113]. Due to the successful and efficient operation of CHL II, the design has been adopted for the MSU FRIB [114–116] and SLAC LCLS-II [117] helium refrigeration systems.

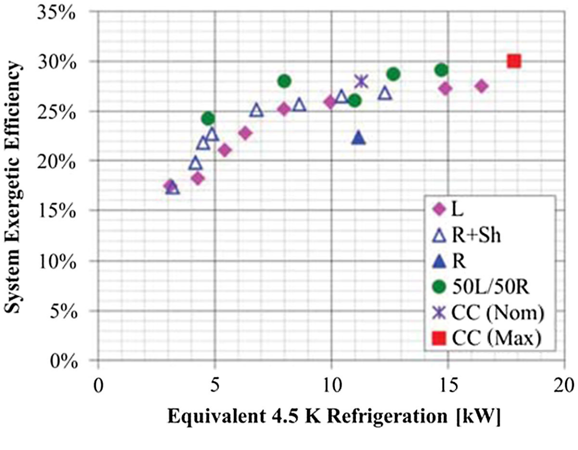

FIG. 22. CHL II cold box performance testing results demonstrate a wide turndown range with remarkably little effect on the overall system efficiency. Test conditions are L (4.5 K liquefaction load), R (4.5 K refrigeration load), and 50L/50R (equal mixed load). Data points for cold compressor (CC) at nominal and maximum load (from [113]).

D. Magnets

The initial CEBAF magnet designs were based on a 4 GeV electron energy requirement, with an additional goal that the 2200 magnets in the accelerator eventually achieve 6 GeV [118]. The magnet complement was measured to support operating the accelerator at 6 GeV beam energy. In order to operate at 12 GeV, most of the dipoles and quadrupoles in the machine needed to operate beyond their existing field maps. In particular, to double the magnetic field required at 12 GeV, most of the dipoles would become saturated. Consequently, the bulk material in many magnets needed to be modified to avoid saturation and all of the magnets were remeasured to magnetic fields up to the 12 GeV specification. This section will describe the modifications and characterization required to support a model-driven 12 GeV accelerator.

1. Dipoles

Prior to the upgrade project, a 2 m arc dipole magnet was both modeled and measured to understand the saturation effects resulting from the higher current needed for 12 GeV. The PC-OPERA 2D finite element package was used for modeling. A plot of the percent saturation is shown in Fig. 23 for the measured and PC-OPERA calculations for an unmodified dipole and for a dipole with an additional steel return leg. Due to the good agreement, modeling was then performed to determine the minimal additional steel needed to reduce saturation effects to acceptable levels. Such considerations resulted in an "H-Steel" design solution where three additional plates were added to the existing dipoles to provide sufficient return paths for the magnetic flux generated at 12 GeV operating currents as seen in Fig. 24. The H-Steel plates were fabricated and added to the test dipole so that magnetic measurements could verify performance. Figure 23 shows the results of

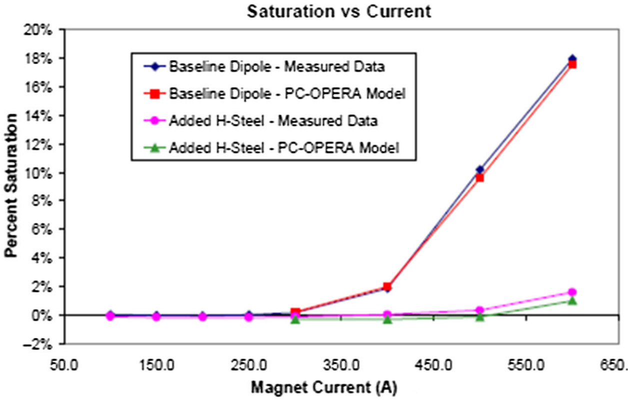

FIG. 23. Saturation plot for converted dipole (from [118]).

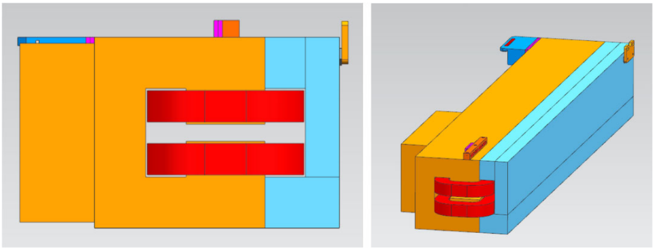

FIG. 24. 6 GeV arc dipole flux return and pole (orange), coil (red), and H-Steel addition enabling 12 GeV capability (sky blue).

the measurements [118]. Additional testing was completed to verify the field quality and thermal integrity of the magnets at 12 GeV currents. Based on the results of the modeling and tests, the H-Steel design modification was adopted for the 12 GeV upgrade.

2. 12 GeV magnetic measurement

Field integrals and field quality are measured using a combination of stretched wire and hall probe grids. Stretched wire measurements provided a simple, fast, and accurate measurement method to use for the dipole mapping. Because all the arc dipoles had been mapped at 6 GeV, there was no cause for concern with respect to voids in the steel. All dipoles are mapped using a single stretched wire method. Additionally, 10% of the dipoles are mapped using a hall probe grid to ensure measurement integrity and provide detailed mapping information.

An analysis routine is developed to evaluate the field quality and integrated strength for 12 GeV dipole magnets mapped with the hall probes. The analysis calculates results based on the curved trajectories the beam follows as it moves through the bending dipoles. Data points are analyzed by a program developed at Jefferson Lab. Field integrals are computed by interpolating between measured data points to create points on the beam trajectory. These field values are then integrated along the curved beam trajectory to calculate the field integrals. Field quality is evaluated by comparing the ratio $B'L/BL$ to the specification where $B'L = \int(\partial B/\partial r)dz$ [119].

Measurements identified some integrated strength inconsistencies among arc magnets. Strength matching of arc dipoles is required because each arc is powered from a single power supply and dipoles do not use individual shunts. To solve this issue, field lengthening shims are added to some dipoles to meet the matching specification. After correction, gradient measurement results show acceptable field profiles for all arc magnets and most spreader, recombiner, and extraction magnets. When needed, field shaping shims are added to correct gradient errors on nonarc dipoles by using a parabolic shim shape to add length to the off-center field integrals along the horizontal axis as shown in Fig. 25.

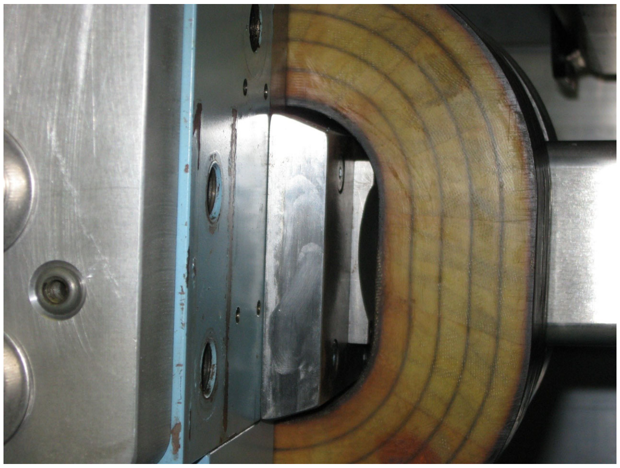

FIG. 25. Photograph of magnet shim correcting field flatness installed in a 12 GeV CEBAF dipole.

Measurement values have been compared against model values. Because the detailed breakdown of the multipole components is not available, a method was developed to compare TOSCA predictions with the measurements from the magnet test stand [120]. Agreement is good when taking into account that TOSCA models do not incorporate misalignment or construction errors.

3. Quadrupoles

The 6 GeV CEBAF experience is used to develop specifications for and to model the 12 GeV quadrupoles. It is found that many existing quadrupoles could be powered to higher currents to meet the design requirements. About 20 A power supplies are used in place of preexisting 10 A supplies in several locations to increase the focusing strength of those magnets. A second quadrupole and 20 A power supply is also added at a few locations [121]. Two new quadrupoles are required for the upgrade. Their designs were based on existing CEBAF "QA" quadrupole designs and required both magnets to fit within the same space along the beam line and to mount onto existing girders. This requirement eliminates the need to modify or design new girder parts and assemblies [122]. The pole tip designs on these magnets are scaled from the QA quadrupole design. Pole root saturation and harmonic effects are studied and optimized using Vector Fields OPERA-2D simulation software. Each new quadrupole is measured in the Magnet Measurement Facility. Rotating coil measurements are used to define magnet strength, multipoles, and quadrupole centers.

Measurement results showed well-matched quadrupole performance. Measurements are done on a rotating probe measurement stand using a MetroLab PDI measurement system along with a printed circuit board rotating coil. Magnet strength measurements showed all magnets within each new family are equal within ±0.5% as seen in Fig. 26. Harmonic content is measured and evaluated in two ways.

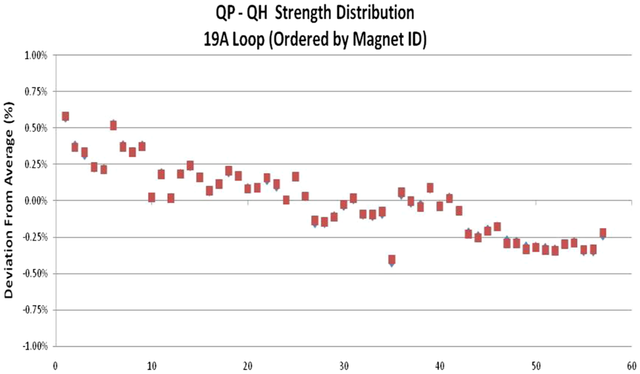

FIG. 26. Measured relative magnetic strength deviation from average for QP and QH quadrupoles.

First, individual multipoles are verified to ensure no significant fabrication errors exist. To compare with the defined 12 GeV specifications, the sum of error multipoles relative to the radial position is calculated. An example showing multipole measurements is shown in Fig. 27. All new quadrupoles are measured and shown to meet 12 GeV specifications. Figure 28 shows a comparison between the measured quadrupole gradient error and specifications needed from beam dynamics calculations. Operating CEBAF at 12 GeV with beam optics settings largely downloaded from an energy-scaled design has proved the acceptable performance for the existing quadrupoles even when driven at higher currents and for the new quadrupoles. Table V summarizes the total counts of magnets adjusted and/or measured during the 12 GeV project.

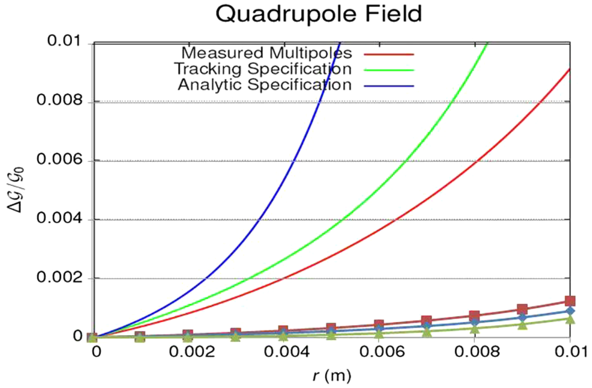

FIG. 28. Comparison between beam dynamics requirements (solid curves) and measured performance for a selected quadrupole including several multipoles.

4. Path length chicane dipole upgrades

The 6 GeV machine circumference ("path length") was adjusted via three-dipole chicanes in the "extraction" regions upstream from each recirculation arc. The physical layout of each supported a 1 cm span of incremental path (design value of ±mm), constrained by the installed dipole and power supply capacity. Regular measurement throughout the operating experience at 6 GeV provided values for expected seasonal variation in path length and in variable pass-to-pass path length [123,124].

For three-dipole chicanes, path correction is an inverse quadratic function of beam momentum for the constant magnetic field. Nominally, doubling CEBAF energy would reduce the available path compensation by a factor of 4 for magnet-limited systems. The observed variable circuit-to-circuit path compensation through years of operation exceeded the anticipated power supply limits. In order to preserve operational efficiency, an upgrade of the chicanes is needed. As summarized in Table VI, the drive current capacity in each of the chicane dipoles is increased by a factor of 2, and the length of the dipole magnets in the fourth chicane (after the second beam pass of the South Linac) is increased by 60%. Even though the net path change capacity is therefore decreased by a factor of 2 (a factor of 40% for the fourth chicane), using the modified system plus fine adjustment of the fundamental operating frequency (at the level of 10 s of kHz) provides sufficient control of the path length in the 12 GeV era. Interestingly, operating scenarios have been found without the need for a tenth chicane in the new recirculation arc beamline leading to the sixth pass through the North Linac.

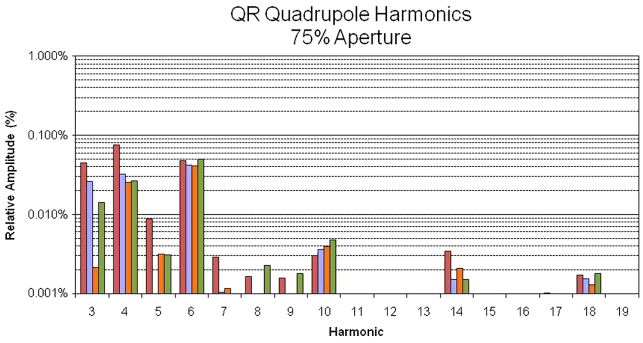

FIG. 27. Rotating coil field harmonics measurement for four QR style quadrupoles at 12 GeV field setting.

TABLE V. Magnets modified and/or remeasured for 12 GeV beam operations.

Type	Location	Number
Dipole	Arcs 1–10	288
Dipole	East spreader	22
Dipole	East recombiner	17
Dipole	West spreader	17
Dipole	West recombiner	17
Dipole	Transport recombiner	17
Dipole	Hall transport	26
Quadrupole	Throughout	114
Corrector	Throughout	120

TABLE VI. Changes to the path length dipoles (“doglegs”) for Operating with 12 GeV beam energy.

Chicane	Current capacity (A)	Dipole change
1	270	
2	270 to 450	Coil area increased 60% length increase
3	270 to 450	
4	270 to 450	
5	270 to 450	
6	270 to 450	
7	270 to 450	
8	270 to 450	
9	270 to 450	

E. Hall D/Arc 10

The original CEBAF magnet transport included nine recirculation arcs (arcs 1 through 9) to support ten linac acceleration passes. Odd-numbered arcs are the “east” arcs on the right side of Fig. 11, while even-numbered arcs are the “west” arcs on the left side of Fig. 11. To support the addition of hall D and an additional linac pass, a new arc (arc 10) is installed below the existing (upgraded) west arcs as part of the 12 GeV upgrade. Corresponding modifications are made to the spreader and recombiner regions at each end of the west arcs, including additional septa, to incorporate arc 10. These modifications are needed to allow rf beam separation between five-pass beams to halls A–C and beam into arc 10 and to include the recombiner merge of the new arc 10 beam into the North Linac. As in the remainder of CEBAF, all quadrupoles and corrector magnets are independently powered in arc 10.

Arc 10 is composed of four superperiods. Analogously to the lower arcs, the optics provides second-order achromaticity and linear isochronicity. Arc 10 M_{56} is tunable via quadrupoles throughout the arc optics, though M_{56} is less critical in arc 10 than in the low-energy arcs. The 32 main arc 10 dipoles are all on the same main bus and have the same 4 m length. Dipole trim windings are added to all arc 10 dipoles to correct for synchrotron radiation beam energy losses; these windings have been tested during commissioning but found to be unnecessary to maintain beam transport quality. Arc 10 has no separate path length chicane (see Sec. III D 4), as sufficient path length modifications can be implemented in the arc proper.

The North Linac FODO optics are designed to provide 120° phase advance per cell for the lowest-energy (first pass) beam. The higher energy hall D beam is thus underfocused and nearly ballistic, leading to tight tolerances on beam optics (particularly divergence) at the exit of the arc 10 recombiner. Design beta functions are over 200 m at the end of this pass of the North Linac, entering the east spreader for separation to the hall D transport line.

The east spreader is modified to add new septum magnets for extraction to hall D and to adjust separation geometry to accommodate space for these magnets. Corresponding changes are made to the east recombiner to preserve spreader and recombiner symmetry. A triplet, quadruplet, and triplet are used to transport and focus beam to a small tuning beam dump ~125 m downstream of separation before entering a vertical ramp toward the hall D tagger enclosure. Vertical dispersion from the vertical separation is not corrected until the vertical ramp, which adds sensitivity of optics corrections to energy fluctuations.

The vertical ramp section starts and ends with antisymmetric vertical dipoles (bending a total of 7.8°) to create a +5.2 m vertical dogleg, with seven quadrupoles between the dipoles arranged in a triplet/singlet/triplet configuration. The central quadrupole is located near vertical dispersion zero crossing and at a vertical beta waist to provide an independent degree of freedom for horizontal beam size and convergence. This is followed by four quadrupoles after the last dipole to provide the other degrees of freedom necessary for control of beam size and convergence in both planes onto the hall D radiator. The optics of the latter half of the hall D beam transport is shown in Fig. 29.

The initial hall D experimental program is dominated by the GlueX collaboration and detector [125,126], which uses a polarized photon beam generated by coherent Bremsstrahlung from the passage of 12 GeV electrons through a diamond radiator. The photon beam convergence and polarization are strongly correlated with the electron beam convergence at the radiator. A collimator 75 m downstream of the radiator is used to select out 40% polarized photons for use in GlueX experiments. After interaction with the radiator, the electron beam is bent through a large tagger dipole, where a tagger hodoscope correlates low-energy electron events with corresponding photon events in the detector for accurate energy reconstruction. The primary electron beam continues through the tagger dipole and is delivered to the hall D beam dump. The hall D transport optics are designed, iterated, and documented in a set of Jefferson Lab Technical Notes [127–129].

Two substantial changes are made in the hall C beamline supporting 12 GeV operation. First, the bending capacity of

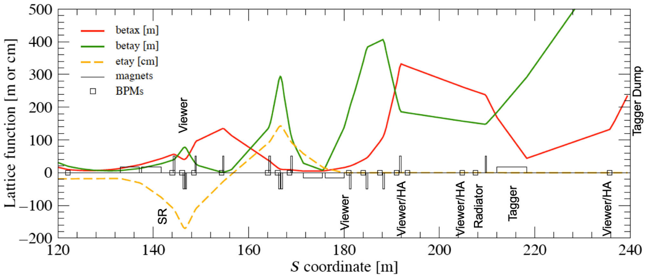

FIG. 29. Hall D transport line optics through the vertical ramp to the tagger dump. Locations of synchrotron radiation monitors (SR), viewers, and profile harps (HA) are indicated. Taller vertical rectangles are horizontally focusing (positive) or vertically focusing (negative) quadrupoles.

the dipoles taking the beam to hall C is increased as discussed in Sec. III D 1. Second, to be able to bend the beam as required in the Compton polarimeter [130], the difference in height between a straight path and the bent path is reduced and a pair of 1 m dipoles is added after the Møller polarimeter to strengthen vertical bending. The beamline from the shield wall to the diagnostic girder was at a small angle in the 6 GeV era. This offset is eliminated moving all the steering correction to the hall. None of the quadrupoles in the hall C beamline are replaced in the transition to 12 GeV. Likewise, the dipoles taking the beam to hall A are upgraded for the enhanced energy to be delivered, but no further changes are needed to the quadrupoles in this beamline.

F. Accelerator physics

At the onset of the project, it has been determined that the main beam physics drivers for the design are the impact of the synchrotron radiation on emittance growth, halo formation, and radiation heating. Other issues such as the heating in the accelerator tunnel due to the magnets being operated at higher currents are also quantified. The first issue may be addressed by a judicious choice of optics combined with a more stringent set of requirements on the magnet field quality. Field specifications are derived from these considerations and utilized in the design of the modified dipoles and the new ones in arc 10.

1. Aperture requirements

In order to keep the beam synchronized with the rf acceleration in the linacs, a combination of dogleg chicanes, changing the rf frequency of the cavities, and offsetting the orbits in the arcs is employed. The later is necessary because there is no dogleg path length adjustment chicane beyond ARC9. Instead, the path length is adjusted by shifting the orbit in the arc. This led to developing a specification for the aperture requirements including beam size, steering allowance, and for arc 10, path length orbit shift.

2. Halo specifications

Various factors can contribute to the formation of beam halo in particle accelerators. Chief among them is the amount of synchrotron radiation, which increases significantly in the 12 GeV machine compared to the 6 GeV machine. This effect causes emittance growth, which in turn leads to larger beam sizes that can sample nonlinear magnetic fields more in the 12 GeV machine.

Other factors that can contribute to halo formation include the rms of the beam orbit centroid relative to the magnet center, mismatched beam optics, and scattering off residual beam gas.

Nonlinear particle tracking simulations are needed to study halo formation. The amount of beam halo due to residual beam gas scattering is expected to be roughly $1/4$ of the beam halo in the 6 GeV machine. The 12 GeV design requires careful attention to these factors to contain emittance growth and minimize halo formation.

With the exception of the synchrotron radiation, all these other effects were present in the 6 GeV machine and we can use our past experience and measurements as a benchmark. In particular, the experiments in hall B that typically require an electron beam in the range of 1–100 nA are very sensitive to halo due to the high luminosity 4π detector. Measurements are routinely performed using wire scanners equipped with photomultipliers for picking up the secondary electron emission generated by the wire going through the beam. This measurement provides a dynamic range of over 6 orders of magnitude.

The experimental hall D, which will see an electron beam of 12 GeV and feature a full acceptance detector similar to that in hall B, sets the maximum allowable halo to be at least 6 orders of magnitude less than the core of the beam assumed to be Gaussian.

In order to include the effect of synchrotron radiation and nonlinear mismatches, a set of simulations is performed where we generate three representative orbits that simulate a real machine. We introduce random misalignments and mispowering to the magnets and multipole components. Finally, we apply a global steering of the beamline using the same algorithms one would use in the real machine. This procedure creates three orbits with standard deviations of 0.3, 0.6, and 1 mm, respectively, each consisting of over 100 million particles. The magnitude of the halo is quantified using the aforementioned measure.

From these studies, we conclude that if the orbit rms is less than 1 mm, we expect a halo to be at least 6 orders of magnitude less than the signal.

The halo due to Mott scattering on the residual gas in the beampipes is evaluated separately and found to be negligible for the existing vacuum, thanks to the fact it is inversely proportional to the square of the beam energy.

3. Optical matching and implications on emittance growth

The matching specifications for the CEBAF lattice were derived from the requirements that the invariant ellipse distortion resulting from linear errors be exactly compensated by quadrupoles located in the spreader regions.

The amount of emittance dilution arising from a mismatched beam propagating through a lattice with higher order multipoles and in the presence of synchrotron radiation is estimated separately and used to draw specifications on the allowed magnitude of these multipoles and the amount of mismatch. That mismatch is quantified by the ratio of the area between the design ellipse and the mismatched new ellipse obtained after rematching the optics [131].

The process by which one performs these arc-by-arc corrections is described in Sec. IV C 2.

4. Control of betatron envelope in higher linac passes

The upgrade of CEBAF from 6 to 12 GeV led to doubling the acceleration in the linacs, adding an extra recirculation arc and modifying the spreaders and recombiners to accommodate these changes. The spreaders and recombiners are two-step achromatic vertical bend systems. The nature of this design is such that the peak beta functions in the spreaders are high. The problem is magnified at higher passes where the linac focusing is essentially nonexistent.

A mismatch error in the upper passes will result in a loss of control of the beam envelope as well as a significant emittance growth. Unlike the 6 GeV CEBAF for which the linac and spreader/recombiner optics were optimized for the first pass, a global approach was chosen in order to minimize the peak betas in the higher passes by trading it with a slightly worse betatron profile at lower passes where it is not significantly impacting beam envelope and emittance growth. All five passes are optimized together to find the best envelope profile [132]. The gradient distribution in the linacs is also investigated.

Emittance growth is impacted by several things, namely the nonlinearities in the magnets due to their multipole contents which drove the steering specifications as well as the linac accelerating profile.

The design was iterated several times until we found a satisfactory combination of gradient distribution as well as multipole and steering specifications. This led to installing the new C100 modules at the end of the linacs for practical and budgetary reasons even though the smallest emittance growth is achieved by having these five cryomodules at the start of the linac.

5. Synchrotron radiation heating

Estimates of the synchrotron radiation power deposition are shown in Table VII. The peak deposition occurs in arc 9 and results in a line load of about 0.2 W/cm. Outgassing is estimated to be well within the existing pumping capacity.

TABLE VII. Synchrotron radiation heating.

Beamline	Dipole length (m)	Beam energy (GeV)	Beam current (μA)	Radiation power (W)
Arc 6	2	6.7	90	509
Arc 7	3	7.8	90	587
Arc 8	3	8.8	90	1029
Arc 9	3	9.9	90	1502
Arc 10	4	11.0	5	109
Hall D	4	12.1	5	9

G. 12 GeV CEBAF optics design

Originally, most of the longitudinal bunching in the injector occurred prior to the acceleration up to the final injection energy. The injector experienced difficulties transporting the beam, because of small tails in the longitudinal beam profile. Particles in these tails were not on the crest of the accelerating wave and were ultimately lost preventing machine operation at high beam current. To alleviate this problem, the optics in the injection chicane has been redesigned to create additional bunch compression at 123 MeV. A significant advantage of high-energy bunching is that the bunching is not affected by the beam space charge. To facilitate this change, a new non-isochronous optics with a negative M_{56} of about -24 cm is designed and loaded in the injection chicane magnets. To perform the bunch compression, one needs to shift the rf phase of the main injector linac by about 8°. To avoid problems with focusing changes at the beginning of the linac, only the second of the two injector cryomodules is shifted in phase. The new configuration significantly improves machine reliability for high current operation.

For 12 GeV CEBAF, the synchrotron radiation effects on beam motion become rather significant in the higher arcs with energies above 6 GeV. Emissions of individual photons excite spurious betatron oscillations; the resulting energy “drop” perturbs the electron trajectory causing its amplitudes to grow leading to cumulative emittance increase. Details of the single particle dynamics are given by Sands [133].

In order to limit emittance dilution due to the synchrotron radiation, several options have been explored. Alternative beam optics are proposed for the higher arcs to limit emittance dilution due to quantum excitations [134]. The optics can be implemented within the 6 GeV physical layout of the arcs (baseline design); producing the new optics only involved changes in quadrupole magnet settings. The effect of synchrotron radiation has been suppressed through careful lattice redesign, by appropriately organizing the Twiss functions and their derivatives inside the bending magnets. A double bend achromat (DBA) cell variety using a triplet rather than a singlet to suppress dispersion is chosen as a “building block” for the arc optics. The lattice provides significantly suppressed emittance dilution while offering superior lattice tunability and compactness. The lattices for Arcs 6–10 are reworked based on the above DBA structure. The resulting emittance growth is suppressed by a factor of 0.64 compared to the “Standard” arc 6–10 optics [135]. Figure 30 shows that measured CEBAF beam emittances during commissioning were well below specifications and closely match design expectations [136,137].

Responding to the need for diagnosing the beam energy spread, the optics of arcs 1 and 2 have been redesigned and synchrotron light monitors are installed to resolve the beam energy spread with high resolution. The optics goal is to increase the horizontal dispersion by a factor of 3 and to decrease the horizontal beta function in the middle of both arcs at the location where the new monitors are installed. The new arc optics, with a mirror-symmetric horizontal

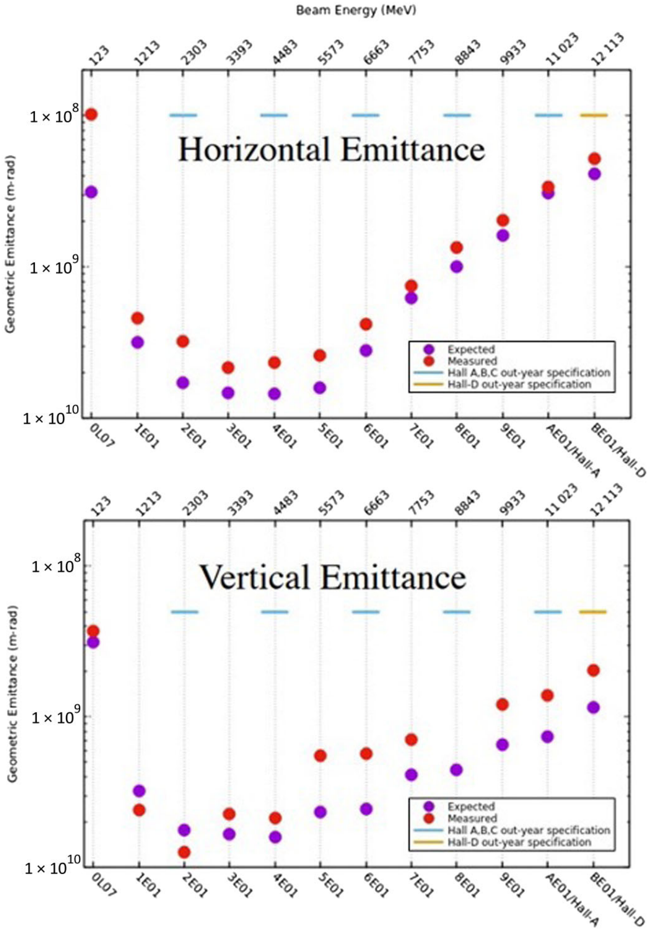

FIG. 30. CEBAF 12 GeV horizontal and vertical emittances measured at the injector, each arc, and at the entrance to hall D during 12 GeV commissioning (from [137]).

dispersion pattern, is designed so that it greatly enhances the resolution of the beam energy spread measurement without limiting the energy aperture of the beamline. To preserve tunability of the new optics, one needs to allow for independent correction of both the horizontal dispersion and M_{56}. This is accomplished by appropriate tailoring of the horizontal betatron phase advance inside the arc to provide two pairs of orthogonal "knobs" (quadrupoles): for dispersion and momentum compaction adjustments. Furthermore, a betatron wave excited by the first tuning quad, which propagates with twice the betatron frequency, is canceled by the second wave launched by the remaining quad in the pair, so the net betatron wave is confined to the tuning region, and subsequently, the tuning process does not affect the betatron match outside the arc.

H. Extraction system/4 hall operations

The extraction system is designed to selectively transport 249.5 and 499 MHz interleaved bunch trains provided by the polarized source to the proper pass and experimental hall needed for the physics program. Figure 31 shows an elevation view of the final configuration for the 12 GeV extraction upgrade. The approximately 170 m long segment represented here starts at the entrance of the southwest spreader and ends at the exit of the Lambertson magnet at the entrance to the beam switch yard. The key elements of the system are 499 and 749.5 MHz rf separators, focusing and defocusing quadrupoles, thin and thick septa magnets, extraction chicane dipoles, beam position monitors, beam viewers, and the Lambertson magnet. In the following sections, a detailed description of these elements and their role in the extraction system is described.

The original 6 GeV CEBAF configuration used ten 499 MHz rf separators with one in the first and second passes, two in the third pass, three in the fourth pass, and a set of three cavities oriented for vertical deflection located approximately 3 m past the exit of the single YA stack. For the first four passes, the cavities were phased to provide peak deflection to the left for the beam intended to be extracted to halls A, B, or C. This puts the other beam(s) on half power points, 120° from peak phase, to be deflected to the right and sent into CEBAF for recirculation to higher passes. The long drift from the rf separators to the entrance of the YA stack along with the horizontally defocusing quadrupole between them provided 16.5 mm of separation as measured by precision wires mounted on the beam viewers and the adjacent beam position monitor located in front of the thin septa. Horizontal correctors at the entrance of the rf separators were used to place the recirculated beam(s) at +5 mm and the extracted beam at −11.0 mm.

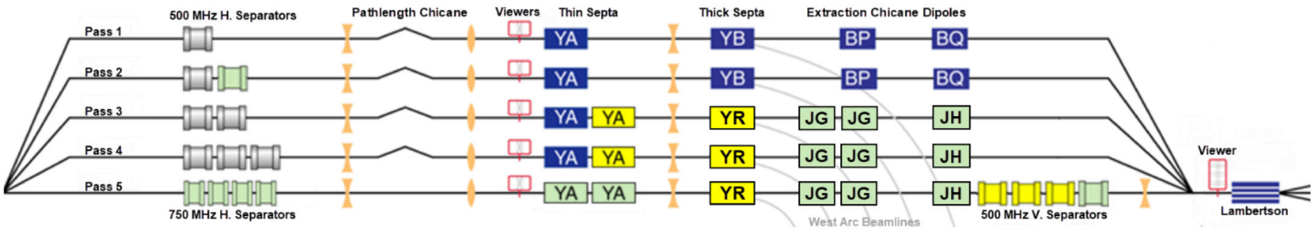

FIG. 31. An elevation view of the overall 12 GeV CEBAF extraction system. Gray cavities and blue magnets are in their original locations. Yellow elements were relocated from other 6 GeV CEBAF locations. Green elements were newly constructed for the 12 GeV accelerator.

The 1-m long YA magnet had a 5 mm wide septum that is protected by a water-cooled molybdenum nose piece. The magnets were aligned so that the right edge of the septum is at the nominal zero coordinate in the x plane. Beams to the right of the septa enter a field free region while beams to the left see the full field of the magnet and are kicked to the left. The recirculated and extracted beams continued to drift apart as they were transported to the entrance of the 1-m long YB stack. The defocusing quadrupole combined with the long drift provided 4.5 cm of separation at the entrance of the YB. The recirculated beam(s) continued to drift through the field-free region and arrived at the West Arc point of tangency at the center of the first arc quadrupole for another pass around CEBAF. The 1-m YB, 2-m BP, and 1-m BQ magnets comprised an extraction dipole chicane that is used to physically avoid the first stack of west arc quadrupoles next to the BP magnet and to place the extracted beam on zero position and angle at the center of the first quadrupole of the transport recombiner beamline segment. The 2.3-m long Lambertson magnet had an upper and lower set of magnet coils that were independently powered to have a field oriented in the negative y axis for the upper coil and in the positive y axis for the lower coil. The magnet had three separate vacuum chambers with hall A in the upper chamber kicked to the right, hall B in the field-free region between the coils and hall C in the lower chamber kicked to the left. The hall A and C beamlines were 2.2 cm above and below the hall B beamline, respectively. Vertical correctors in front of the Lambertson magnet were used to position the beam at the proper elevation for the relevant hall.

The fifth pass of the 6 GeV extraction system used three rf separator cavities oriented for vertical deflection. These cavities were phased to put the hall B beam on zero crossing while kicking the 120° phase delayed hall A beam up and the hall C beam down. A pair of YA septa magnets amplified the kick for the hall A and C beams leaving the hall B beam undeflected. Empirical settings were adjusted to place the beam(s) at the proper elevation(s) at the entrance to the Lambertson magnet.

1. 6 GeV to 12 GeV layout changes

The overall operational paradigm of the 12 GeV extraction upgrade is largely unchanged from that presented above. The following changes are needed to manage the higher energy beams and to accommodate the fourth experimental hall D.

rf separators

1. The operating power of existing 499 MHz separators is increased.
2. An additional 499 MHz separator is added to the second beam pass.
3. Four horizontal 749.5 MHz separators are installed in the fifth pass beamline beneath the existing 499 MHz cavities.
4. The output coupler for one of the four existing 499 MHz rf power amplifiers is modified to operate at 749.5 MHz.
5. The vertical rf separators are relocated to the transport section beyond the west arc and an additional cavity is added.
6. New 10 kW solid-state amplifiers are installed to power the relocated vertical rf separators.

Magnets

1. The two-fifth pass vertical YA magnets are relocated to the third and fourth passes.
2. Two new YA magnets for the fifth pass are fabricated.
3. The third and fourth pass 1-m YB septa are replaced with existing 2-m YR magnets and a third existing YR has been relocated to the fifth pass.
4. The third and fourth pass 2-m BP dipole magnets are replaced with pairs of a new 2-m JG magnet and another JG pair is added to the fifth pass beamline.
5. The third and fourth pass 1-m BQ dipole magnets are replaced with a new 2-m JH magnet design and another JH magnet has been added to the fifth pass beamline.
6. The vertical correctors, used in the first through fourth pass for setting the elevation of the beams at the entrance of the Lambertson, are replaced with higher field magnets.

2. rf separators

The rf separator cavities for CEBAF were conceived of and designed in the early 1990s [10] with the first proof-of-principle experiment conducted in the CEBAF injector using a 45 MeV beam in 1992 [138]. Each separator cavity is a two-cell warm copper structure with each cell containing four coplanar copper rods to concentrate the TEM dipole mode along the central axis of the cavity. A pair of copper rods can be seen in the interior view of Fig. 32 along with a mechanically actuated tuning plate, coupling holes for the adjacent cell, and the 15 mm beam aperture between the rods. The unattached 14″ end flange holds the other pair of copper rods. Water channels in the end flanges and center flanges deliver coolant to the rods that are fitted with internal septum plates. The interior of the cavity bodies is copper plated and water cooled.

Power is delivered through a critically coupled inductive copper loop mounted on a 1–5/8″ coaxial adapter and the field is measured through an under-coupled loop probe. A fully assembled 499 MHz cavity is shown in Fig. 32. To allow for simultaneous beam delivery in all four CEBAF experimental halls, a concept using 249.5 MHz electron bunches and 749.5 MHz rf separators was proposed in 2012 [24,139]. Electromagnetic and thermal analysis studies for the shorter structure began in 2014 and a prototype cavity was fabricated for bench testing. The CST electromagnetic design simulations center on an optimization of the high-power input coupler position, loop size and rotation, and the tuner paddle position to optimize frequency and field flatness [140]. Four production cavities

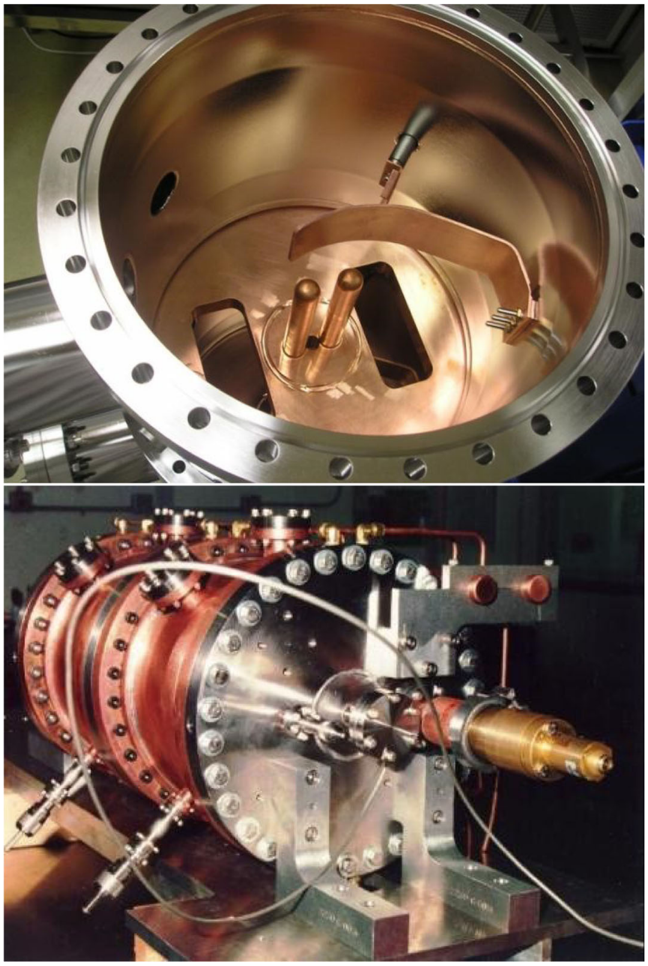

FIG. 32. Interior and fully assembled views of a 499 MHz rf separator cavity.

have been produced, installed in CEBAF, and then commissioned with beam in 2018 [141].

The nominal reference values and calculated power requirements are shown in Tables VIII and IX. For both the 499 and 749.5 MHz cavity designs, the modeled shunt impedances have been experimentally verified through beam-based measurements of the horizontal beam position at the entrance to the downstream YA septa as a function of cavity power with the beam phase at $\pi/2$ relative to zero-crossing phase.

The peak power per cavity from Table IX is just under 3 kW. To verify thermal modeling and that cavity frequency shifts as a function of temperature are within range of the heater-based resonance control system, a high-power test has been conducted on a 499 MHz cavity. The results for both are shown in Fig. 33.

TABLE VIII. Shunt impedance for 499 and 749.5 MHz cavity designs and required cavity phase relative to zero crossing.

Parameter	Value
499 MHz cavity shunt impedance (Ω)	2.10×10^8
749.5 MHz cavity shunt impedance (Ω)	1.04×10^8
1–5 pass horizontal beam phase (radians)	$\pi/2$
5th pass vertical beam phase (radians)	$\pi/3$

TABLE IX. Power requirements for rf separators based on beam energy, deflection angle, and the number of cavities per pass.

Pass	Number of cavities	Angle per cavity (μrad)	Total angle (μrad)	Energy (MeV)	Power at cavities (W)	Cavity power (W)
1	1	221	221	2303	1238	1238
2	2	116	232	4483	2553	1276
3	2	116	232	6663	5695	2848
4	3	81	243	8843	7305	2435
5	4	40	158	11 023	7291	1823
5V	4	62	248	11 023	11 861	2961

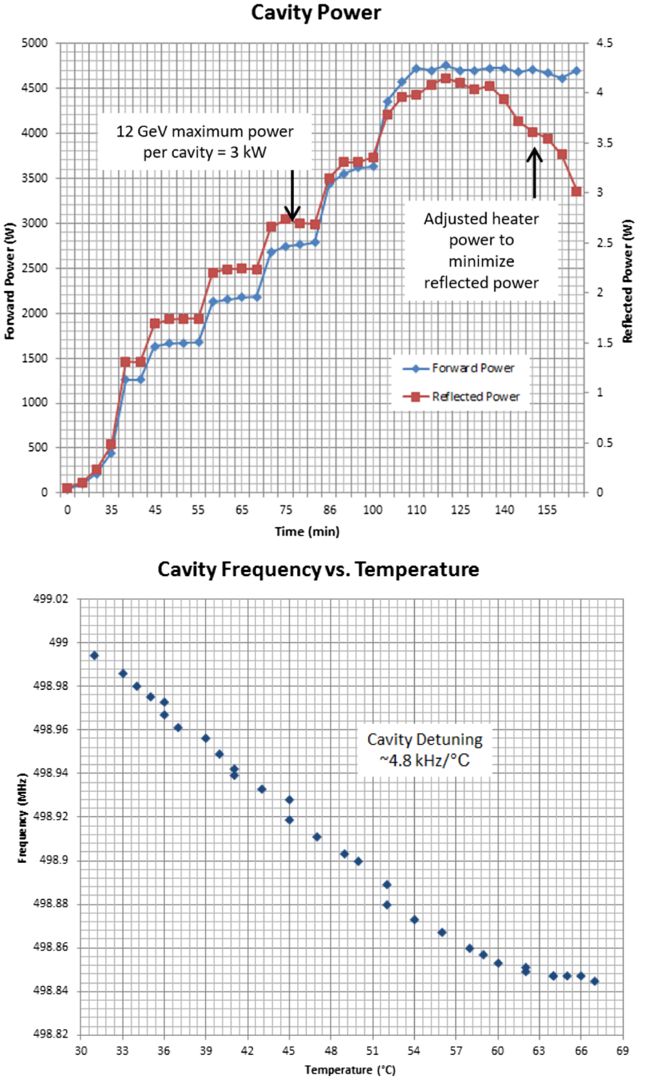

FIG. 33. Power ramp ending in a 1-h high-power run at 4.7 kW (upper) and cavity frequency versus temperature curve (lower).

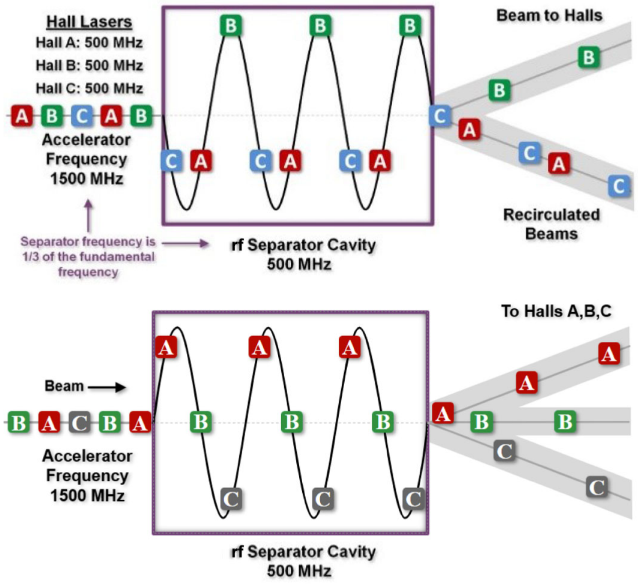

FIG. 34. Schematic showing how beams are interleaved, separated, and delivered to each experiment hall for first through fourth pass horizontal extraction and for fifth pass vertical extraction. Configuration when hall D not receiving beam.

The required phase relationship for the 499 MHz horizontal and vertical extraction systems is shown in Fig. 34. The 749.5 MHz phase relationship has been shown earlier in Fig. 3. Typical horizontal and vertical separation on beam viewers is shown in Fig. 35.

FIG. 35. Viewers showing 16.5 mm of separation in front of the second pass YA thin septum (above) and three beams at their proper elevation at the entrance to the Lambertson magnet for halls A, B, and C (below).

rf amplifiers. The rf power solution for the initial 4 GeV CEBAF installation consisted of six 499 MHz modular solid-state amplifiers (SSA) each with their own low-level rf control module and capable of delivering 1 kW. The amplifiers were connected to the relevant ten cavities on the beamline that were required to support the pass configuration of the scheduled physics program. The maximum number of amplifiers needed at any one time was five allowing the sixth amplifier to serve as a hot spare. The connections were made through a patch panel system with each cavity being powered by a single amplifier.

To address obsolescence issues with the original 1 kW SSA systems and to support the higher power beam during the 6 GeV era, four 499 MHz 10 kW inductive output tube (IOT) systems, floating on a 20 kV dc high voltage deck, were installed. An example is shown in Fig. 36. These UHF rf transmitters provide power for the second through fifth pass cavities while components of the aging original solid-state system were retained to power the first pass separator cavity. The output coupler for one of the 499 MHz IOTs was modified to operate at 749.5 MHz for the fifth pass horizontal system.

The IOTs are each connected to the multiple cavities of a relevant pass through a network of high-power splitters, phase shifters, circulators, and combiners as shown in Fig. 37. A procedure to optimize the phase of each cavity of the combined system relative to the beam has been developed. The system is first powered with cavities 2, 3, and 4 terminated into water-cooled loads. The LLRF controls are then used to find the zero-crossing phase that provides a rightward beam deflection with positive changes in the phase of the LLRF control module. The phase is determined by beam position monitors and viewers at the entrance of the YA thin septa for first through fifth pass horizontal systems and at the entrance of the Lambertson magnet for the fifth pass vertical system. Each of the remaining cavities is then incrementally reconnected to the system with their phase shifter used to return the system to the same zero crossing. The mechanical phase shifters have a limited range of 175° at 499 MHz and 225° at 749.5 MHz. If the proper setting is out of reach, a piece of hardline is inserted to center the phase-shifter zero-crossing response. There have been operational challenges with the 749.5 MHz rf system related to thermal management in the

FIG. 36. The 20 kV high voltage enclosure and controls above and a pair of 10 kW IOTs with their controls below.

rf distribution system as well as long-term amplitude and phase drift in the power delivered to each cavity.

Two additional upgrades for the rf power systems have been accomplished to complete the overall program. Funding from the American Recovery and Reinvestment Act (ARRA), secured in 2013, was used to build an addition to an existing service building and to procure and install four 499 MHz 10 kW solid-state amplifiers for the fifth pass vertical rf separators. An additional unit was purchased in 2018 to power the first pass horizontal system and to retire the original 1 kW solid-state amplifiers. In addition, ARRA funding allowed a 499 MHz superconducting deflector to be built and cold tested [142,143]. The cavity achieved a transverse voltage of 3.3 MV with peak surface fields of 32 MV/m and 49 mT [144].

3. *Magnets*

The extraction system magnet upgrade has been accomplished through the reuse of existing YA/YB septa and BP/BQ dipole magnets. The YA and YR magnets are relocated and outfitted with modified vacuum chambers, two new YA magnets have been fabricated, and new JG and JH dipole magnets have been developed and fabricated for the extraction chicanes. All new magnets are measured for field integral and field quality as described in Sec. III D. In addition, a long-standing error in the $\int BdL$ of the BP and BQ magnets has been corrected through the addition of $1''$ shims to lengthen the magnets. The magnet transitions for third through fifth pass, design bend angles, and integral field strength are shown in Table X.

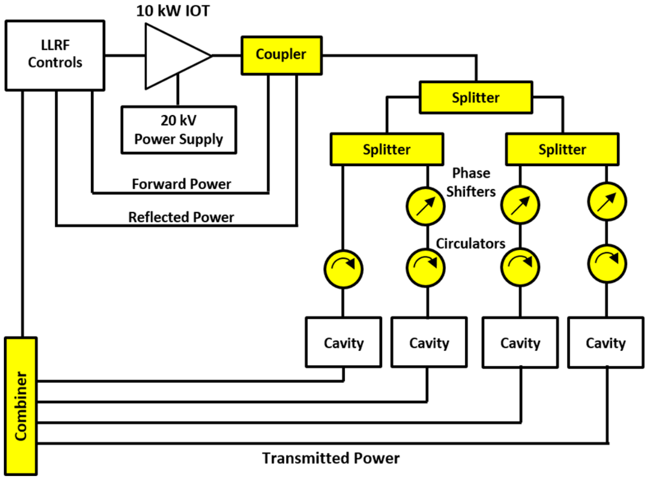

FIG. 37. rf distribution system for the 12 GeV Upgrade IOT systems.

I. Beam diagnostics

The beam diagnostics upgrade consists of adding devices to the new beamlines in arc 10 and hall D and to the modified spreaders and recombiners. The solutions deployed are a mix of replicating existing hardware, using existing solutions with some upgrades to beamline devices and electronics, and developing new components. The details for each system are discussed in the following sections. Table XI lists the total number of devices and the locations where they have been installed for the upgraded facility. Table XII lists the operational range, precision, and accuracy specifications for the various diagnostic systems.

1. *Beam position monitors*

The 6 GeV CEBAF beam position monitor (BPM) configuration included 450 antenna-style beam position monitors consisting of two different types of a similar design [145]. They had four thin quarter-wave antennae symmetrically placed around the beam and oriented at 45° from the normal x-y axes to avoid false signals being induced from synchrotron radiation in the bend planes. A schematic representation of an M15 BPM can is shown in Fig. 38. The majority of BPMs were installed on girder assemblies with the BPM located immediately upstream of a quadrupole. The M15 style was installed in all locations with the exception of the first two recirculation arcs, the

TABLE X. Physical parameters, design bend angles, and the integral field strength for the 12 GeV extraction magnets.

Pass	Energy (MeV)	4 GeV/6 GeV	12 GeV	Magnet type	Length (m)	Septa (mm)	Total angle (mrad)	Total B-dL (G-cm)
3	6600.67	YA	2 YA	Septa	1	5.0	−1.876	−41694
		YB	YR	Septa	2	31.5	−39.675	−881791
		BP	2 JG	Dipole	2		81.335	1807710
		BQ	JH	Dipole	1		−37.767	−838389
4	8760.40	YA	2 YA	Septa	1	5.0	−1.876	−55336
		YB	YR	Septa	2	31.5	−39.675	−1170444
		BP	2 JG	Dipole	2		81.335	2399202
		BQ	JH	Dipole	1		−37.767	−1113989
5	10920.13	YA	2 YA	Septa	1	5.0	−1.701	−62536
		YB	YR	Septa	2	31.5	−39.20	−1441336
		BP	2 JG	Dipole	2		81.335	2988452
		BQ	JH	Dipole	1		−37.767	−1388522

TABLE XI. Added beam diagnostics inventory and installed locations for the 12 GeV CEBAF Upgrade.

Diagnostic system	Injector	Arcs and extraction	Spreader and recombiner	Hall D	Total
Antenna BPM	2	38	22	0	62
Stripline BPM	0	0	0	26	26
Nano-amp cavity BPM	0	0	0	2	2
Wire scanner	0	2	0	4	6
Beam viewer	0	5	6	6	17
Synchrotron light monitor	0	1	0	2	3

TABLE XII. Specifications for CEBAF diagnostics.

Device type	Operating range	Precision/accuracy
Antenna style Beam position monitor	Position: -8 mm $< x/y < 8$ mm Transport style: current: 50 nA $<$ I $<$ 200 μA Linac style: current: 1 μA $<$ I $<$ 2 mA	30 μm/100 μm
Stripline Beam position monitor	Position: -8 mm $< x/y < 8$ mm Current: 10 nA $<$ I $<$ 200 μA	30 μm/100 μm
rf cavity nA Beam position monitor	Position: -12 mm $< x/y < 12$ mm Current: 100 pA $<$ I $<$ 1 μA Beam size: $\sigma_{x/y} < 4$ mm	100 μm/300 μm
rf cavity nA Beam current monitor	Position: -12 mm $<$ x/y $<$ 12 mm Current: 60 nA $<$ I $<$ 1 mA Beam size: $\sigma_{x/y} < 4$ mm	100 nA/1 μA
Wire scanner	Position: -10 mm $< x/y < 10$ mm Current: 2 μA $<$ I $<$ 50 μA Beam size: 25 μm $< \sigma_{x/y} <$ 4 mm rms width: 25 μm $<$ width $<$ 4 mm	10 μm/10 μm (both apply to sigma)
Fluorescent screen beam viewers	Position: -12 mm $< x/y < 12$ mm Current: 100 pA $< I <$ 50 μA Beam size: $\sigma_{x/y} < 4$ mm	500 μm/1 mm
Synchrotron light monitor	Position: -12 mm $< x/y < 12$ mm Current: 1 nA $< I <$ 1 mA Beam size: 100 μm $< \sigma_{x/y} <$ 4 mm	10 μm/10 μm (both apply to sigma)

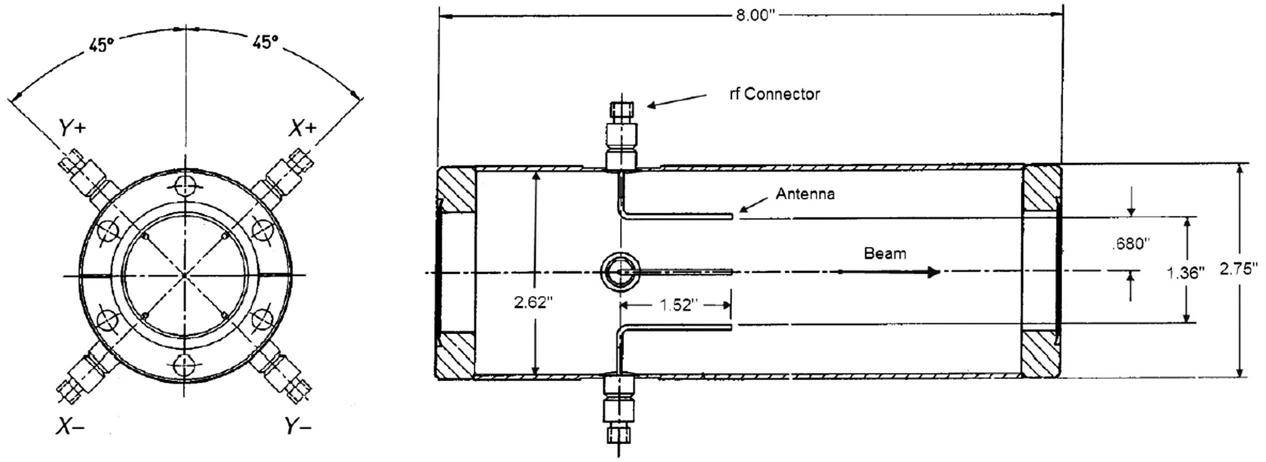

FIG. 38. Schematic for M15 antenna-style beam position monitor. M20 BPMs have a larger diameter with the same length.

extraction regions, and in spreaders and recombiners. In these locations, an M20 BPM with an increased bore was used to accommodate the larger beam tubes in these dispersive sections of the accelerator. The M20 was mounted to a pair of 4-5/8″ conflat flanges and has an inner bore of 1.87″ compared to the 2-3/4″ flanges and 1.36″ inner bore of the M15 design.

The original requirements for the BPM system were to detect beam currents from 1 to 200 μA for cw beams as well as 60 Hz tune mode pulses as short as 100 μs with an average current of 10 μA. The position resolution specification was 100 μm. The first generation of electronics implemented to meet these specifications was a CAMAC-based heterodyne solution referred to as the four-channel or transport BPM system [145]. To first order, the performance of the four-channel system was sufficient in the early years of commissioning and operating CEBAF. Correcting some limitations in the original system and the need to add new features led to the development of the VME-based switched electrode electronics (SEE) system [146].

For example, the four-channel system suffered from drift in the gain between plus and minus channels (see Fig. 38) for each rotated plane. The total five-pass linac beam current specification is from 1 to 1000 μA and the four-channel system lacked the required dynamic range for these beam currents. There was a need to distinguish the beam orbit for each of the linac passes during tune-mode operations. Finally, there was an emerging need to incorporate a high-speed data acquisition system suitable for use as a time domain diagnostic and to support the development of feedback systems for correcting ac line harmonics.

To mitigate gain drift between plus and minus channels, the SEE system switches between the pairs of antenna at 120 kHz and uses a single electronics circuit for detection. Figure 39 provides a representation of the CEBAF 60 Hz tune-mode current structure, showing a 250 μs macropulse and a 4 μs linac “snake” pulse after a 100 μs delay. Most of the beam diagnostic systems are triggered to take data 65 μs after the leading edge of the 60 Hz macropulse. The one-pass transit time around CEBAF is 4.237 μs. To allow for independent pass position measurement using the successive 4 μs current pulses as they snake through the linacs, the system timing of the linac-style SEE electronics is tuned to take readings delayed by the machine recirculation period for each successive pass. The transport-style systems include a multiplexer connecting the in-tunnel rf modules of vertical stacks of ARC BPMs to a service building VME chassis. Specifications for both linac and transport-style electronics are shown in Table XII. The SEE

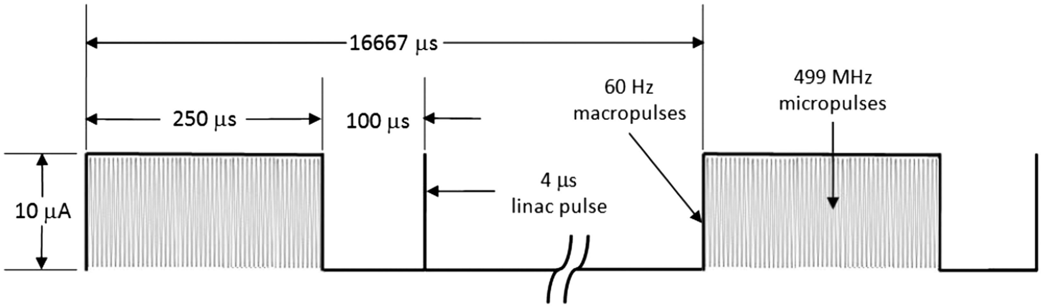

FIG. 39. Tune mode 250 μs 60 Hz macropulse current structure followed by the linac 4 μs snake pulse.

TABLE XIII. Regions where SEE BPM electronics are installed and the installation periods.

SEE install year	Regions upgraded
1995	North and South Linac Spreader and orbit locks for East arcs (1, 3, 5, 7, 9), hall A
1998	Injector and spreader orbit locks for West arcs (2,4,6,8), halls B and C
Mid to late 2000s	Transport recombiner Remaining segments in West arcs

BPM system was designed in 1994 and then implemented in the accelerator segments as shown in Table XIII.

The 12 GeV BPM upgrade encompassed two main technical approaches. First, a mix of M15 and M20 style BPMs are added to the existing SEE electronics systems. The majority of these systems are located in the new arc 10 and in the modified spreaders and recombiners. Two more BPMs are added in the injector segment. There are 62 total BPMs installed in the locations summarized in Table XI.

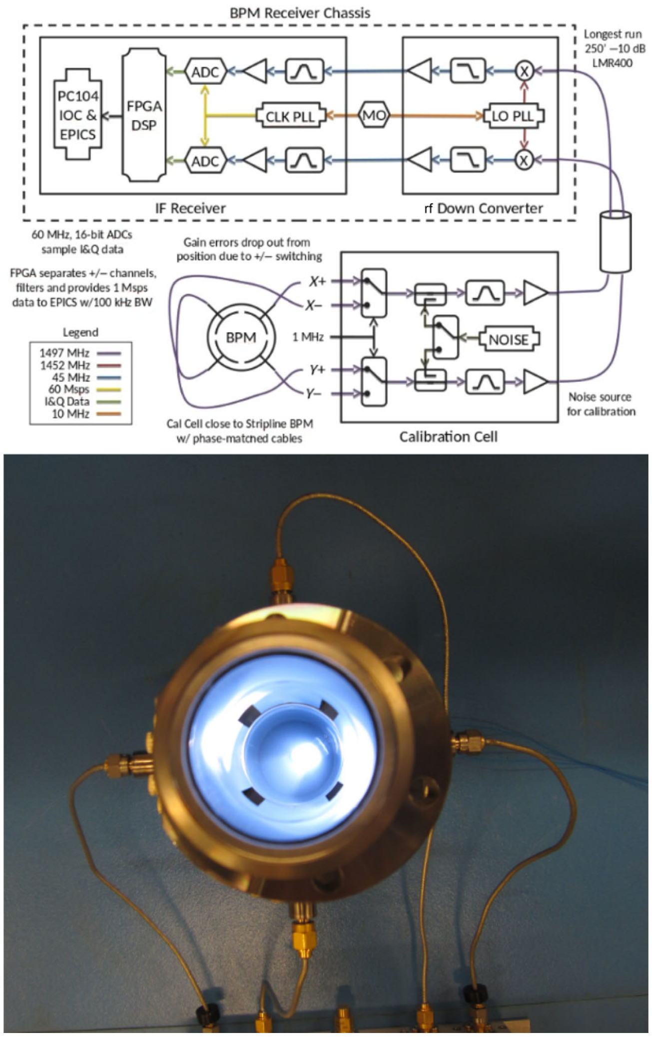

FIG. 40. Schematic view of the digital diagnostic receiver (DR) and an image of a stripline beam position monitor developed for the hall D beamline.

Second, as shown in Fig. 40, a new diagnostics receiver (DR) and stripline BPM have been developed to meet the low beam current specification of less than 1 up to 5 μA for the Hall D beamline. The three main blocks of the system are as follows: (i) a calibration cell that includes a multiplexer to switch between pairs of wires at 1 MHz, a preamplifier block to amplify the 1497 MHz signals before sending them to the service building and a noise source to calibrate the system; (ii) an rf downconverter, filter, and amplifier block to lower the signal frequency to 45 MHz and condition it for the next stage; and (iii) a digital IF section, which filters, samples, demultiplexes, demodulates, and performs CEBAF-specific functions related to beam delivery, including a PC-104-based IOC tied to the EPICS control system. The 1452 $(= 1499 - 45)$ MHz LO is tied to the 10 MHz CEBAF Master Oscillator.

The new stripline BPM is a precision-machined component that registers the pickups more accurately as compared to the M15 and M20 antenna designs. About 26 of these devices and their diagnostics receiver (DR) chassis are installed in the hall D beamline. The system is capable of providing position readbacks with a good signal-to-noise ratio starting around 10 nA. The hall D physics program requires beam currents below this threshold for production running as well as for calibration of their total absorption counter (TAC) at a few nanoamps of beam current. For these conditions, two nA-style BPMs, described in the next section, have been implemented.

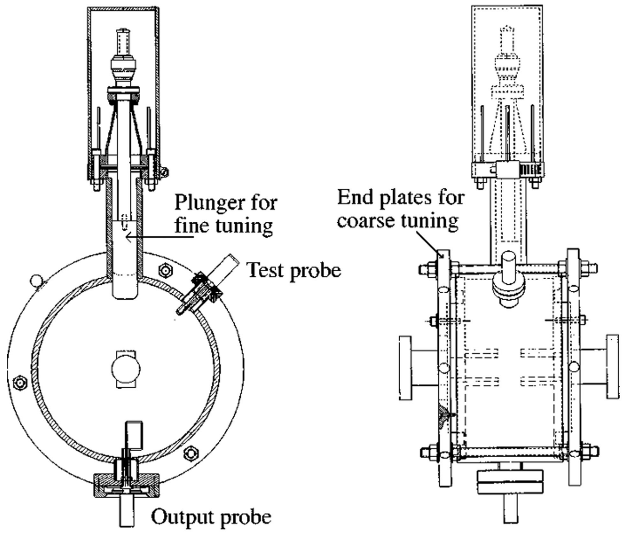

FIG. 41. Schematic of the nA BPM position cavity with 3 cm rod gap.

TABLE XIV. nA BPM cavity specifications.

Parameter	Specification
Operating range	1–1000 nA
BPM resolution	70 pV/m at 1 nA
Position measuring range	$\vert x\vert$, $\vert y\vert \le 5$ mm
Resonant frequency	1497 MHz
Loaded Q	3500
Beamline aperture	3.0 cm
Diameter	19.0 cm
Depth	9.5 cm
Rod gap	3.0 cm
Material	Copper plated stainless

2. Nano-amp BPMs

A system of low-intensity beam position and current monitors capable of operating in the current range of 1 nA–1000 nA was developed in 1996 for hall B [147]. Initial attempts to extend the dynamic range of the stripline BPM system by a factor of 30 for this application were unsuccessful due to limitations in the electronics architecture. A cavity BPM design was adopted that is conceptually similar to the rf separator design described earlier.

Each nA BPM system consists of a pair of position-sensitive pillbox cavities with field perturbing rods operating in a dipole mode oriented for horizontal and vertical measurement and a simple current-sensitive pillbox cavity to normalize the signals from the position-sensitive cavity pair. The requirements for the system are listed in Table XIV. The mechanical design for the 1497 MHz position-sensitive cavities is shown in Fig. 41. The cavity is coarsely tuned by adjusting the end plate spacing and a plunger system is then used for fine-tuning the input coupling. Each cavity has an output coupling loop and a test probe for independently measuring field strength. The four rods are spaced 3 cm apart transverse to the beam axis. The current-sensitive cavities are a similar design without the field-perturbing rods. The three-cavity system is installed as a unit in a temperature-stabilized enclosure as shown in Fig. 42 (lid and thermal blanket not shown).

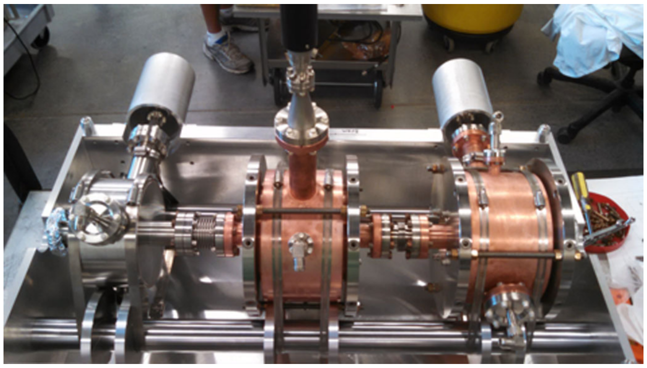

FIG. 42. Three-cavity nA BPM system mounted in its thermal enclosure.

In the electronics, the 1497 MHz signal from each cavity is amplified, mixed with a 1497.1 MHz local oscillator (LO) to down convert to 100 kHz and then processed by a lock-in amplifier. The 100 kHz reference, LO, and 1497 MHz test signal are all generated in an external reference module, which is tied to the CEBAF Master Oscillator.

For the 12 GeV upgrade, two of these nA BPM systems are installed at the top of the ramp in hall D, upstream of the photon radiator and tagger magnet to optimize the position and angle of the electron beam before hitting the photon radiator.

3. Wire scanners

The use of wire scanners to measure transverse beam size and absolute position, and thereby to infer beam emittances, energy, and energy spread, has been in place at CEBAF since the initial operations [148,149]. The majority of the early systems in the main accelerator used CAMAC architecture for controlling stepper motors and reading back beam induced wire signals. During the 6 GeV era, the controls began migrating toward VME solutions, retiring the CAMAC systems with some remaining at the start of the 12 GeV Upgrade.

Wire scanners in the main accelerator are primarily used to match the beam to the design optics at three different energies in the injector, in the matching section preceding each recirculation arc, and at the entrance of each hall beamline as described in Sec. IV C. In addition, wire scanners are used upstream of targets in the halls to optimize the beam spot size and convergence for the experiments.

The 12 GeV upgrade for wire scanners consisted of three parts: (i) developing a more robust fork assembly that uses retaining screws as opposed to gluing the wires to a metal frame (Fig. 43), (ii) building and installing six new wire scanner assemblies, (iii) developing an upgraded electronics package for hall D and propagating that solution around the accelerator to replace existing CAMAC and VME systems [150]. The new assemblies were deployed to match the beam at the entrance to arc 10, measure the spot size and position at the end of the northeast spreader beamline for

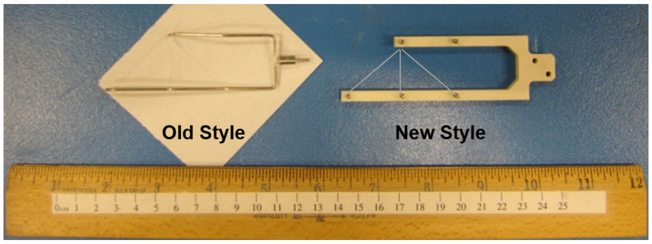

FIG. 43. Wire scanner with metal fork and glued wires and the upgraded polymer fork using retaining screws for stability.

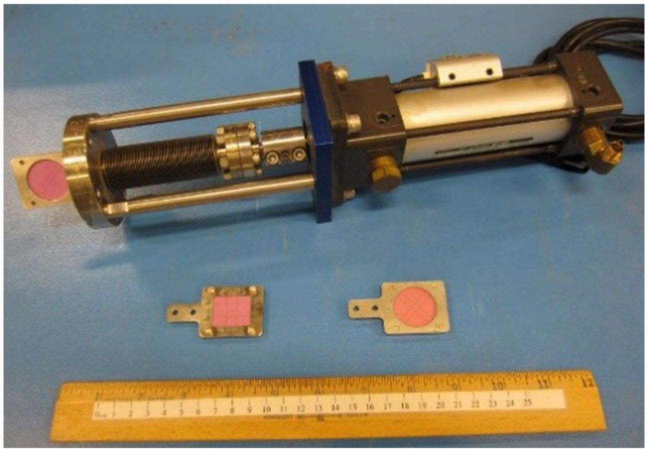

FIG. 44. Pneumatic viewer assembly and an extraction and standard viewer flag.

hall D, and match the beam at the entrance of the hall D ramp. Two additional systems are deployed for matching the beam at the top of the hall D ramp for projecting the convergence of the photon beam onto the physics target in the hall and for measuring the spot size at the hall D beam dump.

The new electronics chassis is capable of driving up to eight wire scanners and includes stepper motor drivers, power for preamplifiers, and data acquisition for wire signals from either digital encoders or analog linear potentiometers. The FPGA-based main controller board includes a PC/104 computer running EPICS as a local IOC.

4. Viewers

The CEBAF beam viewers are fluorescent screens that emit optical light, which is then focused onto CCD cameras. Beginning in the 6 GeV era, the material used was Chromox-6, an alumina-doped ceramic material from Morgan Technical Ceramics. Prior to the upgrade, there were 125 viewers in CEBAF. All but the extraction viewers are 28.45 mm diameter ×0.25 mm thick discs mounted to a 25.4 mm diameter frame. In each linac, six of these were installed on every fourth girder between cryomodules. They were modified to have a hole in the center used for threading the lower pass beam to allow imaging of the next pass on the viewers. The extraction viewers are shown in Fig. 35 of Sec. III H. Shown in Fig. 44 is a standard pneumatic viewer assembly and viewer flags.

For the 12 GeV upgrade, 17 new viewers have been installed as follows: one extraction-style viewer in front of the fifth pass YA magnets, five viewers at zero dispersion points in the new arc 10 beamline, one at the arc 10 recombiner, two in the northeast spreader hall D beamline, five in the new hall D beamline, one at the hall D beam dump, and finally, two in the transport recombiner after the fifth pass.

The 6 GeV spreader and recombiner design used pairs of 2-m YR septa magnets to separate fourth and fifth pass beams. In the transport recombiner, a viewer system was designed to show both fourth and fifth pass beam trajectories between the septa pair. The 12 GeV design requires 3-m ZA septa with a larger separation between fourth and fifth pass trajectories. Figure 45 shows the original viewer flag with nominal beam positions and the new design trajectories for fifth pass. The system has been modified for the 12 GeV beam paths.

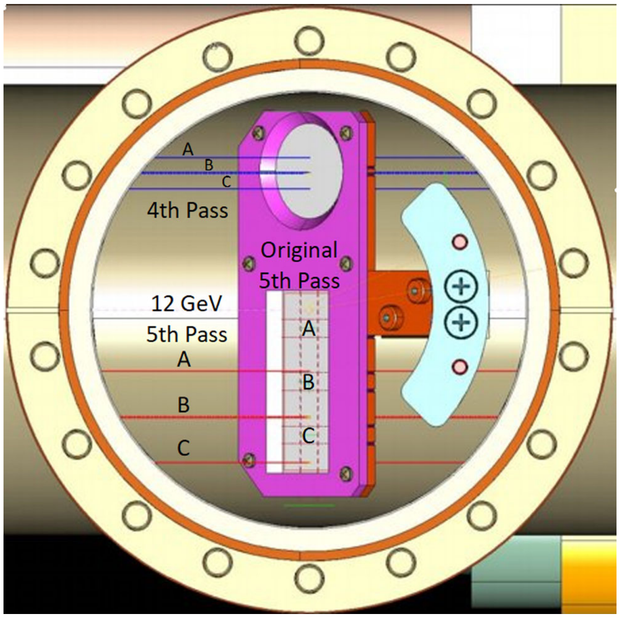

FIG. 45. 6 GeV transport recombiner viewer diagram with shifted 12 GeV trajectories shown for fifth pass.

5. Synchrotron light monitors

Since 1986, there were plans to use synchrotron light monitors in CEBAF [151]. Throughout the 6 GeV era, we have routinely used these devices to monitor energy stability, energy spread, and intrinsic spot size at multiple locations. Leading into the 12 GeV upgrade, there were three synchrotron light monitors in the CEBAF main accelerator that were in routine use; at the exit of the injector chicane dipole 0R02, at the high dispersion point in arc 1 after dipole 1A09 and at the high dispersion point in arc 2 after dipole 2A09. The dispersion at these locations was 1.26 m for the injector location and 6.5 m in the arcs.

Using synchrotron light monitors to measure Twiss parameters was also considered in the early days of CEBAF [152] and realized with the installation of systems at four homologous points in arc 7 [153].

These systems worked reasonably well, but the 12 GeV upgrade provides an opportunity to develop a new modular design that could drop into any location around the accelerator. The images in Fig. 46 capture the details of the new design. The new system is lightweight, low cost, rugged, easy to fiducialize offline and then align in the

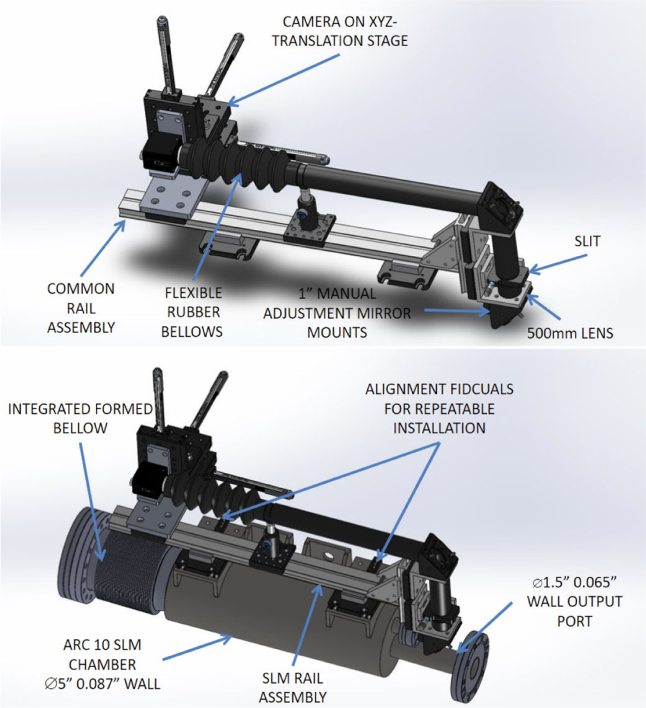

FIG. 46. Modular SLM assembly on rail system and mounted to the arc 10 vacuum chamber.

tunnel, and can be installed without modifying any existing dipole vacuum chambers [154].

For the 12 GeV upgrade, three new synchrotron light monitor assemblies are installed in arc 10 at the exit of the 4 m dipole, in the northeast spreader at the exit of MXLBS08, and after the second vertical-bend dipoles at the bottom of the ramp into hall D. The same design replaces the three existing 6 GeV systems. All of these devices are in dispersive locations and provide energy stability and energy spread information.

J. Machine protection system

The machine protection system (MPS) is designed to protect beamline and beamline components from damage due to beam strike events or other equipment failures, which may result in costly damage to machine components or radioactivation. The two main components of the MPS are the MPS Beam Containment system and the Fast Shutdown (FSD) system. The MPS Beam Containment system detects both acute and chronic beam loss events and is made up of a collection of beam monitoring devices strategically placed around the machine. The FSD is a network collecting and evaluating beam loss monitoring signals and triggering fast beam shutdown devices to terminate the beam.

1. Beam containment system

The main function of the beam containment system is to prevent beam damage to machine components due to acute beam loss. Secondarily, the system supports minimizing the radioactivation of beamline components by reducing low levels of beam loss. The beam containment system employs a variety of detectors and subsystems to monitor and react to beam loss around the CEBAF facility. These include (i) the beam loss accounting (BLA) system, (ii) machine protection beam loss monitors (MPS-BLM), (iii) diagnostic beam loss monitors (DIAG-BLM), and (iv) beam loss ion chambers (BLIC). It is important to note that the beam containment system is layered. The BLA system is able to detect a gross beam loss greater than 2 μA, while BLMs protect the accelerator beamline and its components from low-level beam loss in the range from 10 nA to 2 μA.

Beam loss accounting. In the BLA system, the average current out of the injector is measured by an rf cavity current monitor and compared to the current measured similarly in each of the experiment halls. When the summed total current measured in the halls is 2 μA less than the injector measurement, the beam is shutdown. The original design of the BLA system was suitable to the requirements for 12 GeV operation and only needed expanding to cover the new hall D point of beam delivery.

Beam loss monitors. Beam loss is detected throughout the CEBAF site by promptly detecting the radiation generated by a beam strike using photomultiplier tubes. The addition of new machine segments and the increase in beam energy triggered the extensive review of the beam loss monitor network. As a result of the analysis, the location and quantity of both FSD-interlocked BLM tubes and beam diagnostic BLMs changed around the machine. The count of FSD-interlocked BLMs increased from 45 to 70, while the count of diagnostic BLMs decreased from 111 to 94. The overall machine coverage provided by the BLMs significantly improved through this effort. At the same time, newly redesigned BLM cards were installed that added flexibility in machine protection configuration and diagnostic capabilities [155]. In developing the new BLM hardware, Jefferson Lab took the opportunity to migrate to a VME-based system using FPGAs as shown in Fig. 47.

Beam loss ion chambers. Ion chambers are used to protect areas with a high ambient radiation environment like high power dumps and target systems. While there were no significant changes in the type and number of ion

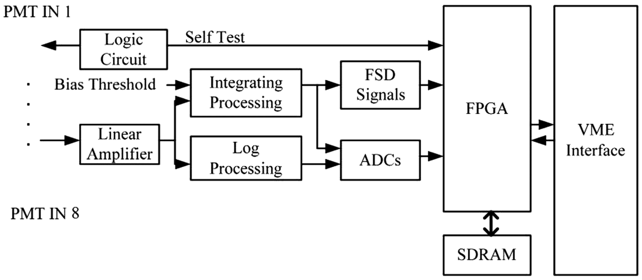

FIG. 47. The system block diagram of the BLM board (from [155]).

chambers due to the 12 GeV upgrade, it is worth noting the use of ion chambers for protecting the high power dump diffusers in halls A and C. In each location, there are two dedicated ion chambers monitoring the backscatter of radiation from the high-power dump diffusers. With the help of specialized FSD cards, these ion chambers cause the FSD system to trip if radiation levels are lower than expected as this condition indicates burnthrough of the dump's diffusers and turning the beam off protects the dump from catastrophic failure. This mode is the opposite of the "trip high" condition normally associated with ion chambers.

Beam envelope limit system: Beam envelope limit system (BELS) is a high reliability PLC-based system [156], which ensures that CEBAF runs within accelerator operations and safety power limits. For 12 GeV CEBAF, the operations envelope (the maximum beam power in normal operations) is 1.1 MW and the safety envelope (the maximum power which if exceeded causes significant administrative burden) is 1.3 MW. This system provides a tiered reaction to exceeding 1100 kW utilizing different beam shutdown methods for each (i) operator warning after 1 min, (ii) control system shutdown after 5 min, (iii) MPS shutdown after 10 min and finally, (iv) the personnel safety system will terminate the beam after 15 min.

The calculated total CEBAF power is the sum of power delivered to individual beam destination segments as calculated based on the beam energy and actual beam current delivered to these segments. Since hall D is a low-power beam destination (with an FSD-monitored power limit of 60 kW), as is hall B (55 kW), the power delivered to hall D is not monitored by the BELS system and the addition of hall D did not trigger significant modification of the system. The increased beam energy delivered to halls A and C required only the modification of BELS software configuration parameters to allow operating at 12 GeV.

2. Fast shutdown system

The FSD system is a network of electronic cards (nodes) strategically located throughout the CEBAF facility. The nodes form a tree structure with the cards aggregating input signals and propagating them to the top-level FSD node in the injector segment, which controls the beam shutoff. When the FSD system is triggered by a beam loss event, the system responds by shutting off the electron beam in less than 50 μs. Control software provides the ability to mask the FSD input signals, allowing for easy and flexible but reliable FSD system configuration according to changing beam delivery destinations or changed conditions in the segmented CEBAF structure.

For the 12 GeV upgrade, the existing FSD infrastructure has been expanded to integrate new areas but did not change significantly beyond that. The upgrade did not require any new FSD input types and response time of the existing FSD cards and their network is sufficient to meet the beam shutoff requirements with the higher energy electron beam.

The new digital low-level rf controls for the C100 cryomodules are designed to produce summary output FSD signals covering quench, arc, IR, and vacuum (waveguide and beamline) fault detection. These fiber optic 5 MHz FSD summary signals feed directly from each new rf zone into dedicated FSD input cards installed, respectively, in the North and South Linacs. Summary of FSD signals from the Linacs further travels to the Master FSD card in the injector segment.

Protection of the beamline and new hardware installed in the hall D and hall D tagger segments required extension of the FSD system. This new installation utilized VME-based FSD cards. Similar to other segments, there is a local master FSD card aggregating FSD signals from all local sources within hall D, and the aggregated summary is sent to the master FSD card in the injector segment.

K. Site cooling and power upgrades

To support the 12 GeV upgrade, new and upgraded cooling and electrical systems are needed to meet the 12 GeV project requirements. Included are modifying the existing low conductivity water (LCW) systems and the CHL condenser water system, installing a new passive chilled beam system in the accelerator tunnel, providing new utilities for the new experimental hall (hall D), and extensively upgrading and improving CEBAF's electrical power system. Table XV summarizes the new total design values after the upgrade.

There are four low conductivity water (LCW) systems that were upgraded to support the 12 GeV project.

TABLE XV. CEBAF cooling and power systems requirements after 12 GeV upgrade. gpm stands for gallons per minute water flow rate.

Location	LCW system (gpm)	Condenser water (gpm)	Chilled water (gpm)	Power—new unit substations
Accelerator	5600	4900	200	3 MVA (4 ea) 2 MVA (1 ea) 1.5 MVA (1 ea)
CHL		3100		5 MVA (2 ea)
Hall D	385	1120	600	2 MVA (1 ea) 1 MVA (1 ea)

TABLE XVI. LCW Systems in the 6 and 12 GeV eras.

Load	West arc LCW system (gpm)	North linac LCW system (gpm)	East arc LCW system (gpm)	South linac LCW system (gmp)
6 GeV flow	660	955	453	987
12 GeV magnets	212		34	
12 GeV rf zones and power supplies		903		891
Total 12 GeV gpm				
Required	872	1858	487	1878
Design capacity	1000	2000	600	2000

The systems have been expanded to provide cooling for new and upgraded magnets, the additional rf zones, and the additional power supplies. Table XVI shows the 6 GeV operational capacities and the new 12 GeV design flow capacity. All LCW systems provide 2 MΩ water at 95 °F.

The 12 GeV upgrade requires 4 times more cooling at the bending magnets than was required for 6 GeV operations. The heat generated from these magnets must be removed to allow personnel access to make equipment repairs within 1 h of interrupting magnet operations. Ambient air temperature of 95 °F is specified; without air conditioning, tunnel temperatures could exceed 135 °F. The new air conditioner is a natural convection noncondensing cooling system. It consists of chilled water systems (located above ground) providing chilled water to 132 chilled beams (cooling radiators) mated with required automated controls and provides tunnel cooling without producing condensation. Each chilled beam requires 1.5 gpm of chilled water and is $96'' \times 20'' \times 12''$ as shown in Fig. 48. Each of the air conditioning systems for each arc produces 60 tons of aggregate cooling and has been in operation for several years. The chilled water system maintains tunnel air temperature contributing to overall accelerator stability and worker safety.

Figure 49 shows a one-line diagram of the electrical distribution system at 6 GeV (shown in black) with the

FIG. 48. Photograph of chilled beams of the air conditioning system next to the east arc magnets.

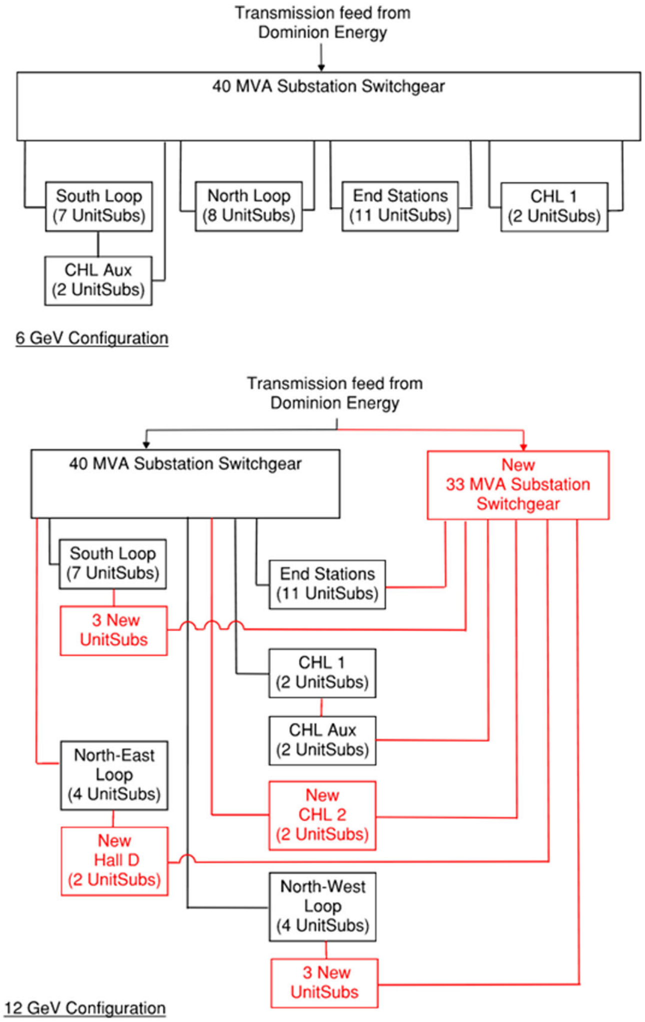

FIG. 49. Electrical power distribution comparing 6 GeV and 12 GeV CEBAF.

modifications for 12 GeV shown in red. An additional 33 MVA substation switchgear was added to the existing Dominion Energy (formerly Dominion Virginia Power) overhead transmission line feed to accommodate the additional power requirements for the 12 GeV upgrade as well as to provide a more reliable and robust 15 kV distribution system. During the 6 GeV era, all the power for the accelerator site was fed from the 40 MVA primary substation switchgear through four 15 kV loops; the south loop, the north loop, the CHL loop, and the end-station loop. The new 12 GeV site power distribution included adding six new unit substations to the existing north and south loops. The north loop was split into a northeast and northwest loop with the two new unit substations for the hall D complex added to the northeast loop. The CHL Aux unit substations were moved to the CHL1 loop, and the CHL2 loop was created with the two new 5 MVA unit substations.

Additional electrical power was added for the new high-power amplifiers (HPAs) and the additional rf zones in each of the North and South Linac Buildings as outlined in Table XV. A new 1.5 MVA unit substation was provided at the east end of the North Linac Building to account for this power need. A new 2 MVA unit substation was provided at the west end of the South Linac Building to meet the additional power needs as well as providing additional box power supply power in the supporting west arc service building (W2) with a standard operating headroom of 30%. New feeders run from each unit substation to a new switchboard in both the North and South Linac Buildings.

All magnet power supplies were refed to the newly installed unit substations and indoor switchboards. The existing switchboards that previously supported the power supplies during 6 GeV operations were rewired and used to power the upgraded LCW equipment, cooling towers, and chilled water systems.

IV. OPERATING CEBAF AT 12 GEV

In this major section, we summarize three significant aspects of 12 GeV CEBAF project performance: results for the newly installed cavities; effects of particulate movement around the CEBAF accelerator and its results on cavity performance; and recent enhancements of operations procedures and software that have led to significantly improved accelerator tuning and overall reliability.

A. Installed C100 cavity performance

After each C100 cryomodule was installed in CEBAF, it was commissioned. SRF commissioning consists of a set of tests designed to quantify the performance aspects of the cavities that are most important in an operational setting. Commissioning tests are focused on determining maximum stable operating gradients and measuring field emission, dynamic heat loads (Q_0), and microphonics.

1. Determining the maximum gradient

The 12 GeV specification states that a C100 cryomodule must be capable of delivering a stable energy gain of 108 MV. Therefore, each cavity in a C100 cryomodule cavity must deliver, on average, a usable gradient of at least 19.2 MV/m. The first step in the commissioning process, once cavities have been mechanically tuned, is to determine the highest stable gradient available from each cavity.

The first step in gradient determination is to quantify the rf cable losses in order to calibrate rf power levels. Then, while running pulsed rf into the cavity, the gradient is calculated from the emitted power. The loaded Q (Q_L) is calculated at this time as well. The field probe calibration is then set so that gradient as calculated from the field probe power level is equal to the gradient as calculated from the emitted power. From this point on, the gradient derived from field probe power is used as the relevant gradient measure.

Once the gradient is calibrated, pulsed rf power is increased in small steps. C100 cavities will frequently go through a series of nonrepeating quenches as the gradient is increased. The process continues until the cavity reaches a limiting condition.

Potential gradient limitations include quenching, high dynamic heat loads, warm rf window temperatures, vacuum degradation in either the beamline or the waveguide guard vacuums, arcing in the guard vacuum, or finally the administrative limit of 25 MV/m. For the majority of C100 cavities, the final limitation is a repeatable quench. Most of the remaining cavities will be limited by rf heat load or by the administrative limit of 25 MV/m. This administrative limit is meant to protect the cavities from new field emitter creation. The current controls and available rf power would limit normal operation of these cavities to gradients lower than 25 MV/m.

Once the maximum gradient is defined, the limit is then tested using cw rf. When the absolute maximum gradient is known, the next step is to determine the maximum stable operating gradient. The maximum stable operating gradient is found by lowering the gradient below the maximum just enough to avoid fault conditions over the course of running the cavity cw at least an hour. This procedure provides an opportunity for the helium circuit and the beamline and waveguide guard vacuums to settle. Figure 50 shows the process of raising the gradient to determine the maximum gradient. In this example, the gradient has already been increased to roughly 20 MV/m. Over the next several hours, the cavity is pushed through a series of quenches in pulsed mode until a final maximum of approximately 23 MV/m is reached. Then, while running cw rf, it is determined that the rf heat load is too high above 20 MV/m and the gradient is lowered to a point where it will run stably. The red trace shows the 2K helium liquid level. Periods where the rf heat load exceeds the capabilities of the helium vessel's plumbing show large oscillations at

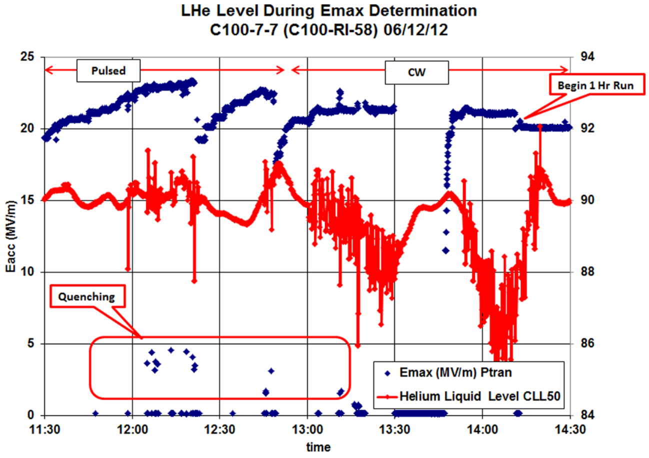

FIG. 50. Sample individual cavity $E_{\max}$ determination (from [104]). The blue curves give the cavity gradient and the red curves give the liquid helium level during the test.

the liquid level. During the last 15 min shown in the figure, the gradient has been turned down enough that the helium bath begins to stabilize and the 1 h run begins at 20.1 MV/m.

Finally, once Q_0 measurements of all the cavities in a cryomodule have been completed and the static and dynamic heat loads are known, a further optimization of gradients is completed. The optimization takes into account the 1 h run gradients along with heat load information and provides a set of gradients that allow for all eight cavities to operate at the highest stable gradients, while staying within the dynamic heat load budget of 240 W. Figure 51 shows the distribution of the absolute maximum gradients (red) and compares that with the distribution of final maximum operating gradients (E_{maxop}) after the optimization is completed (blue). The final maximum operating gradients are entered into machine operations software as a maximum operating gradient permitted for that superconducting cavity.

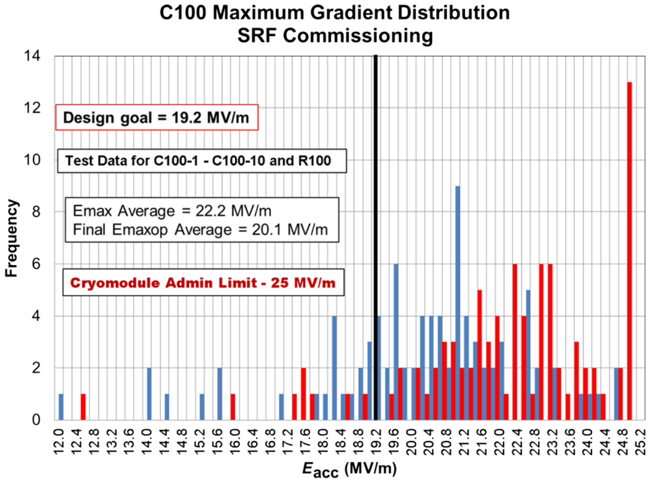

FIG. 51. Maximum operating gradients E_{maxop} both before (blue) and after (red) the optimization procedure.

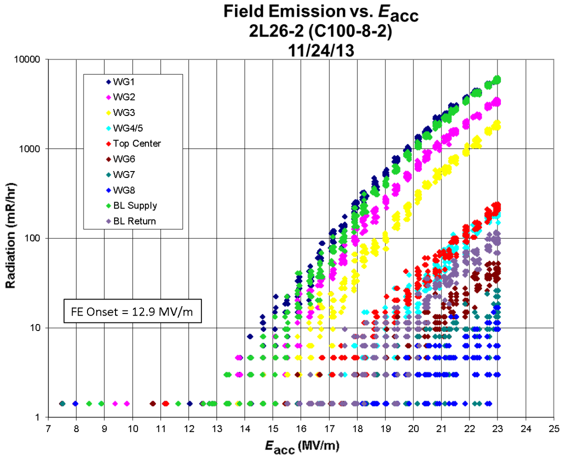

FIG. 52. Measured field emission count rate as a function of accelerating gradient for a typical cavity.

2. Field emission

After the E_{maxop} extended run is completed, measurements of x rays produced by field emission as a function of gradient are made. A set of 10 Geiger-Mueller (GM) tubes are placed on the cryomodule at several locations, including the beamline at either end of the cryomodule, and at the fundamental power couplers (FPCs) [104]. Figure 52 shows a set of measurements for a typical cavity.

Neutron production was measured during the commissioning of the first two cryomodules that were installed. This, however, has not been a routine measurement on all of the C100-style cryomodules as the necessary instrumentation was not always available. Figure 53 shows an example of neutron production.

Figure 54 shows the distribution of field emission onset gradients for the C100 cryomodules as measured during

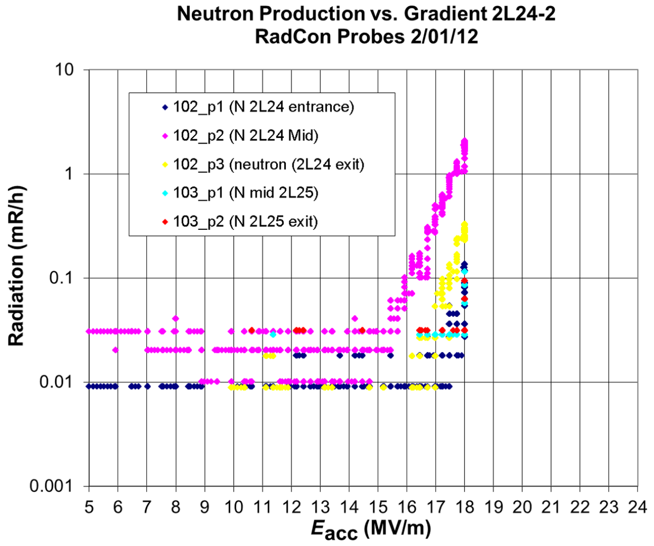

FIG. 53. Measured neutron production as a function of accelerating gradient for a typical cavity.

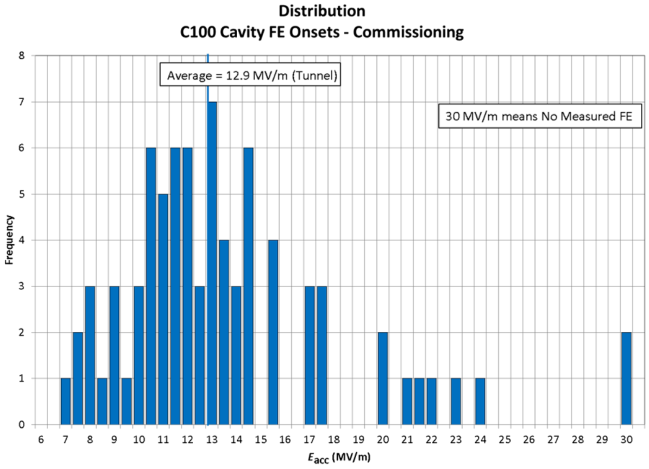

FIG. 54. Field emission onset gradients for 79 cavities in the initial complement of C100 cryomodules, as determined by measured radiation at a level of 1 mR/h.

initial commissioning. The average across all of the C100s and the R100 was 12.9 MV/m. The detector resolution of the system in use to measure the radiation meant that the criterion for onset gradient would be defined as the lowest gradient at which any of the channels measured a value of about 1 mR/h.

3. Q_0 and heat load

After the maximum gradients of stable operation for the individual cavities have been established, Q_0 is measured. The Q_0 is calculated from a calorimetric measurement of the power dissipated by the cavity into the helium bath. This is accomplished by isolating the cryomodule from the helium transfer lines and measuring the rate of rise of helium pressure with rf off, with a known heater power, and finally with rf on. This method can resolve power dissipation as low as 1 W [104].

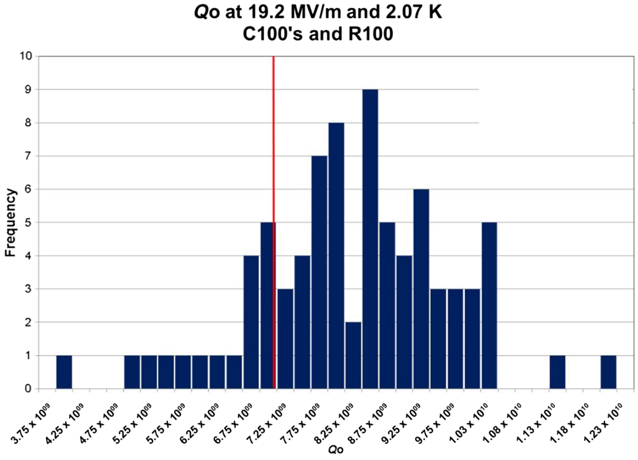

FIG. 55. Q_0 distribution for each C100 cavity at the lesser of E_{maxop} or 19.2 MV/m. The design goal was 7.2×10^9 and the average was 8.1×10^9.

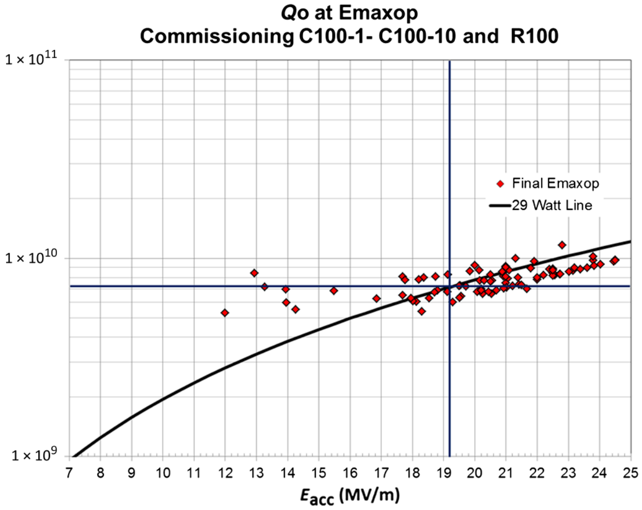

FIG. 56. C100 cavity Q_0 at maximum operating gradient. The vertical line is the upgrade project specification.

Figure 55 shows the distribution of measured Q_0 values at 19.2 MV/m for all C100s and the R100. Roughly, 25% of the cavities could not be measured at 19.2 MV/m due to gradient limitations. The average over all the cavities clearly exceeds the 12 GeV project requirements.

After the Q_0 versus E_{acc} data has been measured for all eight cavities in a cryomodule, an optimal set of maximum gradients can be defined that takes into consideration the extended run gradients and the heat loads measured at various gradients. This optimum is calculated within a constrained maximum allowable heat load per cavity of 35 W and a total heat load for all eight cavities of 240 W. Figure 56 shows the Q_0 for each cavity at the final E_{maxop} gradient. The black curve on this graph denotes the Q_0 that is equivalent to 29 W of dynamic heat load across a range of gradients. The crossed lines indicate the gradient and Q_0 specifications.

TABLE XVII. The cumulative operating voltage for each C100, all eight cavities per C100 operated simultaneously for at least 1 h.

Cryomodules	Voltage (MV)
C100-1	104
C100-2	120
C100-3	124
C100-4	105
C100-5	110
C100-6	113
C100-7	113
C100-8	109
C100-9	117
C100-10	116
R100	116
Average	113

A final step in the maximum gradient determination is to turn-on all eight cavities at the final E_{maxop} gradients. The cavities are then run for at least an hour in this configuration. Should the heat load be too high, a run of more than a few minutes is not possible. Table XVII shows the integrated voltages at which these eight cavity runs were accomplished for each new cryomodule. Only two cryomodules fell slightly short of the 108 MV goal and the average performance is comfortably above the 108 MeV 12 GeV project requirement.

4. Microphonics and tuning sensitivity

The 12 GeV project "budgeted" for 25 Hz peak total detuning (4 Hz static plus 21 Hz dynamic) based on the available klystron power (13 kW), the design Q_{ext} for the fundamental power couplers (3.2×10^7), and maximum beam load (465 μA) [3].

The measurement of cavity detuning due to external vibration sources and the vibrational modes of the cavity/cryomodule structure is conducted in both the cryomodule test facility and in the tunnel. The results of these measurements tend to be location and environment dependent.

Microphonics testing of the first unit (C100-1) met design goals marginally, but results were higher than expected based on prototype testing. This unexpected result was due at least in part to the low-loss cell shape used for the C100 cavities. The cell walls are more vertical as they approach the iris making them more susceptible to deflection than the original CEBAF cell shape. Even though the detuning due to microphonics was lower than the 12 GeV allowance, a detailed vibration study was initiated and conducted on the first two C100-style cryomodules, the R100 and C100-1. This study led to a simple modification of the pivot plate in the tuner assembly that reduced the amount of detuning in later cryomodules by an average of 42% [157].

Figure 57 depicts the frequency shifts due to microphonics over a 90 s period in cavities with and without the modified tuner and shows how the pivot plate was modified. The cavity with the modified tuner has had an almost 50% reduction in detuning.

In addition to reducing sensitivity to microphonics, modifying the tuner assembly led to an average reduction of 35% (348 Hz/Torr to 228 Hz/Torr) in the cavity pressure sensitivity (detuning due to pressure changes). An average reduction of 25%, in the static Lorentz detuning (from $-2.16\ \mathrm{Hz/(MV/m)^2}$ to $-1.62\ \mathrm{Hz/(MV/m)^2}$) was measured as well.

5. SRF commissioning summary

Commissioning results show that these cryomodules were able to deliver an average energy gain of 113 MeV which exceeds the design goal of 108 MV. The C100 cavities were able to operate at an average maximum operating gradient of 20.1 MV/m. However, during routine beam operations in the Fall of 2022, nine C100 zones averaged only 86 MeV, where most had substantial field emission radiation. Plans for improving the performance of the C100 cavities are discussed in Sec. V D.

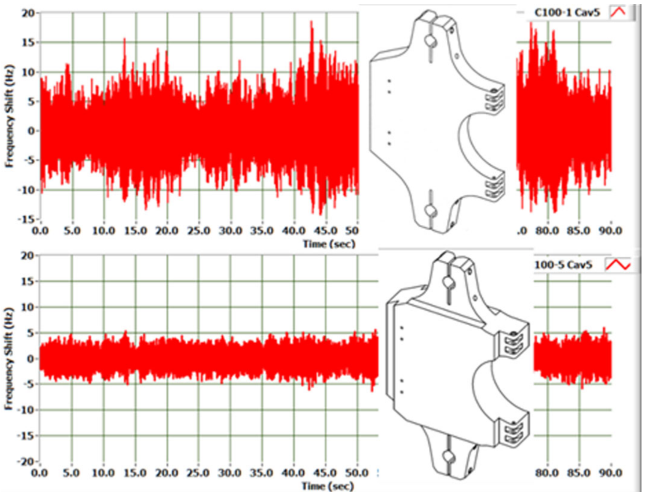

FIG. 57. 90 second microphonic detuning measurement for original and modified pivot plate. Detuning fluctuations are reduced to almost 50% (from [104]).

B. Particulate movement in high-gradient SRF linacs

Particulates that have settled on the inner surface of beamline components other than SRF cavities, such as intercryomodule warm sections, pose no harm. However, when they migrate to the rf surface of an SRF cavity, a number of impactful consequences may result. Particulates that have landed on the cavity iris region may become new field emitters, giving rise to an increased electron field emission at the high required operational cavity gradient. Some secondary effects induced by enhanced field emission such as rapid beamline vacuum excursions, frequent charging of components made of insulation materials, and accelerated boiling of bath liquid helium, have the acute consequence of reducing the linac energy output. Such limits in the collective operational acceleration by the ensemble of installed cavities, even though individual cavities are intrinsically capable of higher gradient as demonstrated in their individual qualification testing, need to be avoided. Other secondary effects such as the field emitted electrons producing gamma and neutron radiations are chronic effects degrading and ultimately damaging accelerator components, in turn negatively impacting the operating schedule and maintenance cost for the accelerator.

Particulate movement is currently understood as a driving mechanism behind the apparent loss of energy reach in CEBAF [158]. Understanding the controlling variables of particulate movement in accelerator-quality

FIG. 58. Identifying particulate sources. Left: collecting particulates from a five-cell cavity previously operated with beam for reconstructing contamination distribution and offline determination of particulate sizes and compositions; right: inspecting the sealing surface of a beamline gate valve Viton seal aided with a magnifying glass for large particulates.

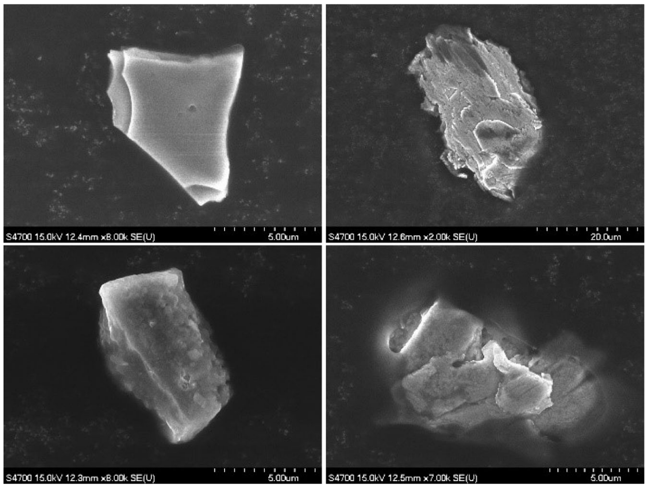

FIG. 59. Examples of particulates of Ti/Ta, stainless-steel, silicate, and copper (clockwise starting at upper left), found on the surface of cavities extracted from beamlines (from Ref. [159]).

vacuum with or without cw electron beams is a prerequisite to solving and perhaps ultimately reversing the slow energy loss problem. Besides, a lasting solution requires the knowledge of the particulate sources and mechanisms of particulate movement in the entire CEBAF linac beamline systems. To that end, a fresh effort was started in 2014 [159–163], coinciding the onset of CEBAF 12 GeV era operation, with a three-pronged strategy: (i) identifying (see Fig. 58) and reducing particulate sources; (ii) identifying the particulate transporting mechanisms and blocking particulate traffic into the cavity space; and (iii) developing effective *in situ* particulate removal apparatus and procedures and applying them at scheduled intervals [164].

As established in Ref. [159], a critical first step taken at the beginning of this campaign against particulates in CEBAF was to collect with a suitable method particulate matter from the vacuum surfaces of components including SRF cavities that had been operated with beam for some time. The collected samples were transferred to carbon tapes which were then analyzed with an SEM for characterization. Typical examples of particulates found on the surface of cavities removed from the cryomodule FEL-2, being refurbished into C50-12, are shown in Fig. 59.

Through systematic collection and characterization of particulates from cavities and beam pipes in the cryomodule FEL-2, physical evidence of particulate movement was revealed [159]. Ti/Ta particulates, a characteristic material of the differential elements in the cryomodule ion pump (so-called B pump in the CEBAF nomenclature) were detected in all four of the sampled cavities, two being close to the B pump (the first two cavities in the string) and the other two being away from the pump (last two cavities in the string). Stainless steel and silicate particulates were observed in abundance. All these observations point to a consistent picture of particulate sources being outside of SRF cavities and particulate loading, by some movement mechanisms, postcryomodule installation. Several changes were implemented in CEBAF SRF linac operation and maintenance practices based on the findings of 2014–2015 particulate collection and identification effort, all targeted at reducing source particulates, including the implementing "cavity-quality cleaning" of adjacent warm girder beamline UHV components of any future cryomodule extracted from the accelerator tunnel for refurbishment. Furthermore, high voltage conditioning of ion pumps (hi-potting) has been prohibited over the entire CEBAF linac system and the B pumps are disabled during any planned cryomodule warm-up. Modern NEG/ion pumps have replaced the current conventional or differential ion pumps in the CEBAF SRF linacs since the summer of 2016 [165]. From 2016 onward, extracted cryomodules and warm girder beamline UHV components are further sampled for particulate characterization with an improved collection method and automated SEM analysis procedure [166,167]. This resulted in a growing catalog of particulates, confirming and reinforcing the extent of particulate contamination, and the need for controlling particulate sources external to SRF cavities.

Recently, particulate source identification efforts moved to evaluate the *in situ* particulate generation of the regular beamline components in their nominal use for beam operation. The current focus is the cryomodule isolation gate vales (two each for every installed cryomodule) and ion pumps (one each for every installed cryomodule and one each for every warm girder between adjacent cryomodules). A laboratory test bed (see Fig. 60) has been established since May 2019. Preliminary test results have established a correlation between service life and particulate generation for both the beamline gate valves and ion pumps. No particulates down to 0.3 μm in size were detected for a freshly in-house rebuilt gate valve with accumulated open/close cycles up to 1000. In comparison, particulates up to 2 μm in size were frequently detected for a gate valve extracted from the CEBAF North Linac. A differential ion pump extracted from the North linac zone

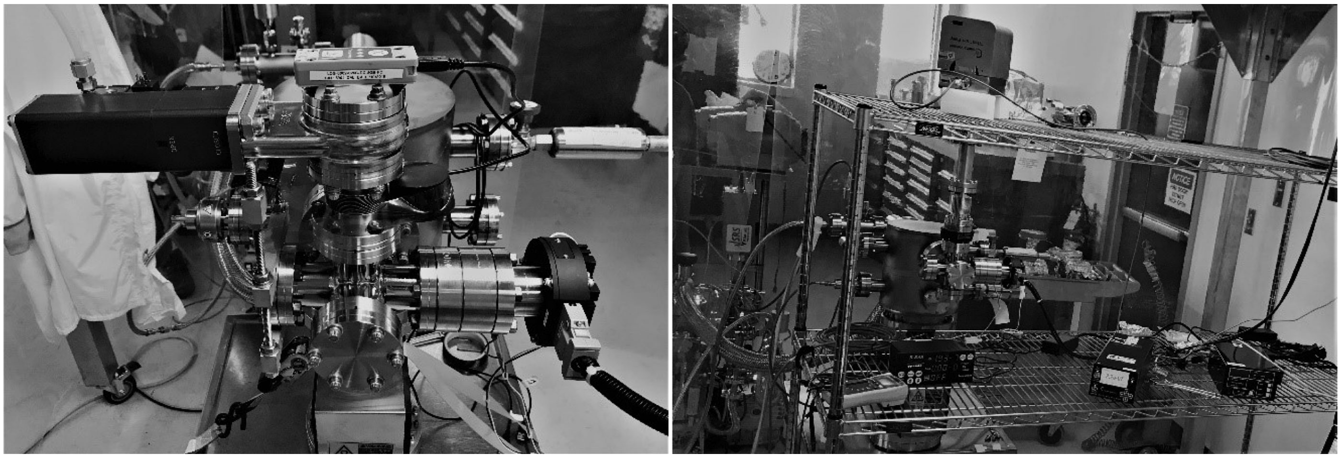

FIG. 60. Laboratory vacuum test bed instrumented with a vacuum particle counter configured for evaluation of particulate generation attributes of CEBAF beamline gate valves (left) and ion pumps (right).

1L23, which was the B pump of a new cryomodule C100-6 installed for the CEBAF 12 GeV upgrade, was tested with a controlled vacuum in the range of 10^{-7} to 10^{-4} torr and varying gas species such as N_2, He, and Ar. No particulate down to the detection limit of the vacuum particle counter was detected regardless of its operating high voltage. In comparison, particulates up to 2 μm in size were easily detected in a conventional ion pump, which was extracted from the former JLAB FEL with standard operating high voltage.

Presently, the gate valve and ion pump evaluation is dedicated to determining the onset of particulate generation as the accumulated service life increases. The outcome of this effort is a set of recommended operational procedures as well as maintenance schedules of the current beamline gate valves and ion pumps for effective control of particulate generation. Furthermore, alternative valves and pumps possessing superior particle generation attributes are to be evaluated as future options for the CEBAF linac SRF systems.

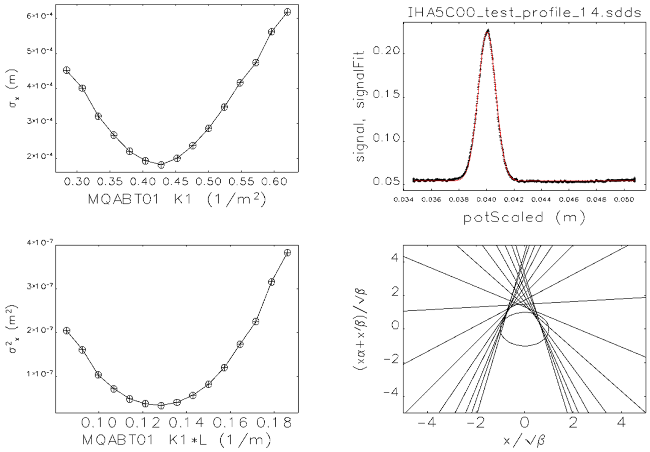

FIG. 61. Emittance measurement example.

Depending on the nature of moving forces, different modes of particulate movement may be identified. In routine CEBAF electron beam operation, the intrinsic electrostatic force levitates, suspends, and transports the charged population of particulates that are exposed to or irradiated by various species including x rays, gamma rays, and electrons. When excessive charge accumulation reaches a point where the internal repulsive Coulomb force exceeds the tensile strength of the body material, particulate explosion or fragmentation results, leading to particulate mobility. In interrupted beam operating conditions, such as fault-triggered gate valve closures, the mechanical shocking force launches particulates originally at rest on a given site. Launched particulates then follow ballistic trajectories governed by gravity and ultimately land at a remote site. In an accident condition when a cavity string vacuum is lost, either partially or completely, the hydrodynamic force arising from gas inrush disperses particulates. The landscape of particulate distribution on the beamline UHV surfaces over the affected linac section might be profoundly changed in a catastrophic vacuum loss event. Last but not least, the thermal force, arising from temperature gradients that exist in the beamline axial direction because of alternating cold and warm components in the CEBAF linacs, acts on suspended particulates, which then tend to drift adiabatically toward the cold cavity walls.

An interesting observation has recently been made due to microscopic SEM inspection of the sealing surfaces of Viton seals from beamline gate valves extracted from the CEBAF North Linac. Earlier optical inspection established that particulates were embedded along these sealing surfaces. Attempts to characterize these particulates using an ordinary SEM, however, failed because of severe charging in the nonconducting Viton elastomer. By using a special SEM at the College of William & Mary, that specimen charging problem was overcome when the specimen was measured in the ambient air. The microscopic images revealed the concentration of particulates captured, with an estimated density of 10^4–10^5 per mm^2 for particulates 10 μm or smaller in size. The elemental composition of these particulates has a large overlap with those collected from the beamline UHV surfaces. This recent observation led us to conclude that we now have the first physical evidence of the existence of charged particulates in the CEBAF beamline spaces. Moreover, in view of the outcome from the test bed gate valve evaluation which shows zero particulate generation from a freshly in-house rebuilt gate valve, we now have a potential future solution to reduce the particulate input into cavities, namely blocking particulate movement using the Viton seal as a particulate trap. Alternative particulate traps, such as electrostatic precipitators, are a potential solution as well. We plan to evaluate these options in conjunction with developing a plan for scheduled maintenance of the CEBAF beamline gate valves.

An important step in understanding particulate movement, but currently missing, is its direct observation. Toward that end, a novel particulate detector was invented and patented at Jefferson Lab. The detector is based on the phase and amplitude interruption of a laser beam interacting with a passing particulate, which is introduced through a window into the accelerator beamline. The design package was completed in September 2019 and the first demonstration unit has been built in collaboration with OmniSensing Photonics LLC. Extensive bench testing is ongoing, which is to be followed by a field test in CEBAF. We anticipate that by applying such particulate detectors in the CEBAF SRF linacs, detecting and diagnosing particulate movement in real time will become available, providing needed information to guide solutions for reducing, preserving, and even possibly reversing the problem of slow loss of CEBAF energy reach.

C. Beam delivery

During CEBAF's operational life, many procedures and processes have been developed in order to operate recirculated linacs efficiently. Many of these processes have been improved as a result of the upgrade project. In this section, we highlight individual systems in the accelerator that are important for accurate and timely beam delivery. These tools are all by now sufficiently developed that operations staff routinely utilize them during the initial setup of the accelerator after a long down, to affect a change of CEBAF configuration needed as part of the physics program, or to analyze the existing machine configuration during operations. In particular, we discuss the methods to manage the large number of magnet settings in the accelerator, our optics verification tools, the path length systems, and the linac energy management system.

1. Model driven settings

For the 12 GeV upgrade, improvements in agreement between the CEBAF model and machine performance, along with new software tools and processes, were implemented such that new machine configurations can be set from the model with less tune time. Over the course of 12 GeV CEBAF commissioning, these new tools and processes were tested and improved upon. The result was a measurable reduction in the necessary time for new machine configurations.

A CEBAF Modeling Team was formed to establish tools and procedures for model-driven configuration of 12 GeV. The Modeling Team chose the accelerator simulation code ELEGANT [168] to model the machine. The Modeling Team established a formal feedback process such that model discrepancies discovered during commissioning and operation are fed back to the model, thus providing a path for convergence. The process includes a formal audit to verify consistency and correctness.

To address configuration control, the CEBAF Element Database (`CED`) was created [169,170]. `CED` is a relational database that stores beamline elements and their attributes. It is the authoritative source of hardware, control system, and model information for the accelerator. It is accessed real time by control system software and operator tools. Operator screens are generated on the fly from `CED` so they are always correct and up to date. A number of high-level software tools were developed, based on ELEGANT and `CED`, to provide operators the means to quickly and consistently configure and tune the machine.

For example, elegant Download Tool (eDT) is a high-level software tool that generates magnet design setpoints for various machine energies and pass configurations based on the modeled ELEGANT values stored in `CED` [171]. eDT also compares the present machine set points to the design set points and provides a means to highlight off-design magnets.

2. Beam optics tuning

Emittance measurement and matching. During the 6 GeV era, transverse optics matching was manually performed using designated tuning knobs while observing differential orbits produced by diagnostic kickers [57,172]. The `qsUtility` software toolset was developed to perform transverse emittance measurement and matching for 12 GeV CEBAF in a more deterministic and reproducible fashion [173].

The `qsUtility` software toolset automates the measurement of emittance and Twiss parameters, along with computing quadrupole settings to achieve the design Twiss parameters at each match point.

The emittance is measured by varying the field strength of one or more quadrupole magnets while measuring the beam size with a downstream wire scanner as described in [174]. To save time, the beam size measurements are performed with the "zig-zag" method described in [175]. An example of data collected and analyzed in an emittance measurement is shown in Fig. 61.

The Twiss parameters at the entrance of the quadrupole that were varied during the measurement are determined by solving Eq. (1) for ϵ, β, and α using the least squares method outlined in [174].

$$\begin{pmatrix} (\sigma_x^{(1)})^2 \\ (\sigma_x^{(2)})^2 \\ (\sigma_x^{(3)})^2 \\ \dots \\ (\sigma_x^{(n)})^2 \end{pmatrix} = \begin{pmatrix} (R_{11}^{(1)})^2 & 2R_{11}^{(1)}R_{12}^{(1)} & (R_{11}^{(1)})^2 \\ (R_{11}^{(2)})^2 & 2R_{11}^{(2)}R_{12}^{(2)} & (R_{11}^{(2)})^2 \\ (R_{11}^{(3)})^2 & 2R_{11}^{(3)}R_{12}^{(3)} & (R_{11}^{(3)})^2 \\ \dots & & \\ (R_{11}^{(n)})^2 & 2R_{11}^{(n)}R_{12}^{(n)} & (R_{11}^{(n)})^2 \end{pmatrix} \begin{pmatrix} \beta(s_0)\epsilon \\ -\alpha(s_0)\epsilon \\ \gamma(s_0)\epsilon \end{pmatrix}. \tag{1}$$

The superscript indices in parentheses refer to the measurement step, the $\sigma_x^{(n)}$ are the beam size measurements, and the $R_{11}^{(n)}$ and $R_{12}^{(n)}$ are the transport matrix elements for the beamline from the varied quadrupole and the wire scanner.

Once the upstream Twiss parameters are determined, a set of quadrupole set points to match to the design Twiss parameters at the match point is computed using the built-in optimizer in ELEGANT [168].

Matching is performed at the exit of the injector, at each of the ten spreaders, and at the entrance to each of the four experiment halls. Occasionally, hand tuning in one or more recombiners is needed using the Courant-Snyder measurement, as described in [57,172], to produce optics suitable for matching at the downstream spreaders.

The ray-tracing technique described in [176,177] is being explored for use during machine setup. The technique involves injecting a number of orbits into a region of the accelerator and monitoring the position response to trace out the phase ellipse of the beam as it travels. The ray-trace technique measures the beam optics at multiple locations simultaneously which reduces setup time and provides a more global understanding of the machine optics.

Dispersion measurement and correction. Dispersion measurement at CEBAF is performed by modulating the beam energy and observing the differential beam positions. The differential beam positions are proportional to dispersion [172]. The final four cavities in the Injector Linac and the eight cavities in the 20th cryomodule in the North Linac are used for energy modulation [57], with the North Linac cavities used most commonly. Dispersion correction is performed arc by arc by adjusting designated pairs of quadrupole magnets in each recirculation arc for horizontal dispersion correction and designated pairs in each spreader and recombiner for vertical dispersion correction. Adjustments are performed while observing the downstream differential orbits and adjusting designated quads to cancel the dispersion leakage out of each dispersive region.

A new software tool for displaying dispersion measurements in a more operator-friendly fashion, along with an automatic dispersion optimization method to speed up dispersion corrections, is being explored for future use at CEBAF [178].

3. Beam locks

The CEBAF beam experiences both slow drifts and fast fluctuations in beam position and energy. Slow drifts are due to magnet power supply fluctuations, temperature drifts, ground motion, and the like. Fast fluctuations are primarily induced by power line frequency interference. In order to ensure that the beam stays within the energy and orbit apertures of the machine and within the users' requirements, a set of feedback locks has been developed.

Orbit locks. A set of slow orbit locks was implemented to stabilize the beam against slow orbit drifts at frequencies less than 1 Hz [179,180]. The slow orbit locks maintain beam positions into the injector linac, each of the ten recirculation arcs, each of the five extraction regions, and various locations in each of the experimental hall transport lines. Each lock uses a pair of correctors and BPMs for each plane to maintain the required beam position and angle into the region of interest. The locks are calibrated empirically by applying small kicks with the lock correctors and measuring the resulting BPM positions to produce a response matrix. The orbit lock server uses the control device (CDEV) interface layer [181] to communicate with instances of the orbit lock GUI and the EPICS control system.

Arc energy locks. A set of slow energy locks was also implemented to stabilize the beam against similarly slow energy drifts [182]. The energy locks adjust the gradient set points in selected SRF cavities at or near the end of each linac to maintain the correct beam energy in the downstream arcs. There is a lock to maintain the correct energy from the injector linac through the injector chicane, from the North Linac into arc 1, and from the South Linac into arc 2 (Fig. 62).

The beam energy monitor (BEM) [183] provides the energy input to the arc energy locks. BEM computes the beam energy in each arc using the arc magnet power supply set point, corrector set points, and BPM position readbacks (Fig. 63).

Generic locks. In addition to dedicated slow orbit and energy locks, a so-called generic lock architecture was

FIG. 62. Energy lock GUI.

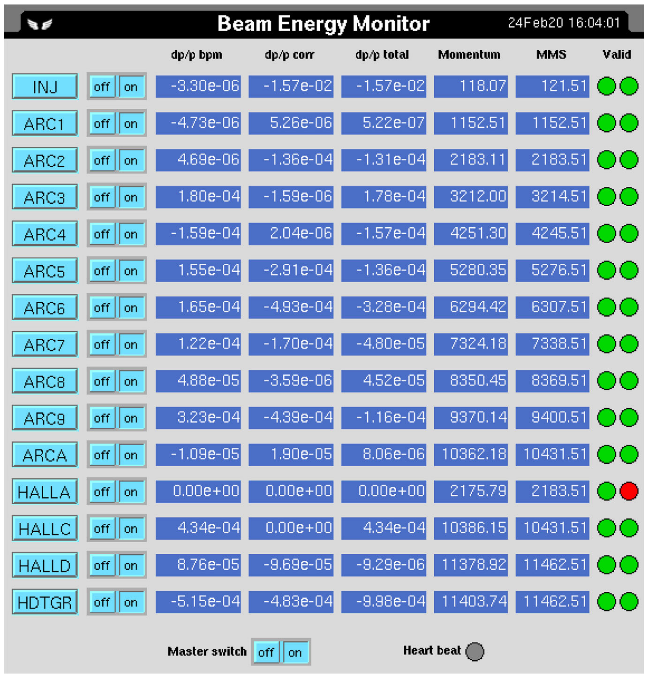
Beam Energy Monitor 24Feb20 16:04:01

		dp/p bpm	dp/p corr	dp/p total	Momentum	MMS	Valid
INJ	off on	-3.30e-06	-1.57e-02	-1.57e-02	118.07	121.51	● ●
ARC1	off on	-4.73e-06	5.26e-06	5.22e-07	1152.51	1152.51	● ●
ARC2	off on	4.69e-06	-1.36e-04	-1.31e-04	2183.11	2183.51	● ●
ARC3	off on	1.80e-04	-1.59e-06	1.78e-04	3212.00	3214.51	● ●
ARC4	off on	-1.59e-04	2.04e-06	-1.57e-04	4251.30	4245.51	● ●
ARC5	off on	1.55e-04	-2.91e-04	-1.36e-04	5280.35	5276.51	● ●
ARC6	off on	1.65e-04	-4.93e-04	-3.28e-04	6294.42	6307.51	● ●
ARC7	off on	1.22e-04	-1.70e-04	-4.80e-05	7324.18	7338.51	● ●
ARC8	off on	4.88e-05	-3.59e-06	4.52e-05	8350.45	8369.51	● ●
ARC9	off on	3.23e-04	-4.39e-04	-1.16e-04	9370.14	9400.51	● ●
ARCA	off on	-1.09e-05	1.90e-05	8.06e-06	10362.18	10431.51	● ●
HALLA	off on	0.00e+00	0.00e+00	0.00e+00	2175.79	2183.51	● ●
HALLC	off on	4.34e-04	0.00e+00	4.34e-04	10386.15	10431.51	● ●
HALLD	off on	8.76e-05	-9.69e-05	-9.29e-06	11378.92	11462.51	● ●
HDTGR	off on	-5.15e-04	-4.83e-04	-9.98e-04	11403.74	11462.51	● ●

Master switch off on

Heart beat ●

FIG. 63. Beam energy monitor.

developed to allow operators to easily implement PID locks between arbitrary process variables [184]. Examples of generic locks include locks to maintain stable beam current, rf phase locks, and short-term experiment-specific orbit locks. The generic lock tool allows the operator to specify input and output process variables, PID gains, expressions to enable or disable the lock based on other process variable values, etc. Figure 64 shows an example of a generic lock to maintain horizontal and vertical beam positions on the active collimator in hall D.

Fast feedback. In addition to slow orbit and energy drifts, the beam experiences fast fluctuations in beam position and energy. These fluctuations primarily occur at harmonics of the power line frequency (60, 120, 180 Hz, etc.) [185]. A fast feedback system was implemented to squelch these fast fluctuations [186–189]. The system was originally installed in halls A and C and was expanded to control the beam delivered to hall D as part of the 12 GeV upgrade [190].

The fast feedback system is connected to a set of BPMs which were modified to provide a high enough frame rate in order to be useful as an operational feedback system [188]. Outputs from the fast feedback system include a set or air-core correctors for position control and an rf vernier for energy control [187]. Figure 65 shows a block diagram of the system. Figure 66 shows the control screen for the hall A fast feedback system.

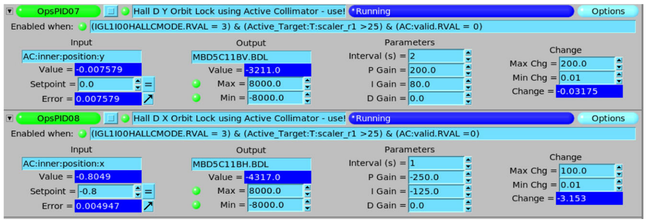

OpsPID07 Hall D Y Orbit Lock using Active Collimator - use! Running

Enabled when: (IGL1I00HALLCMODE.RVAL = 3) & (Active_Target:T:scaler_r1 >25) & (AC:valid.RVAL = 0)

Input: AC:inner:position:y
Value = -0.007579
Setpoint = 0.0
Error = 0.007579

Output: MBD5C11BV.BDL
Value = -3211.0
Max = 8000.0
Min = -8000.0

Parameters:
Interval (s) = 2
P Gain = 200.0
I Gain = 80.0
D Gain = 0.0

Change:
Max Chg = 200.0
Min Chg = 0.01
Change = -0.03175

OpsPID08 Hall D X Orbit Lock using Active Collimator - use! Running

Enabled when: (IGL1I00HALLCMODE.RVAL = 3) & (Active_Target:T:scaler_r1 >25) & (AC:valid.RVAL =0)

Input: AC:inner:position:x
Value = -0.8049
Setpoint = -0.8
Error = 0.004947

Output: MBD5C11BH.BDL
Value = -4317.0
Max = 8000.0
Min = -8000.0

Parameters:
Interval (s) = 1
P Gain = -250.0
I Gain = -125.0
D Gain = 0.0

Change:
Max Chg = 100.0
Min Chg = 0.01
Change = -3.153

FIG. 64. Generic lock example.

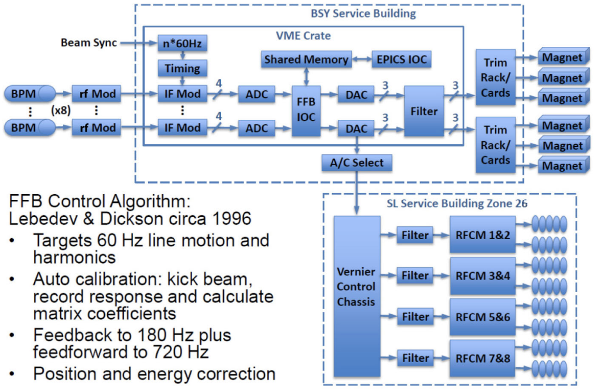

FFB Control Algorithm:
Lebedev & Dickson circa 1996

- Targets 60 Hz line motion and harmonics
- Auto calibration: kick beam, record response and calculate matrix coefficients
- Feedback to 180 Hz plus feedforward to 720 Hz
- Position and energy correction

FIG. 65. Fast feedback block diagram.

The fast feedback system suppresses fluctuations from the first three power line harmonics. A feed forward system was added to suppress higher order harmonics (up to 12). The feed forward system predicts future beam motion by analyzing BPM and corrector data from the recent past [191].

The air-core correctors and rf vernier have a limited dynamic range. A slow lock was added to compensate for slow drifts which could drive the beam outside the range of the air-core correctors and/or the rf vernier [191].

4. Path length and M_{56} measurement and correction

Introduction. Accurate measurements of path length and path length change versus momentum (M_{56}) are critical for maintaining minimum beam energy spread in CEBAF. Path length in CEBAF tends to drift due to seasonal and diurnal temperature changes and long-term ground motion.

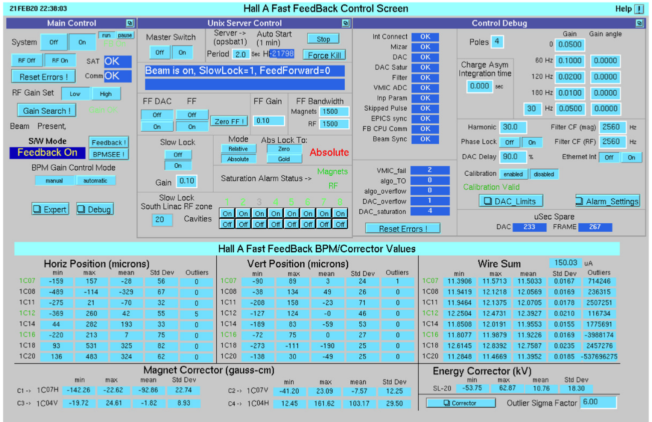
21FEB20 22:38:03 Hall A Fast FeedBack Control Screen

Beam is on, SlowLock=1, FeedForward=0

FIG. 66. Fast feedback control screen.

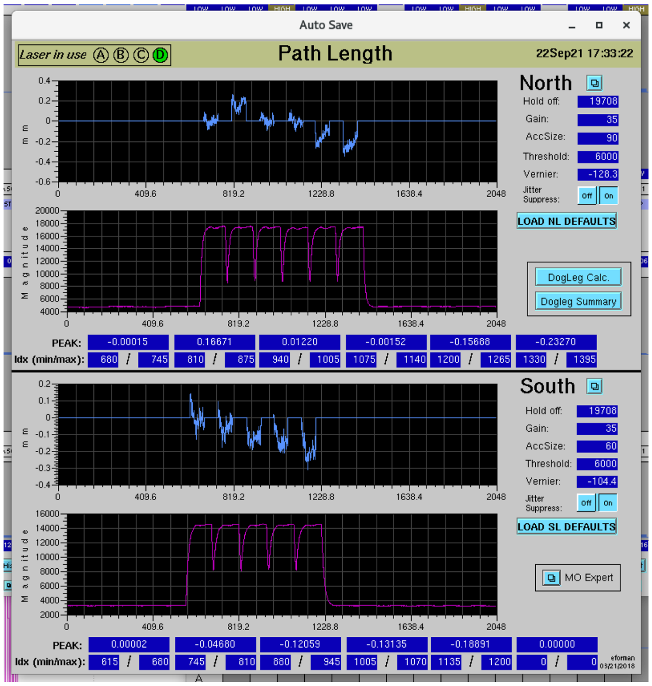

North

Hold off: 19708
Gain: 35
AccSize: 90
Threshold: 6000
Vernier: -128.3
Jitter Suppress: Off On

PEAK: -0.00015 0.16671 0.01220 -0.00152 -0.15688 -0.23270
Idx (min/max): 680 / 745 810 / 875 940 / 1005 1075 / 1140 1200 / 1265 1330 / 1395

South

Hold off: 19708
Gain: 35
AccSize: 60
Threshold: 6000
Vernier: -104.4
Jitter Suppress: Off On

PEAK: 0.00002 -0.04680 -0.12059 -0.13135 -0.18891 0.00000
Idx (min/max): 615 / 680 745 / 810 880 / 945 1005 / 1070 1135 / 1200 0 / 0

FIG. 67. Cavity monitor waveform display.

Overall path length in CEBAF is measured and controlled as it was during 6 GeV running [55,192–194].

Measurement devices. Path length and M_{56} are determined using a precision phase detector [55] measuring the relative arrival time of the electron bunches at a longitudinal pickup cavity operating at 1497 MHz located at the end of each linac. A beam macropulse with a duration of 4 μs (less than the recirculation time of 4.2 μs) is established. The output of the cavity comes out in successive 4 μs bursts separated by 0.2 μs, each burst rf phase locked to the beam current of each pass, respectively. A difference in path length between passes is measured as a phase difference between the rf from each burst [193]. Briefly, the path length is adjusted via the path length chicanes so that all the measured phases are identical. Once this is achieved, higher beam passes transit the linac SRF cavities at the same phase they did on the first pass to high precision.

For 12 GeV CEBAF, functionalities to digitize the waveforms generated by the cavity monitors and to store them as EPICS waveform database records were added. Figure 67 shows a display of the waveforms for each cavity monitor.

The magenta traces are the cavity monitor output amplitude levels for each pass, six for the passes through the North Linac and five for the passes through the South Linac. The output voltages are proportional to beam currents for each pass, therefore they are a useful indication of beam transmission. The blue traces in Fig. 67 represent the relative arrival times of each pass as measured by the rf phase from the cavity monitor. In the example shown, the accumulated path length from pass 1 to pass 2 through the North Linac is 150 μm long, 0 μm for pass 1 to passes 3 and 4, 150 μm too short for pass 1 to pass 5 and 200 μm short for pass 1 to pass 6. In this case, the South Linac is exhibiting a classic pattern often found when the accelerator contracts: 1–2 is 50 μm short, 1–3 is 100 μm short, 1–4 is 150 μm short, and 1–5 is 200 μm short. Because the North Linac data do not reflect this same type of pattern, CEBAF did not actually contract between readings. Rather, the measurement indicates that the South Linac is off crest and requires a phase adjustment.

Path length correction. For path length correction, the main changes in 12 GeV CEBAF are that there are up to six beam passes through the North Linac, and there is no arc 10 path length chicane. The path length correction is now a three-step process. First, the overall accelerator Master Oscillator (MO) frequency is adjusted to globally correct the overall path length, including the arc 10 beam pass. Once this frequency is established, the arc 1–9 path length chicanes can be adjusted to the proper values by the same process used previously. As discussed in Sec. III D 4, at 12 GeV, the dogleg chicanes now allow the path length to be adjusted by up to ±10° of rf phase or ±5.6 mm of path length. As the final step, the path length of the arc 10 pass can be fine-tuned by horizontally steering the beam inboard or outboard in the arc itself using steering correctors, which decreases or increases the distance of the beam travel through the arc. The same method can be used in the other nine arcs in addition to dogleg adjustments to provide a range of several additional millimeters of path length correction.

Dogleg calculator tool. During the 6 GeV era, path length was corrected manually by adjusting dogleg magnets while observing the cavity monitor output traces on a pair of oscilloscopes. For 12 GeV, the cavity monitor outputs are stored as EPICS waveform database records, which allows for automation of path length correction. A new software tool, called `DogCalc12`, was developed to quickly compute and apply new dogleg chicane set points to correct pass-by-pass path length in a single step. The time to correct pass-by-pass path length was reduced from an order of hours to less than 1 m. Figure 68 is a screen capture of the new tool.

`DogCalc12` reads the path length errors from the EPICS waveform data and displays the measured path length errors along with the computed dogleg chicane set points which will correct the errors. The tool will recompute the dogleg set points to accommodate path length corrections using MO frequency adjustments or arc orbit offsets.

M_{56} correction. The path length measurement system is also used to measure M_{56} for each arc. M_{56} is the change in path length for a given momentum change [193]

$$\Delta \text{pathlength} = M_{56} \frac{\Delta p}{p}. \tag{2}$$

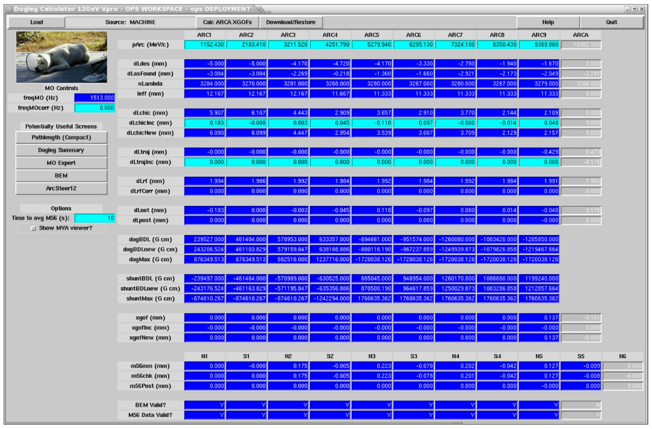

freqMO (Hz) 1513.000
freqMOcorr (Hz) 0.000
Time to avg M56 (s): 10

	ARC1	ARC2	ARC3	ARC4	ARC5	ARC6	ARC7	ARC8	ARC9	ARCA
pArc (MeV/c)	1152.430	2183.410	3211.520	4251.790	5279.940	6295.130	7324.180	8350.430	9369.860	10362.100
dLdes (mm)	-5.000	-5.000	-4.170	-4.720	-4.170	-3.330	-2.780	-1.940	-1.670	0.000
dLasFound (mm)	-3.084	-3.084	-2.269	-0.218	-1.360	-1.660	-2.921	-2.173	-2.049	-2.281
nLambda	3284.000	3270.000	3281.000	3268.000	3280.000	3267.000	3280.000	3267.000	3279.000	3266.000
leff (mm)	12.167	12.167	12.167	11.667	11.333	11.333	11.333	11.333	11.333	0.000
dLchic (mm)	5.907	6.107	4.443	2.909	3.657	2.910	3.770	2.144	2.109	0.000
dLchicInc (mm)	0.183	-0.008	0.003	0.045	-0.118	0.097	-0.060	-0.014	0.048	0.000
dLchicNew (mm)	6.090	6.099	4.447	2.954	3.539	3.007	3.709	2.129	2.157	0.000
dLtraj (mm)	-0.000	-0.000	-0.000	-0.000	-0.000	-0.000	-0.000	-0.000	-0.429	0.473
dLtrajInc (mm)	0.000	0.000	0.000	0.000	0.000	0.000	0.000	0.000	0.000	-0.175
dLrf (mm)	1.994	1.986	1.992	1.984	1.992	1.984	1.992	1.984	1.991	1.983
dLrfCorr (mm)	0.000	0.000	0.000	0.000	0.000	0.000	0.000	0.000	0.000	0.000
dLnet (mm)	-0.183	0.008	-0.003	-0.045	0.118	-0.097	0.060	0.014	-0.048	0.175
dLpost (mm)	0.000	0.000	0.000	0.000	0.000	0.000	0.000	0.000	-0.000	0.000
dogBDL (G cm)	239527.000	461404.000	578953.000	633357.000	-894661.000	-951574.000	-1260080.000	-1083420.000	-1205850.000	
dogBDLnew (G cm)	243206.524	461103.829	579159.847	638188.886	-880116.190	-967237.859	-1249939.873	-1079826.858	-1219467.664	
dogMax (G cm)	876349.513	876349.513	882516.000	1237716.000	-1720038.126	-1720038.126	-1720038.126	-1720038.126	-1720038.126	
shuntBDL (G cm)	-239497.000	-461464.000	-570989.000	-630525.000	885045.000	948954.000	1260170.000	1086880.000	1199240.000	
shuntBDLnew (G cm)	-243176.524	-461163.829	-571195.847	-635356.886	870500.190	964617.859	1250029.873	1083286.858	1212857.664	
shuntMax (G cm)	-874610.267	-874610.267	-874610.267	-1242294.000	1760635.362	1760635.362	1760635.362	1760635.362	1760635.362	
xgof (mm)	0.000	0.000	0.000	0.000	0.000	0.000	0.000	0.000	0.137	-0.151
xgofInc (mm)	-0.000	-0.000	-0.000	-0.000	-0.000	-0.000	-0.000	-0.000	-0.000	0.056
xgofNew (mm)	0.000	0.000	0.000	0.000	0.000	0.000	0.000	0.000	0.137	-0.095

	N1	S1	N2	S2	N3	S3	N4	S4	N5	S5	N6
m56mm (mm)	0.000	-0.000	0.175	-0.005	0.223	-0.078	0.202	-0.042	0.127	-0.009	0.000
m56chk (mm)	0.000	0.000	0.175	-0.005	0.223	-0.078	0.201	-0.042	0.127	-0.008	-0.000
m56Post (mm)	0.000	0.000	0.000	0.000	0.000	0.000	0.000	0.000	-0.000	0.000	0.000
BEM Valid?	Y	Y	Y	Y	Y	Y	Y	Y	Y	N	
M56 Data Valid?	Y	Y	Y	Y	Y	Y	Y	Y	Y	Y	

FIG. 68. Dogleg calculator tool.

M_{56} is measured by applying a small momentum offset and observing the resulting change in path length. Corrections for each arc are performed by adjusting the settings of designated quadrupole magnets according to the design beam optics in the arc.

5. Linac Energy Management

Linac energies are set via a software tool called Linac Energy Management (LEM). Given a requested operating beam energy, LEM distributes the accelerating gradient to individual cavities in a way that minimizes the overall machine rf fault rate [195]. Once the gradient distribution is determined, quadrupoles in the linac are adjusted to the machine model values scaled by the actual beam first pass energy at the quadrupole.

LEM must take into account several aspects of the overall accelerator configuration to complete a setup. Obviously, cavities that are off-line for any reason must be tracked and eliminated from the optimization. In addition, LEM tracks and uses "operations maximum gradient" set points, one for each cavity, determined by the running operations history of that particular cavity. Roughly, the operations maximum gradient is the largest gradient set point, determined by the operations staff through use, that the cavity operates reliably. In no case, should this gradient exceed the maximum gradient as determined in the SRF commissioning outlined in Sec. IV A 1. Included in the LEM optimization is that the operations (and by implication the SRF commissioning) maximum gradient for each cavity is not exceeded. LEM automatically distributes gradient to all operating cavities using a solution that minimizes the rf trip rate but adheres to these constraints [196].

In early 12 GeV CEBAF running, the C100 cavities had to be turned down to approximately 80% of their design value for energy gain due to field emission. Consequently, the old cavities had to be pushed to higher gradients and therefore higher fault rates. The final energy to hall D was lowered from 12.0 to 11.6 GeV to mitigate overall fault rates.

V. FUTURE PLANS

A. Machine learning

Following the lead of other scientific disciplines, such as astronomy and high-energy physics, accelerator physics has started to leverage machine learning to address challenging problems. In the United States, this is largely in response to recent National and Department of Energy (DOE) artificial intelligence (AI) initiatives. We note that despite the terms "machine learning" and "artificial intelligence" often being used interchangeably, machine learning is a subset, albeit a large one, of the more general field of AI. A helpful definition of machine learning is "the field of study that gives computers the ability to learn without being explicitly programmed". This represents a major paradigm shift from conventional programming where the user inputs data and a set of explicit rules is used to generate the output. Machine learning, on the other hand, takes as its input data and the corresponding answers (or labels) and infers the rules. The rules can then be applied to new, unlabeled data. This is an example of supervised machine learning since the data are associated with a label and represent the most common class of machine learning. Unsupervised learning, by contrast, is another category of machine learning that takes unlabeled data as its input and seeks to organize it into clusters or to reduce its dimensionality.

The rise of machine learning—across sectors as diverse as commerce, health care, and science, among others—is being driven by the confluence of computing power, abundant data, open-source software, and theoretical advances in the field. Historically, particle accelerator systems have been a source of enormous amounts of data, not only by users (i.e., experimental beamlines, detectors) but also from machine diagnostics which record data about the beam, hardware components, and their various subsystems. With the advent of specialized coprocessors, such as graphical and tensor processing units and cloud-based computing resources, computing power is available to analyze, process, interact, and visualize large datasets in ways that were not possible before. The quality of free resources available for learning to build machine learning systems, coupled with the accessibility of open-source software that incorporates the latest algorithmic advances, makes for a low barrier of entry into the field. Where machine learning was once a niche field practiced by subject matter experts and trained machine operators, one can now reproduce state-of-the-art results on a personal computer by following a simple tutorial.

Particle accelerators represent a class of complex scientific instruments that comprised many interacting subsystems. As such, they are a source of potentially rich datasets that cover phenomena across a wide variety of timescales, from slow thermal drifts to fast beam loss faults, and across many subsystems with correlations that may or may not be apparent. Data of this kind are described as "big data," that is, datasets so large or complex that it is not amenable to traditional data processing techniques.

1. SRF fault classification

Recently, machine learning was applied in CEBAF for the classification of SRF cavity faults [197]. As a user facility, the goal at CEBAF is to maximize beam time to the experimental halls. Currently, a significant contributor to machine downtime is beam trips caused by SRF system faults. During FY2018, there were an average of six rf trips per hour with a mean recovery time of 0.5 min per trip. Consequently, over an hour of beam time is lost every day. The amount of data lost in the experimental halls is even greater because during analysis of the data, 30 s of data before the trip and 30 s after recovery are discarded.

The C100 modules, in particular, were responsible for 33% of the downtime due to short trips across all accelerator subsystems. In order to better understand the nature and frequency of these faults, a waveform harvester was implemented in each of the 11 C100 cryomodules. For each C100 cavity fault, the system automatically writes 17 rf signals from each of the 8 cavities in the cryomodule to file. The recorded time-series data allow subject matter experts to analyze the data and determine which of the eight cavities within the cryomodule went unstable first and classify the type of cavity fault. Due to the diligent work of system experts, more than 20,000 labeled examples exist; that is, time-series signals from cavities have corresponding labels indicating the first cavity to trip and the fault type. With the existence of these data, there is a clear motivation to utilize supervised machine learning to automate the process. Real-time—rather than postmortem—identification of the offending cavity and classification of the fault type would give control room operators valuable feedback for corrective action planning. Improving the stability of the rf system naturally translates into higher beam-on-target time. It also provides performance metrics that can be used to improve cavity designs [198].

Initial efforts utilized ensemble machine learning, specifically random forests, to train a model on several hundred labeled cavity faults. The models performed well on test data, achieving accuracy scores over 95% and 96% for identifying the cavity that faulted first and for classifying the type of fault, respectively [199]. Encouraged by these initial results, a prototype software system has been developed to deploy trained machine learning models to run online [200]. Commissioning, testing, and first results were completed in early 2020.

Future effort will be aimed at replacing current machine learning models with their deep learning counterparts [201]. Deep learning is a subfield of machine learning which is based on learning successive layers of increasingly meaningful representations of the data. (The "deep" in deep learning refers to multiple hidden layers in the network architecture). The primary advantage of methods based on learning data representations is that it avoids the computationally costly feature engineering step. Efforts are also being made to understand the relevant cavity fault timescales to see whether preventative measures can be taken to avoid a fault if predicted early enough. Longer-term plans are in place to upgrade all CEBAF cryomodules (not just C100s) with the same digital LLRF system. This would allow data collection not only from the 11 C100 cryomodules, but the remaining 39 cryomodules as well. With more data and information, there is increased potential for improving CEBAF availability.

2. Other applications

Building on the initial success of applying machine learning for SRF fault classification, one goal is to continue to find ways to leverage machine learning to improve beam availability and machine reliability. Several such projects are being developed at CEBAF.

For example, one project is directed to uncovering latent knowledge in a large and complex dataset, specifically in CEBAF's archived data. The archiver represents a potentially rich source of information—particularly given the 25 years of operational data at CEBAF—which is underutilized. The goals are twofold; (i) mining useful information to improve the performance of the machine and (ii) identifying how the archiver and associated control systems need to evolve to keep pace with the rapid growth in machine learning.

Another promising application for machine learning is to guide machine tuning, a process which often relies on brute force methods that can be slow to converge. Our efforts have been patterned on encouraging results demonstrated from several fourth-generation light sources where the machine is tuned via machine learning methods to optimize FEL power [202,203], but now optimizing based on other beam quality metrics important to the end users of CEBAF.

As a final example, remote monitoring using autonomous machines represents a novel intersection of robotics with AI [204,205]. The use of robots in potentially hazardous environments, such as accelerator enclosures, would improve personnel safety at CEBAF and could automate time-consuming tasks.

As accelerators grow in complexity to meet the scientific requirements of users, machine learning will be a necessary tool to help meet those demands.

B. Enhancements for physics

Moving into the future, this section documents plans foreseen to enhance the physics reach of the lab. These plans focus on a new generation of experiments at up to 12 GeV beam energy but rely on enhancements to the present beam parameters or maximize exploiting the present parameters by improving the detector systems used.

1. CLAS12, generation 2

Reaching further into the generalized parton distributions (GPDs), transverse momentum dependent (TMDs) parton distributions, and spin-dependent nuclear distribution functions than what was envisioned with the present CLAS12 detector in hall B requires upgrading it to handle higher particle luminosities, more complex event geometries, and a much higher amount of data. Various task groups are looking into new technologies for these upgrades like detector streaming readout to handle the data volume while being able to efficiently extract events of interest with minimal dead time, gas electron multiplier tracking detectors to be able to handle the higher particle flux of more complex events, transition radiation detectors for particle identification, and others. The luminosity upgrade will greatly benefit from the new technologies that the lab is investing on: AI-supported algorithms for particle tracking, electromagnetic calorimeter clustering, online data reconstruction, and data preservation. A stronger integration with the IT group to exploit resources available on site and off site will provide the necessary computing power for the next generation experiments. The CLAS12 detector has the unique opportunity to test future EIC technologies. Replacing partially or in full the current components, it will be possible to deploy the proposed detectors and test them on-beam in conditions even more demanding than what is expected at the Electron-Ion Collider. The experience gained with the future hall-B experimental program will be extremely useful to efficiently run any new projects (including SOLID and MOLLER) and optimize data collection, physics analysis, and data preservation.

2. MOLLER

The MOLLER experiment (Measurement Of a Lepton Lepton Electroweak Reaction) [41] aims to measure the parity-violating asymmetry A_{PV} in polarized electron-unpolarized electron (Møller) scattering. In the Standard Model of particle physics, A_{PV} is due to the interference between the electromagnetic amplitude, mediated by a photon γ, and the weak neutral current mediated by a Z_0 boson. The experiment aims to measure the predicted value of $A_{PV} \sim 33$ parts per billion (ppb) at the experiment kinematics with a precision of about 2% of that value. With such precision, the measurement would be sensitive to the interference of the photon with new neutral current amplitudes which may exist from as yet undiscovered dynamics beyond the Standard Model. New MeV-scale and multi-TeV-scale vector bosons, electron compositeness, supersymmetry, and doubly charged scalars are some examples of the new physics that could be reached by this experiment.

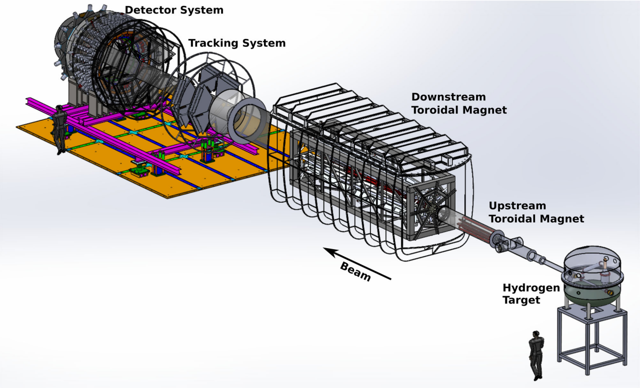

FIG. 69. Conceptual layout of the MOLLER experiment. The apparatus measures approximately 30 m from the center of the hydrogen target to the back of the detector system.

Figure 69 shows the conceptual layout of the MOLLER experiment. Given its length, the experiment is envisioned to take place in hall A, the largest of the existing experimental halls with 53 m inside diameter. The experiment plans to use a polarized electron beam of 11 GeV, the highest beam energy that can be sent to halls A, B, and C, with beam currents of 70 μA. The experiment requires high beam polarizations (> 84%) and high-frequency (~2 kHz) helicity flip to achieve its goals. While the beam energy, current, and polarization requested are standard parameters at JLab, the high-frequency helicity flip is not. The helicity flip frequency affects the amount of noise the detectors see when comparing buckets of electrons with spins opposite to each other. The noise originates from density changes in the 1.25 meters long liquid hydrogen target due to, basically, micron sized bubbles generated by beam heating of the liquid, a total of about 4 kW. For comparison, it is usual for parity-violating experiments to flip the beam helicity at 30 Hz. To achieve a 2 kHz helicity flip rate, new electro-optical materials must be used to rotate the laser polarization and produce polarized electrons from a photocathode. New polarization rotation cells of rubidium titanyle phosphate (RTP) have been implemented to replace the previously used cells of potassium dihydrogen phosphate (KD*P).

Besides the high frequency helicity flip, to be able to measure physics asymmetries of the order of 33 ppb (about 8 times smaller than any other previous JLab parity-violating experiment), many helicity-correlated errors like position, incident angle, beam size, and charge differences between buckets of different helicity must be reduced by a factor of about 4 or better compared with previous experiments, mostly performed during the 6 GeV era.

Such improvements require changes in the injector and its coupling to the first linac as well as a more refined understanding of the 12 GeV machine optics. The MOLLER experiment received Critical Decision-0 (CD0, Mission Need Statement) from the Department of Energy in December 2016 but due to fiscal budget constraints work on it was paused until recently. MOLLER is seeking to receive CD2/3 in 2023.

3. SoLID

A new, large acceptance, high luminosity detector, SoLID (Solenoidal Large Intensity Device) [206] has been proposed to fully exploit the potential of JLab 12 GeV energy upgrade. As the name indicates, the key of this detector is to be able to operate at luminosities much higher than possible in halls B and D which also have large acceptance detectors. The core research program for such a device consists of one parity-violating experiment, three semi-inclusive deep-inelastic experiments, and a J/ψ production experiment. Research programs with polarized targets are also being developed. Figure 70 shows a conceptual layout of the detector. Two configurations are shown.

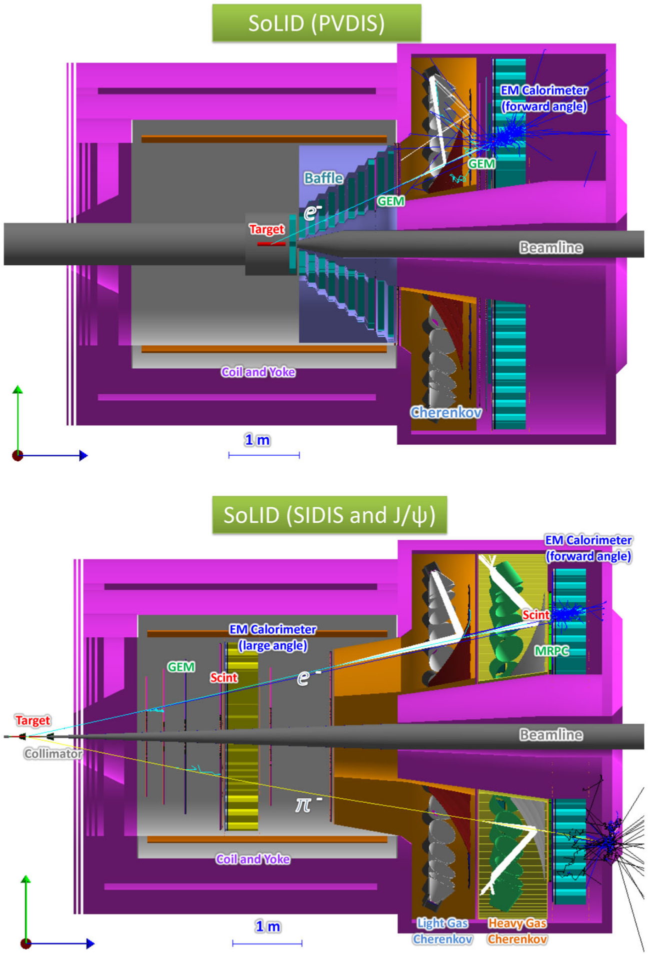

FIG. 70. Conceptual cross-section layout of the SoLID detector. The incident beam moves from left to right. The device has a cylindrical shape with its major axis along the beam. It measures about 8 m along the beam direction and it has a diameter of about 5.6 m. At its core is the CLEO-II superconducting solenoid magnet. The magnet produces a field of up to 1.5 T, has an inner bore of 2.9 m, and a length of about 3.5 m.

The top panel shows the proposed configuration to carry the parity-violating deep-inelastic scattering (PVDIS) experiment while the bottom panel shows the general configuration used for the rest of the program. Note that to be able to reach the design luminosity of 10^{39} cm^{-2} s^{-1} required by the PVDIS experiments, a set of baffles is required to block unwanted photons and hadrons originating in the target. The magnetic field must then be strong enough to spiral the several GeV DIS electrons through the gaps in the baffles and also provide sufficient curvature in the tracks so that their momentum can be reconstructed. Both requirements can be met with a field integral along the flight path on the order of 2.5 T-m.

4. Compact photon source

A compact, high-intensity, multi-GeV photon source (CPS) is being developed to gain access to new lines of research in both halls C and D. The research program in hall C is focused on deep-virtual compton scattering (DVCS), wide-angle compton scattering (WACS), semi-inclusive deep inelastic scattering (SIDIS) meson production, and neutral pion photoproduction with regular and polarized targets. For this research, a neutral particle spectrometer (NPS) is being developed to complement the existing high momentum and super-high momentum spectrometers (HMS and SHMS, respectively) of hall C.

The research program in hall D would use a CPS to produce a beam of neutral kaons [207] directed to the existing GlueX detector system. Basically, this will be a new “facility.” A flux of up to 10^4 K_L/s is expected, about 3 orders of magnitude larger than achieved in the past at other facilities. Such large fluxes will allow one to perform measurements of both differential cross sections and self-analyzing polarizations of the Λ, Σ, Ξ, and Ω hyperons produced. The data are expected to cement the orbitally excited states in the Ξ and Ω spectra as well as aid to constraint the partial wave analysis. It is also expected to have a large impact on our understanding of the strange meson sector.

C. Injector improvements

The present CEBAF injector [21] has a long history of reliability but there are improvements that can be made to support the 12 GeV physics program. In particular, the quarter cryomodule used to accelerate the beam from 500 keV to 5 MeV introduces unwanted x/y coupling as a result of the asymmetrical designs of the rf power couplers for early CEBAF cavities. This x/y coupling makes it difficult to match the beam envelope across the quarter cryomodule [45] which in turn makes it difficult to obtain the maximum desired adiabatic damping required for parity-violation experiments that have demanding helicity-correlated beam requirements [41].

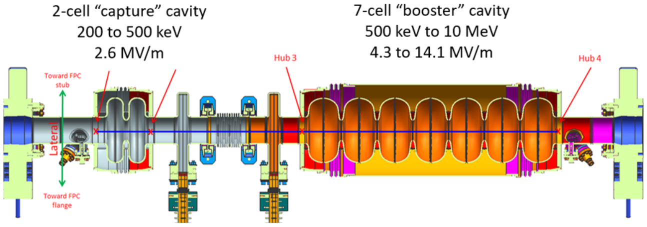

FIG. 71. Schematic diagram of new booster layout.

A new "booster" cryomodule [208,209] was constructed and has been tested in a stand-alone injector test facility for performance testing. The booster cryomodule is composed of two SRF cavities: a two-cell "capture" cavity to accelerate 200 keV beam from the photogun to 1.2 MeV total energy and a seven-cell cavity to accelerate the 1.2 MeV beam to 10 MeV, as shown schematically in Fig. 71. The booster cryomodule eliminates the only copper accelerating structure used at CEBAF, and it is expected, the x/y coupling problematic of the earlier quarter cryomodule. We anticipate the booster cryomodule will improve beam quality for parity-violation experiments and simplify injector setup because there will be fewer rf components required to accelerate beams to relativistic energy and because the photogun will be operating at a 200 kV bias voltage, providing stiffer and more manageable beam. A photograph of the two accelerating cavities on a beamline before they were incorporated into the quarter cryomodule is given in Fig. 72.

The new booster cryomodule was installed at CEBAF in the summer of 2023. The plan is to increase the photogun bias voltage to 200 kV, instead of 130 kV used to present [210]. Modifying the photogun electrostatic design [211] is required. Similarly, the electrostatic features of the Wein filters [212] that are part of the 4π spin manipulator [18] must be modified to maintain capability of 90° spin rotation for 200 keV beam.

Another worthwhile improvement that supports the 12 GeV CEBAF physics program relates to the injector rf "chopper" system [213] originally used to create the required rf time structure on dc beam produced from a thermionic gun that has since been removed from the accelerator. Although the photogun provides rf time structure directly, the chopper system is still used to remove nanoampere level dc beam produced by low-level dc light from the drive lasers [214].

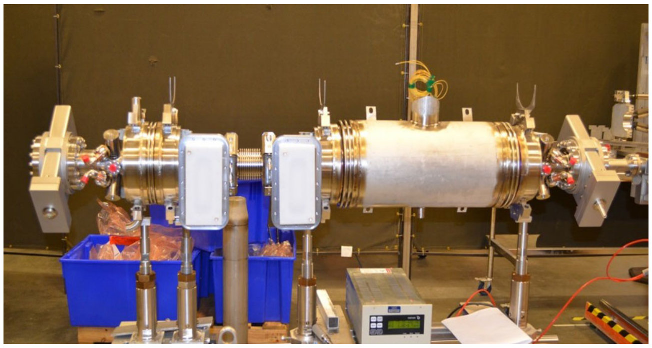

FIG. 72. Booster beamline before enclosing it into a quarter cryomodule.

The present rf chopper system operates at the third subharmonic of the CEBAF accelerating frequency to support beam delivery to three experiment halls. The 12 GeV CEBAF provides beams to four experiment halls [23] and this means two halls must operate at 249.5 MHz with interleaved beams passing through the same chopper slit. An improved 12 GeV chopper system would provide independent chopper slits for each experiment hall. For example, a chopper system operating at the sixth subharmonic of 249.5 MHz could provide independent beams to six experiment halls [215].

D. CEBAF performance plan

CEBAF has been run at the full 12 GeV project specification with pulsed electron beams not suitable for nuclear physics experiments. When cw beam is required, as for the experiments, CEBAF is unable to deliver the full 12 GeV beam to hall D. For example, during the Spring 2022 physics running period, the beam energy in hall D was 11.6 GeV. Effectively executing the 12 GeV experimental program is crucial in maintaining CEBAF as the world leader in experimental nuclear physics.

The CEBAF Performance Plan (CPP) is an internal technical document [216] authored as a performance improvement strategy for CEBAF systems published soon after regular physics running began. This document presents a plan for addressing the known performance gaps as soon as possible and addressing obsolete systems. The plan places a priority on addressing the performance gaps up front so that the majority of the 12 GeV program can benefit from reliable CEBAF operations at design beam parameters.

Gap analysis was performed on several aspects of CEBAF operations [137]. Gaps are identified with respect to CEBAF operational goals outlined within the technical note. There are three subsections: CEBAF availability, energy reach, and operations performance. An outlined performance plan found in subsequent sections of the document map actions to close the performance gaps for realizing the stated goals. Frequent critical system failures, CEBAF energy degradation, and reduced weeks of operations driven by funding issues highlight a few of the topics sought to be addressed by the CEBAF performance plan. The gap in CEBAF energy reach is not insurmountable nor large enough to warrant a halt in 12 GeV operations, but it has been significant enough to place the effective execution of the 12 GeV experimental program at risk. The plans presented in the CPP are meant to mitigate this risk [137,216].

In 2018, funding was allocated to support parts of the CPP. A "CEBAF Reliability Plan FY18-21" was submitted to the Department of Energy from Jefferson Lab leadership aimed at improving CEBAF reliability [217]. The subcategories funded include critical spare parts for accelerator and cryogenic systems, an rf klystron purchase agreement to address end-of-life components, immediate investments in higher risk obsolete systems, energy reach efforts to counter continued LINAC gradient degradation, and projects aimed at optimizing maintenance practices. Significant progress has been made in implementing the CPP strategy within the aforementioned categories, though early in the strategy implementation to fully realize true reliability improvement. An internal technical note, "CEBAF Performance Plan Implementation Summary" JLAB-TN-20-012, highlights specific success and challenges in executing the CPP strategy through 2020 [218].

To address energy reach, and to build operating margin into the beam acceleration systems to the point that 12 GeV running is supported even with the loss of one full C100 cryomodule, a long-term plan has been developed involving several elements: (i) upgrading individual old-style C20 modules so that they can run at gradients approaching 75 MeV, (ii) systematically refurbishing worst-performing C100 modules, and (iii) understanding through performance analysis studies and measurements observed decay of superconducting cavity maximum field. Over the next 5 years, seven "C75" cryomodule replacement/upgrades [219] and five C100 cryomodule refurbishments will be completed. As these tasks are performed, the best recent understanding of cavity processing will be incorporated into any newly installed cryomodules [218]. Figure 73 provides summary estimates of accelerator availability and energy reach over the next half decade.

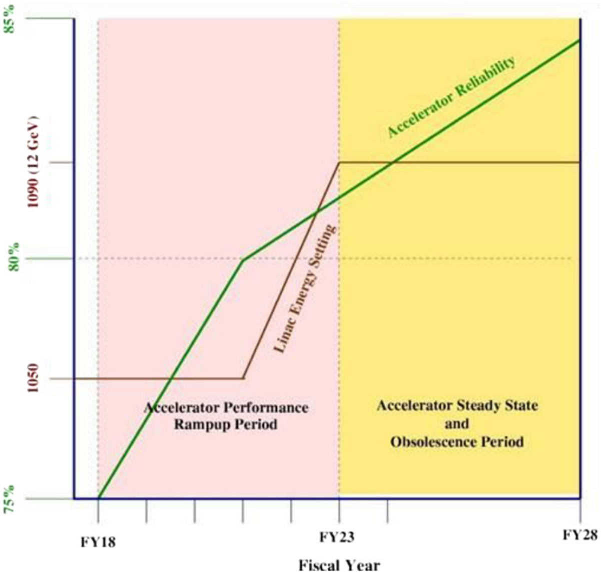

FIG. 73. Future reliability and energy reach predictions from executing the CEBAF performance plan (from [137]).

VI. SUMMARY

Jefferson Lab's CEBAF accelerator has been upgraded and operated at 12 GeV beam energy. This achievement was made possible by continuous improvement in the performance capabilities in niobium superconducting cavities that have arisen in the 25 years since the first CEBAF was completed. Individual "C100" cryomodules of length 10.4 m capable of providing over 100 MeV cw beam energy gain were designed and built. The *Renascence* cryomodule was the first SRF accelerator cryomodule to accelerate cw electron beam by 100 MeV. In addition to the upgrades of the linac, significant upgrades to other accelerator systems needed to be made: the recirculating arc magnets now operate at double the field previously, the cooling capacity of the main helium liquefier has been doubled, the upper beam energy of the injector has been enhanced, and the site electrification and cooling have been upgraded to allow beam operations at elevated energies. In addition, as part of the upgrade project, a new experimental hall D devoted to "QCD spectroscopy" was added to CEBAF and the beam preparation systems and extraction systems have been modified so that all experimental halls at CEBAF can operate with beam simultaneously. Experiments at 12 GeV have led to a greater and deeper understanding of the atomic nucleus and its constituents, and the strong force that holds it together [220].

ACKNOWLEDGMENTS

This material is based upon work supported by the U.S. Department of Energy, Office of Science, Office of Nuclear Physics under Contract No. DE-AC05-06OR23177. As is typical for review papers of this type, authors, who may have worked at one time at Jefferson Lab on some aspect of the 12 GeV project may no longer be working there. In the affiliation list for this paper, the present or final institutional association of the author is listed.

APPENDIX: EXPERIMENTAL HALL BEAM PERFORMANCE REQUIREMENTS

A document was compiled summarizing the beam delivery performance requirements for each of the CEBAF experimental halls and shared with individual hall physics users to assist them in preparing proposals for beam time [221]. For reference purposes, the individual tables are added to this paper. Table XVIII summarizes the beam parameters at hall A, Table XIX the beam parameters in hall B, Table XX the beam parameters for hall C, and Table XXI the beam parameters at the new hall D. Except for the caveat mentioned in Sec. V D regarding beam energy, these tables document the beam quality achieved and routinely delivered to experiment users in the 12 GeV CEBAF era.

TABLE XVIII. Delivery beam parameter table for hall A.

Beam property	Nominal value/range	Stability over 8 h
Spot size at target (rms) (μm)	horizontal <[a] 250, vertical <200	horizontal 20, vertical 20
Angular divergence at target (μrad)	<20	<2
Beam current (μA)	1–120	10% of nominal
Charge per beam bunch (fC)	4–480	10% of nominal
Bunch repetition rate (MHz)	249.5	
Beam position	All locations within 2.5 mm of target center	<40 μm with slow lock and 20 μm at 60 Hz
Relative energy spread (rms)	pass 1 $<10^{-4}$, pass 2 $<10^{-4}$, pass 3 $<10^{-4}$, pass 4 $<3 \times 10^{-4}$, pass 5 $<5 \times 10^{-4}$	10% of nominal
Beam direction (μrad)	±300	<2
Energy range (GeV)	1–11	
Energy accuracy (rms)	3×10^{-3}	
Beam polarization	Up to 85%	
Charge asymmetry	<0.1%	
Background beam halo	<0.1%	
Beam availability (including rf trips)	60%	

[a] Interpret “<” as “not to exceed.”

TABLE XIX. Delivery beam parameter table for hall B.

Beam property	Nominal value/range	Stability over 8 h
Spot size at wire scanner (rms) (μm)	<[a] 100 for 1–6 GeV, <200 for 7–11 GeV	User defined measurement frequency
Angular divergence at target (μrad)	<100	<2
Beam current (nA)	1–160	<5% when > 5 nA
Charge per beam bunch (fC)	$4 \times 10^{-3} - 0.64$	<5% when > 5 nA
Bunch repetition rate (MHz)	249.5	
Beam position	All locations within 2 mm of beam axis	<40 μm with slow lock and 20 μm at 60 Hz
Relative energy spread (rms)	pass 1 $<10^{-4}$, pass 2 $<10^{-4}$, pass 3 $<10^{-4}$, pass 4 $<3 \times 10^{-4}$, pass 5 $<5 \times 10^{-4}$	10% of nominal
Beam direction [μrad]	±300	<2
Energy range [GeV]	1–11	
Energy accuracy (rms)	3×10^{-3}	
Beam polarization	Up to 85%	
Charge asymmetry	<0.1%	
Background beam halo	<0.1%	
Beam availability (including rf trips)	60%	

[a] Interpret “<” as “not to exceed.”

TABLE XX. Delivery beam parameter table for hall C.

Beam property	Nominal value/range	Stability over 8 h
Spot size at target (rms) (μm)	horizontal $<^a$ 250, vertical <200	horizontal 20, vertical 20
Angular divergence at target (μrad)	<20	<2
Beam current (μA)	1–120	10% of nominal
Charge per beam bunch (fC)	4–480	10% of nominal
Bunch repetition rate (MHz)	249.5	
Beam position	all locations within 2.5 mm of target center	<40 μm with slow lock and 20 μm at 60 Hz
Relative energy spread (rms)	pass 1 $<10^{-4}$, pass 2 $<10^{-4}$, pass 3 $<10^{-4}$, pass 4 $<3\times10^{-4}$, pass 5 $<5\times10^{-4}$	10% of nominal
Beam direction (μrad)	±300	<2
Energy range (GeV)	1–11	
Energy accuracy (rms)	3×10^{-3}	
Beam polarization	Up to 85%	
Charge asymmetry	$<0.1\%$	
Background beam halo	$<0.1\%$	
Beam availability (including rf trips)	60%	

[a] Interpret "<" as "not to exceed."

TABLE XXI. Delivery beam parameter table for hall D.

Beam property	Nominal value/range	Stability over 8 h
Spot size at target (rms) (μm)	horizontal $<^a$ 1000, vertical <500	horizontal 100, vertical 100
Angular divergence at target (μrad)	<15	<1
Beam current (nA)	1–2000	10% of nominal
Charge per beam bunch (fC)	$4\times10^{-3}-8$	10% of nominal
Bunch repetition rate (MHz)	249.5	
Beam position	±1 mm	<40 μm
Relative energy spread (rms)	2–3×10^{-3}	10% of nominal
Beam direction (μrad)	±30	<2
Energy range (GeV)	8.8–12.1	
Energy accuracy (rms)	3×10^{-3}	
Background beam halo	$<0.1\%$	
Beam availability (including rf trips)	60%	

[a] Interpret "<" as "not to exceed."

[1] C. W. Leemann, D. R. Douglas, and G. A. Krafft, The Continuous Electron Beam Accelerator Facility: CEBAF at the Jefferson Laboratory, Annu. Rev. Nucl. Part. Sci. **51**, 413 (2001).

[2] Jefferson Lab Information Resources, Unique science opportunities of the 12 GeV upgrade (2020), https://www.jlab.org/physics/GeV/unique.

[3] P. Kneisel, J. Amato, J. Kirchgessner, K. Nakajima, H. Padamsee, H. L. Phillips, C. Reece, R. Sundelin, and M. Tigner, Performance of superconducting storage ring cavities at 1500 MHz, IEEE Trans. Magn. **21**, 1000 (1985).

[4] H. A. Grunder, J. J. Bisognano, W. I. Diamond, B. K. Hartline, C. W. Leemann, J. Mougey, R. M. Sundelin, and R. C. York, The Continuous Electron Beam Accelerator Facility, in *Proceedings of the 1987 Particle Accelerator Conference* (IEEE, Washington, DC, 1987), pp. 13–18, http://accelconf.web.cern.ch/p87/PDF/PAC1987_0013.PDF.

[5] R. C. York and D. R. Douglas, Optics of the CEBAF CW superconducting accelerator, in *Proceedings of the 1987 Particle Accelerator Conference* (IEEE, Washington, DC, 1987), pp. 1292–1294, http://accelconf.web.cern.ch/p87/PDF/PAC1987_1292.PDF.

[6] D. R. Douglas, R. C. York, and J. Kewisch, Optical design of the CEBAF beam transport system, in *Proceedings of the 1989 Particle Accelerator Conference, Chicago, IL* (IEEE, New York, 1989), pp. 557–559, http://accelconf.web.cern.ch/p89/PDF/PAC1989_0557.PDF.

[7] D. Douglas, Optics of beam recirculation in the CEBAF CW linac, in *Proceedings of the 13th International Linear Accelerator Conference, Stanford, CA* (JACoW, Geneva,

Switzerland, 1986), pp. 449–451, https://accelconf.web.cern.ch/l86/papers/th3-8.pdf.

[8] M. Poelker, High power gain-switched diode laser master oscillator and amplifier, Appl. Phys. Lett. **67**, 2762 (1995).

[9] C. Hovater and M. Poelker, Injection modelocked Ti-sapphire laser with discretely variable pulse repetition rates to 1.56 GHz, Nucl. Instrum. Methods Phys. Res., Sect. A **418**, 280 (1998).

[10] C. Leemann and C. G. Yao, A highly effective deflecting structure, in *Proceedings of the Linear Accelerator Conference 1990, Albuquerque, NM* (JACoW, Geneva, Switzerland, 1990), pp. 232–234, http://accelconf.web.cern.ch/l90/papers/mo465.pdf.

[11] M. A. Wilson, R. I. Cutler, E. R. Lindstrom, S. Penner, N. R. Yoder, R. L. Ayres, D. L. Mohr, L. M. Young, and E. R. Martin, NBS-LANL RTM injector installation, in *Proceedings of the 1983 Particle Accelerator Conference, Santa Fe, NM* (IEEE, Piscataway, NJ, 1983), pp. 3021–3023, http://accelconf.web.cern.ch/p83/PDF/PAC1983_3021.PDF.

[12] W. Diamond, The injector for the CEBAF CW superconducting linac, in *Proceedings of the 1987 Particle Accelerator Conference* (IEEE, Washington, DC, 1987), pp. 1907–1909, http://accelconf.web.cern.ch/p87/PDF/PAC1987_1907.PDF.

[13] W. Diamond and R. Pico, Status of the CEBAF injector, in *Proceedings of the 1988 Linear Accelerator Conference, Williamsburg, VA* (JACoW, Geneva, Switzerland, 1988), pp. 403–405, http://accelconf.web.cern.ch/l88/papers/we3-37.pdf.

[14] S. Wang, J. Guo, R. Rimmer, and H. Wang, The new design for capture cavity of CEBAF, in *Proceedings of the 5th International Particle Accelerator Conference, IPAC-2014, Dresden, Germany* (EPS-AG, Dresden, 2014), pp. 3955–3957, http://accelconf.web.cern.ch/IPAC2014/papers/thpri080.pdf.

[15] D. Douglas, R. York, and J. Kewisch, Optical design of the CEBAF beam transport system, in *Proceedings of the 1989 Particle Accelerator Conference, Chicago, IL* (IEEE, New York, 1989), pp. 557–559, https://accelconf.web.cern.ch/p89/PDF/PAC1989_0557.PDF.

[16] R. Abbott, S. Benson, M. Crofford, D. Douglas, R. Gonzales, R. Kazimi, D. Kehne, G. Krafft, P. Liger, H. Liu, D. Machie, and C. Sinclair, Design, commissioning and operation of the upgraded CEBAF injector, in *Proceedings of the 17th International Linear Accelerator Conference (LINAC-1994), Tsukuba, Japan, 1994* (KEK, Tsukuba, Japan, 1994), pp. 777–779, http://accelconf.web.cern.ch/l94/papers/th-30.pdf.

[17] M. Crofford, C. Hovater, G. Lahti, C. Piller, and M. Poelker, The RF system for the CEBAF polarized photoinjector, in *Proceedings of the 19th International Linear Accelerators Conference, Chicago, IL, 1998* (NTIS, Springfield, VA, 1998), pp. 552–554, http://accelconf.web.cern.ch/l98/PAPERS/TU4067.PDF.

[18] J. Grames, P. Adderley, J. Benesch, J. Clark, J. Hansknecht, R. Kazimi, D. Machie, M. Poelker, M. Stutzman, R. Suleiman, and Y. Zhang, Two Wien filter spin flipper, in *Proceedings of the 24th Particle Accelerator Conference, PAC-2011, New York* (IEEE, New York, 2011), pp. 862–864, http://accelconf.web.cern.ch/PAC2011/papers/tup025.pdf.

[19] B. N. Dunham, L. S. Cardman, and C. K. Sinclair, Emittance measurements for the Illinois/CEBAF Polarized Electron Source, in *Proceedings of the Particle Accelerator Conference, Dallas, TX, 1995* (IEEE, New York, 1995), pp. 1030–1032, https://accelconf.web.cern.ch/p95/ARTICLES/WPC/WPC17.PDF.

[20] C. K. Sinclair, P. A. Adderley, B. M. Dunham, J. C. Hansknecht, P. Hartmann, M. Poelker, J. S. Price, P. M. Rutt, W. J. Schneider, and M. Steigerwald, Development of a high average current polarized electron source with long cathode operational lifetime, Phys. Rev. ST Accel. Beams **10**, 023501 (2007).

[21] Y. Wang, A. Hofler, and R. Kazimi, Commissioning of the 123 MeV injector for 12 GeV CEBAF, in *Proceedings of the 6th International Particle Accelerator Conference, IPAC-2015, Richmond, VA* (JACoW, Geneva, Switzerland, 2015), pp. 1920–1922, https://accelconf.web.cern.ch/IPAC2015/papers/tupma037.pdf.

[22] F. Marhauser, W. Clemens, M. Drury, D. Forehand, J. Henry, S. Manning, R. Overton, and S. Williams, Results of cavity series fabrication at Jefferson Laboratory for the cryomodule R100, in *Proceedings of the 2nd International Particle Accelerator Conference, IPAC-2011, San Sebastián, Spain* (EPS-AG, Spain, 2011), pp. 340–342, https://accelconf.web.cern.ch/IPAC2011/papers/mopc113.pdf.

[23] R. Kazimi, J. Grames, A. Hofler, Y. Wang, J. Hansknecht, M. Spata, T. Plawski, M. Poelker, and A. Freyberger, Operational results of simultaneous four-beam delivery at Jefferson lab, in *Proceedings of the 10th International Particle Accelerator Conference, IPAC-2019, Melbourne, Australia, 2019* (JACoW, Geneva, Switzerland, 2019), pp. 2454–2457, http://accelconf.web.cern.ch/ipac2019/papers/wepmp053.pdf.

[24] R. Kazimi, Simultaneous four-hall operation for 12 GeV CEBAF, in *Proceedings of the 4th International Particle Accelerator Conference, IPAC-2013, Shanghai, China* (JACoW, CERN, Geneva, Switzerland, 2013), pp. 3502–3504, https://accelconf.web.cern.ch/IPAC2013/papers/thpfi091.pdf.

[25] P. A. Adderley, J. Clark, J. Grames, J. Hansknecht, K. Surles-Law, D. Machie, M. Poelker, M. L. Stutzman, and R. Suleiman, Load-locked dc high voltage GaAs photogun with an inverted-geometry ceramic insulator, Phys. Rev. ST Accel. Beams **13**, 010101 (2010).

[26] W. Liu, M. Poelker, X. Peng, S. Zhang, and M. Stutzman, A comprehensive evaluation of factors that influence the spin polarization of electrons emitted from bulk GaAs photocathodes, J. Appl. Phys. **122**, 035703 (2017).

[27] T. Maruyama, E. L. Garwin, R. Prepost, G. H. Zapalac, J. S. Smith, and J. D. Walker, Observation of strain-enhanced electron-spin polarization in photoemission from InGaAs, Phys. Rev. Lett. **66**, 2376 (1991).

[28] T. Maruyama, D.-A. Luh, A. Brachmann, J. E. Clendenin, E. L. Garwin, S. Harvey, J. Jiang, R. E. Kirby, C. Y. Prescott, R. Prepost, and A. M. Moy, Systematic study of polarized electron emission from strained GaAs/GaAsp

superlattice photocathodes, Appl. Phys. Lett. **85**, 2640 (2004).

[29] W. Liu, Y. Chen, W. Lu, A. Moy, M. Poelker, M. Stutzman, and S. Zhang, Record-level quantum efficiency from a high polarization strained GaAs/GaAsp superlattice photocathode with distributed Bragg reflector, Appl. Phys. Lett. **109**, 252104 (2016).

[30] X. Peng, M. Poelker, M. Stutzman, B. Tang, S. Zhang, and J. Zou, Mie-type GaAs nanopillar array resonators for negative electron affinity photocathodes, Opt. Express **28**, 860 (2020).

[31] X. Peng, Z. Wang, Y. Liu, D. M. Manos, M. Poelker, M. Stutzman, B. Tang, S. Zhang, and J. Zou, Optical-resonance-enhanced photoemission from nanostructured GaAs photocathodes, Phys. Rev. Appl. **12**, 064002 (2019).

[32] J. Grames, Positron beams at CEBAF, in *Proceedings of the 14th International Particle Accelerator Conference, Venice, Italy* (JACoW, Geneva, Switzerland, 2023), pp. 582–586, https://doi.org/10.18429/JACoW-IPAC2023-MOPL152.

[33] J. Grames, P. Adderley, J. Hansknecht, R. Kazimi, M. Poelker, D. Moser, M. Stutzman, R. Suleiman, and S. Zhang, Milliampere beam studies using high polarization photocathodes at the CEBAF photoinjector, in *Proceedings of the XVII International Workshop on Polarized Sources, Targets and Polarimetry, PSTP2017, Kaist, South Korea* (SISSA, Trieste, Italy, 2017), pp. 1–7, https://pos.sissa.it/324/014/pdf.

[34] C. Hernandez-Garcia, D. Bullard, F. Hannon, Y. Wang, and M. Poelker, High voltage performance of a dc photoemission electron gun with centrifugal barrel-polished electrodes, Rev. Sci. Instrum. **88**, 093303 (2017).

[35] W. Liu, S. Zhang, M. Stutzman, and M. Poelker, Effects of ion bombardment on bulk GaAs photocathodes with different surface-cleavage planes, Phys. Rev. Accel. Beams **19**, 103402 (2016).

[36] M. A. A. Mamun, A. A. Elmustafa, M. L. Stutzman, P. A. Adderley, and M. Poelker, Effect of heat treatments and coatings on the outgassing rate of stainless steel chambers, J. Vac. Sci. Technol. A **32**, 021604 (2014).

[37] M. L. Stutzman, P. A. Adderley, M. A. A. Mamun, and M. Poelker, Nonevaporable getter coating chambers for extreme high vacuum, J. Vac. Sci. Technol. A **36**, 031603 (2018).

[38] M. Poelker, J. Grames, J. Hansknecht, R. Kazimi, and J. Musson, Generation of electron bunches at low repetition rates using a beat-frequency technique, Phys. Rev. ST Accel. Beams **10**, 053502 (2007).

[39] D. Armstrong and R. McKeown, Parity-violating electron scattering and the electric and magnetic strange form factors of the nucleon, Annu. Rev. Nucl. Part. Sci. **62**, 337 (2012).

[40] K. D. Paschke, Sources of helicity-correlated electron beam asymmetries, AIP Conf. Proc. **1149**, 853 (2009).

[41] J. Benesch *et al.*, The MOLLER Experiment: An ultra-precise measurement of the weak mixing angle using Möller scattering, arXiv:1411.4088.

[42] D. Engwall, B. Dunham, L. Cardman, D. Heddle, and C. Sinclair, A spin manipulator for electron accelerators, Nucl. Instrum. Methods Phys. Res., Sect. A **324**, 409 (1993).

[43] J. M. Grames *et al.*, Unique electron polarimeter analyzing power comparison and precision spin-based energy measurement, Phys. Rev. ST Accel. Beams **7**, 042802 (2004); **13**, 069901(E) (2010).

[44] J. M. Grames, C. K. Sinclair, M. Poelker, X. Roca-Maza, M. L. Stutzman, R. Suleiman, M. A. Mamun, M. McHugh, D. Moser, J. Hansknecht, B. Moffit, and T. J. Gay, High precision 5 MeV Mott polarimeter, Phys. Rev. C **102**, 015501 (2020).

[45] Y.-C. Chao, Generation and control of high precision beams at lepton accelerators, in *Proceedings of the 22nd Particle Accelerator Conference, PAC-2007, Albuquerque, NM* (IEEE, New York, 2007), pp. 780–784, http://accelconf.web.cern.ch/p07/PAPERS/TUYAB02.PDF.

[46] R. Sundelin, High gradient superconducting cavities for storage rings, IEEE Trans. Nucl. Sci. **32**, 3570 (1985).

[47] C. E. Reece, Continuous wave superconducting radio frequency electron linac for nuclear physics research, Phys. Rev. Accel. Beams **19**, 124801 (2016).

[48] C. Reece, J. Benesch, M. Drury, C. Hovater, J. Mammosser, T. Powers, and J. Preble, Performance experience with the CEBAF SRF cavities, in *Proceedings of the Particle Accelerator Conference, Dallas, TX, 1995* (IEEE, New York, 1995), pp. 1512–1514, https://accelconf.web.cern.ch/p95/ARTICLES/FAE/FAE12.PDF.

[49] C. Leemann, CEBAF design overview and project status, in *Proceedings of the 3rd Workshop on RF Superconductivity, Argonne National Laboratory, IL* (JACoW, Geneva, Switzerland, 1987), pp. 141–162, http://accelconf.web.cern.ch/srf87/papers/srf87a09.pdf.

[50] S. Simrock, RF control system for CEBAF, in *Proceedings of the Particle Accelerator Conference, San Francisco, CA, 1991* (IEEE, New York, 1991), pp. 2515–2519, http://accelconf.web.cern.ch/p91/PDF/PAC1991_2515.PDF.

[51] S. N. Simrock, J. C. Hovater, I. Ashkenazi, G. E. Lahti, K. L. Mahoney, and J. A. Fugitt, Calibration and operation schemes for CEBAF RF control, in *Proceedings of the 1990 Linear Accelerator Conference, Albuquerque, NM* (JACoW, Geneva, Switzerland, 1990), pp. 480–483, https://accelconf.web.cern.ch/l90/papers/tu462.pdf.

[52] C. Reece, Achieving 800 kW CW beam power and continuing energy improvements in CEBAF, in *Proceedings of the 19th International Linear Accelerators Conference, Chicago, IL, 1998* (NTIS, Springfield, VA, 1998), pp. 448–450, http://accelconf.web.cern.ch/l98/PAPERS/TU4025.PDF.

[53] M. A. Drury, E. F. Daly, G. K. Davis, J. Fischer, C. Grenoble, W. Hicks, J. Hogan, L. King, R. Nichols, T. Plawski, J. Preble, T. Rothgeb, and H. Wang, Performance of the first refurbished CEBAF cryomodule, in *Proceedings of the 22nd Particle Accelerator Conference, PAC-2007, Albuquerque, NM* (IEEE, New York, 2007), pp. 2478–2480, http://accelconf.web.cern.ch/p07/PAPERS/WEPMS059.PDF.

[54] M. A. Drury, E. F. Daly, G. K. Davis, J. Fischer, C. Grenoble, J. Hogan, L. King, K. Macha, J. Mammosser, J. Preble, C. Reece, A. Reilly, J. Saunders, and H. Wang, Summary report for the C50 cryomodule project, in *Proceedings of the 24th Particle Accelerator Conference, PAC-2011, New York* (IEEE, New York, 2011), pp. 1044–1046, http://accelconf.web.cern.ch/PAC2011/papers/tup108.pdf.

[55] G. A. Krafft, M. Crofford, D. R. Douglas, S. L. Harwood, R. Kazimi, R. Legg, W. Oren, K. Tremblay, and D. Wang, Measuring and adjusting the path length at CEBAF, in *Proceedings of the Particle Accelerator Conference, Dallas, TX, 1995* (IEEE, New York, 1995), pp. 2429–2431, https://accelconf.web.cern.ch/p95/ARTICLES/WXE/WXE01.PDF.

[56] Y. Chao, M. Crofford, N. Dobeck, D. Douglas, A. Hofler, C. Hovater, G. A. Krafft, R. Legg, J. Perry, E. Price, S. Suhring, M. Tiefenback, and J. van Zeijts, Commissioning and operation experience with the CEBAF recirculation arc beam transport system, in *Proceedings of the 15th Particle Accelerator Conference, PAC-1993, Washington, DC, 1993* (IEEE, New York, 1993), pp. 587–589, https://accelconf.web.cern.ch/p93/PDF/PAC1993_0587.PDF.

[57] V. A. Lebedev, M. Bickley, S. Schaffner, J. van Zeijts, G. A. Krafft, and W. A. Watson(III), Correction of dispersion and the betatron functions in the CEBAF accelerator, Nucl. Instrum. Methods Phys. Res., Sect. A **408**, 373 (1998).

[58] L. Harwood, The JLAB 12 GeV energy upgrade of CEBAF, in *Proceedings of the 25th Particle Accelerator Conference, PAC-2013, Pasadena, CA, 2013* (IEEE, New York, 2013), pp. 36–40, http://accelconf.web.cern.ch/PAC2013/papers/mozaa1.pdf.

[59] L. Harwood, Upgrading CEBAF to 12 GeV, in *Proceedings of the 20th Particle Accelerator Conference, PAC-2003, Portland, OR* (IEEE, New York, 2003), pp. 586–588, https://accelconf.web.cern.ch/p03/PAPERS/ROPA005.PDF.

[60] A.-M. Valente, E. Daly, J. Delayen, M. Drury, C. Hovater, J. Mammosser, L. Phillips, T. Powers, J. Preble, C. Reece, R. A. Rimmer, H. Wang, and C. Thomas-Madec, Production and performance of the first CEBAF upgrade cryomodule intermediate prototype, in *Proceedings of the 11th International Workshop on RF Superconductivity, Travemünder, Germany* (JACoW, Geneva, Switzerland, 2003), pp. 388–391, http://accelconf.web.cern.ch/SRF2003/papers/tup35.pdf.

[61] A.-M. Valente, E. Daly, J. Delayen, M. Drury, R. Hicks, C. Hovater, J. Mammosser, L. Phillips, T. Powers, J. Preble, C. Reece, R. A. Rimmer, H. Wang, and C. Thomas-Madec, Production and performance of the CEBAF upgrade cryomodule intermediate prototypes, in *Proceedings of the 9th European Particle Accelerator Conference, Lucerne, 2004* (EPS-AG, Lucerne, 2004), pp. 1105–1007, http://accelconf.web.cern.ch/e04/PAPERS/TUPKF072.PDF.

[62] J. R. Delayen, Development of an upgrade of the CEBAF acceleration system, in *Proceedings of the 19th International Linear Accelerators Conference, Chicago, IL, 1998* (NTIS, Springfield, VA, 1998), pp. 400–402, https://accelconf.web.cern.ch/l98/PAPERS/TU4006.PDF.

[63] J. R. Delayen, Development of a cryomodule for the CEBAF upgrade, in *Proceedings of the 9th Workshop on RF Superconductivity, Santa Fe, NM* (NTIS, Springfield, VA, 1999), pp. 218–233, https://accelconf.web.cern.ch/SRF99/papers/tup019.pdf.

[64] L. L. Harwood and C. Reece, CEBAF at 12 and 25 GeV, in *Proceedings of the 10th International Workshop on RF Superconductivity, Tsukuba, Japan* (KEK, Tsukuba, Japan, 2001), pp. 332–336, http://accelconf.web.cern.ch/srf01/papers/ta008.pdf.

[65] L. Harwood, Upgrading CEBAF to 12 GeV, in *Proceedings of the 2003 Particle Accelerator Conference, Portland, OR* (IEEE, New York, 2003), pp. 586–588, http://accelconf.web.cern.ch/p03/PAPERS/ROPA005.PDF.

[66] J. R. Delayen, I. E. Campisi, L. R. Doolittle, P. Kneisel, J. Mammosser, and L. Phillips, Superconducting cavity development for the CEBAF upgrade, in *Proceedings of the 18th Particle Accelerator Conference, New York, 1999* (1999), pp. 937–939, http://accelconf.web.cern.ch/p99/PAPERS/MOP117.PDF.

[67] J. R. Delayen, L. R. Doolittle, E. Feldl, V. Nguyen, and W. Sachleben, Frequency tuning of the CEBAF upgrade cavities, in *Proceedings of the 1999 Particle Accelerator Conference, New York, NY, USA* (IEEE, New York, 1999), pp. 928–930, http://accelconf.web.cern.ch/p99/PAPERS/MOP114.PDF.

[68] G. K. Davis, J. R. Delayen, M. Drury, and E. Feldl, Development and testing of a prototype tuner for the CEBAF upgrade cryomodule, in *Proceedings of the 19th Particle Accelerator Conference, Chicago, IL, 2001* (IEEE, Piscataway, NJ, 2001), pp. 1149–1151, http://accelconf.web.cern.ch/p01/PAPERS/MPPH156.PDF.

[69] E. Daly, G. K. Davis, and W. R. Hicks, Testing of the new tuner design for the CEBAF 12 GeV upgrade SRF cavities, in *Proceedings of the 21st Particle Accelerator Conference, Knoxville, TN, 2005* (IEEE, Piscataway, NJ, 2005), pp. 3910–3912, http://accelconf.web.cern.ch/p05/PAPERS/TPPT073.PDF.

[70] J. R. Delayen, L. Doolittle, T. Hiatt, J. Hogan, J. Mammosser, L. Phillips, J. Preble, W. Schneider, and G. Wu, An R.F. input coupler system for the CEBAF energy upgrade cryomodule, in *Proceedings of the 21st Particle Accelerator Conference, Knoxville, TN, 2005* (IEEE, Piscataway, NJ, 2005), pp. 1462–1464, http://accelconf.web.cern.ch/p99/PAPERS/TUA164.PDF.

[71] G. Wu, H. Wang, C. Reece, and R. Rimmer, Waveguide coupler kick to beam bunch and current dependency on SRF cavities, in *Proceedings of the 13th International Workshop on RF Superconductivity, Peking University, Beijing, China* (JACoW, Geneva, Switzerland, 2007), pp. 721–723, http://accelconf.web.cern.ch/srf2007/PAPERS/WEP85.pdf.

[72] C. Reece *et al.*, Design and construction of the prototype cryomodule renascence for the CEBAF 12 GeV upgrade, in *Proceedings of the 11th International Workshop on RF*

Superconductivity, Travemünder, Germany (JACoW, Geneva, Switzerland, 2003), pp. 131–134, http://accelconf.web.cern.ch/SRF2003/papers/mop38.pdf.

[73] E. Daly, I. E. Campisi, J. Henry, W. R. Hicks, J. Hogan, P. Kneisel, D. Machie, C. E. Reece, T. Rothgeb, J. Sekutowicz, K. Smith, T. Whitlatch, K. M. Wilson, and M. Wiseman, Improved prototype cryomodule for the CEBAF 12 GeV upgrade, in *Proceedings of the 20th Particle Accelerator Conference, PAC-2003, Portland, OR* (IEEE, New York, 2003), pp. 1377–1379, http://accelconf.web.cern.ch/p03/PAPERS/TPAB077.PDF.

[74] J. Sekutowicz, G. Ciovati, P. Kneisel, G. Wu, A. Brinkmann, W. Hartung, R. Parodi, and S. Zheng, Cavities for JLAB's 12 GeV Upgrade, in *Proceedings of the 20th Particle Accelerator Conference, PAC-2003, Portland, OR* (IEEE, New York, 2003), pp. 1395–1397, http://accelconf.web.cern.ch/p03/PAPERS/TPAB085.PDF.

[75] C. Reece, E. Daly, S. Manning, R. Manus, S. Morgan, J. Ozelis, and L. Turlington, Fabrication and testing of the SRF cavities for the CEBAF 12 GeV upgrade prototype cryomodule renascence, in *Proceedings of the 21st Particle Accelerator Conference, Knoxville, TN, 2005* (IEEE, Piscataway, NJ, 2005), pp. 4081–4083, http://accelconf.web.cern.ch/p05/PAPERS/TPPT081.PDF.

[76] C. Reece and H. Tian, Exploiting new electrochemical understanding of niobium electropolishing for improved performance of SRF cavities for CEBAF, in *Proceedings of the 25th International Linear Accelerator Conference, LINAC-2010, Tsukuba, Japan* (KEK, Tsukuba, Japan, 2010), pp. 779–781, http://accelconf.web.cern.ch/LINAC2010/papers/thp010.pdf.

[77] G. Wu, H. Wang, R. Rimmer, and C. Reece, Electromagnetic simulations of coaxial type HOM coupler, in *Proceedings of the 12th International Workshop on RF Superconductivity, Ithaca, NY* (2005), pp. 600–603, http://accelconf.web.cern.ch/SRF2005/papers/thp58.pdf.

[78] C. Reece, E. F. Daly, T. Elliott, H. L. Phillips, J. P. Ozelis, T. Rothgeb, K. Wilson, and G. Wu, High thermal conductivity cryogenic RF feedthroughs for higher order mode couplers, in *Proceedings of the 21st Particle Accelerator Conference, Knoxville, TN, 2005* (IEEE, Piscataway, NJ, 2005), pp. 4108–4110, http://accelconf.web.cern.ch/p05/PAPERS/TPPT082.PDF.

[79] G. Wu and H. Phillips, Cryogenic vacuum RF feedthrough device, U.S. Patent No. 7471052 B2. 2008 (2009).

[80] K. Smith, Radial wedge flange clamp, U.S. Patent No. 6499774 (2002).

[81] T. Moore and C. Reece, Serpentine metal gasket, U.S. Patent 7540502 B1 (2009).

[82] Kazimi, A. P. Freyberger, C. Hovater, G. A. Krafft, F. Marhauser, T. E. Plawski, C. E. Reece, J. Sekutowicz, C. Tennant, M. G. Tiefenback, and H. Wang, Observation and mitigation of multipass BBU in CEBAF, in *Proceedings of the 11th European Particle Accelerator Conference, Genoa, Italy, 2008* (EPSAG, Geneva, 2008), pp. 2722–2724, http://accelconf.web.cern.ch/e08/papers/wepp087.pdf.

[83] Y. Chao, M. Drury, C. Hovater, A. Hutton, G. Krafft, M. Poelker, C. Reece, and M. Tiefenback, CEBAF accelerator achievements, J. Phys. Conf. Ser. **299**, 012015 (2011).

[84] F. Marhauser, J. Henry, and H. Wang, Critical dipole modes in JLAB upgrade cavities, in *Proceedings of the 25th International Linear Accelerator Conference, LINAC-2010, Tsukuba, Japan* (KEK, Tsukuba, Japan, 2010), pp. 776–778, http://accelconf.web.cern.ch/LINAC2010/papers/thp009.pdf.

[85] C. Potratz, H.-W. Glock, U. van, and F. Marhauser, Automatic pole and Q-value extraction for RF structures, in *Proceedings of the 2nd International Particle Accelerator Conference, IPAC-2011, San Sebastián, Spain* (EPS-AG, Spain, 2011), pp. 2241–2243, https://accelconf.web.cern.ch/ipac2011/papers/wepc098.pdf.

[86] C. Reece, E. Daly, J. Henry, W. Hicks, J. Preble, H. Wang, and G. Wu, Optimization of the SRF cavity design for the CEBAF 12 GeV upgrade, in *Proceedings of the 13th International Workshop on RF Superconductivity, Peking University, Beijing, China* (JACoW, Geneva, Switzerland, 2007), pp. 536–539, http://accelconf.web.cern.ch/srf2007/PAPERS/WEP31.pdf.

[87] J. Preble, CEBAF energy upgrade program including rework of CEBAF cavities, in *Proceedings of the 13th International Workshop on RF Superconductivity, Peking University, Beijing, China* (JACoW, Geneva, Switzerland, 2007), pp. 756–760,http://accelconf.web.cern.ch/srf2007/PAPERS/FR104.pdf.

[88] F. Marhauser, A. Burrill, K. Davis, D. Forehand, C. Grenoble, J. Hogan, R. Overton, A. Reilly, R. Rimmer, and M. Stirbet, Fabrication and testing status of CEBAF 12 GeV upgrade cavities, in *Proceedings of the 2nd International Particle Accelerator Conference, IPAC-2011, San Sebastián, Spain* (EPS-AG, Spain, 2011), pp. 337–339, http://accelconf.web.cern.ch/IPAC2011/papers/mopc112.pdf.

[89] F. Marhauser, JLAB SRF cavity fabrication errors, consequences and lessons learned, in *Proceedings of the 2nd International Particle Accelerator Conference, IPAC-2011, San Sebastián, Spain* (JACoW, Geneva, Switzerland, 2011), pp. 346–348, https://accelconf.web.cern.ch/ipac2011/papers/mopc115.pdf.

[90] F. Marhauser, W. A. Clemens, M. A. Drury, D. Forehand, J. Henry, S. Manning, R. B. Overton, and R. S. Williams, Results of cavity series fabrication at Jefferson Laboratory for the Cryomodule "R100", in *Proceedings of the 2nd International Particle Accelerator Conference, IPAC-2011, San Sebastián, Spain* (JACoW, Geneva, Switzerland, 2011), pp. 340–342, https://accelconf.web.cern.ch/ipac2011/papers/mopc113.pdf.

[91] H. Tian, S. G. Corcoran, C. Reece, and M. Kelley, The mechanism of electropolishing of niobium in hydrofluoric–sulfuric acid electrolyte, J. Electrochem. Soc. **155**, D563 (2008).

[92] H. Tian, M. J. Kelley, and C. Reece, Basic electropolishing process research and development in support of improved reliable performance SRF cavities for the future

accelerators, in *Proceedings of the 23rd Particle Accelerator Conference, Vancouver, Canada, 2009* (IEEE, Piscataway, NJ, 2009), pp. 2135–2137, http://accelconf.web.cern.ch/PAC2009/papers/we5pfp058.pdf.

[93] C. Reece, A. C. Crawford, and R. L. Geng, Improved performance of JLab 7-cell cavities by electropolishing, in *Proceedings of the 23rd Particle Accelerator Conference, Vancouver, Canada, 2009* (IEEE, Piscataway, NJ, 2009), pp. 2126–2128, http://accelconf.web.cern.ch/PAC2009/papers/we5pfp055.pdf.

[94] A. Reilly, T. Bass, A. Burrill, K. Davis, F. Marhauser, C. Reece, and M. Stirbet, Preparation and testing of the SRF cavities for the CEBAF 12 GeV upgrade, in *Proceedings of the 15th International Conference on RF Superconductivity, Chicago, IL* (JACoW, Geneva, Switzerland, 2011), pp. 542–548, http://accelconf.web.cern.ch/SRF2011/papers/tupo061.pdf.

[95] T. Bass, G. K. Davis, C. Grenoble, and M. Stirbet, Standardization of CEBAF 12 GeV upgrade cavity testing, in *Proceedings of the 3rd International Particle Accelerator Conference, New Orleans, LA, 2012* (IEEE, Piscataway, NJ, 2012), pp. 2420–2422, http://accelconf.web.cern.ch/IPAC2012/papers/weppc088.pdf.

[96] A. Burrill, G. K. Davis, F. Marhauser, C. Reece, A. V. Reilly, and M. Stirbet, Production and testing experience with the SRF cavities for the CEBAF 12 GeV upgrade, in *Proceedings of the 2nd International Particle Accelerator Conference, IPAC-2011, San Sebastián, Spain* (EPS-AG, Spain, 2011), pp. 26–28, http://accelconf.web.cern.ch/IPAC2011/papers/mooca01.pdf.

[97] A. Burrill, G. K. Davis, C. Reece, A. Reilly, and M. Stirbet, SRF cavity performance overview for the 12 GeV upgrade, in *Proceedings of the 3rd International Particle Accelerator Conference, New Orleans, LA, 2012* (IEEE, Piscataway, NJ, 2012), pp. 2423–2425, http://accelconf.web.cern.ch/IPAC2012/papers/weppc089.pdf.

[98] C. Hovater, T. L. Allison, R. Bachimanchi, G. E. Lahti, J. Musson, T. Plawski, C. Seaton, and D. J. Seidman, Status of the CEBAF energy upgrade RF control system, in *Proceedings of the 25th International Linear Accelerator Conference, LINAC-2010, Tsukuba, Japan* (KEK, Tsukuba, Japan, 2010), pp. 280–282, http://accelconf.web.cern.ch/LINAC2010/papers/mop095.pdf.

[99] A. J. Kimber and R. M. Nelson, RF power upgrade for CEBAF at Jefferson laboratory, in *Proceedings of the 24th Particle Accelerator Conference, PAC-2011, New York* (IEEE, New York, 2011), pp. 2127–2129, http://accelconf.web.cern.ch/PAC2011/papers/thocs4.pdf.

[100] R. Bachimanchi, T. Allison, E. Daly, M. Drury, C. Hovater, C. Mounts, R. Nelson, and T. Plawski, CEBAF SRF performance during initial 12 GeV commissioning, in *Proceedings of the 6th International Particle Accelerator Conference, IPAC-2015, Richmond, VA, 2015* (JACoW, Geneva, Switzerland, 2015), pp. 3638–3642, https://accelconf.web.cern.ch/IPAC2015/papers/thxb1.pdf.

[101] T. Allison, J. Delayen, C. Hovater, J. Musson, and T. Plawski, A digital self excited loop for accelerating cavity field control, in *Proceedings of the 22nd Particle Accelerator Conference, PAC-2007, Albuquerque, NM* (IEEE, New York, 2007), pp. 2481–2483, https://accelconf.web.cern.ch/p07/PAPERS/WEPMS060.PDF.

[102] T. Allison, J. Delayen, C. Hovater, J. Musson, and T. Plawski, Digital self excited loop, U.S. Patent No. 8130045 B1 (2012).

[103] J. R. Delayen, Phase and amplitude stabilization of superconducting resonators, Ph.D. thesis, California Institute of Technology, 1978, https://thesis.library.caltech.edu/867/.

[104] M. A. Drury, G. K. Davis, J. Hogan, C. Hovater, L. King, F. Marhauser, H. Park, J. Preble, C. Reece, R. Rimmer, H. Wang, and M. Wiseman, CEBAF upgrade: Cryomodule performance and lessons learned, in *Proceedings of 16th International Conference on RF Superconductivity, SRF2013, Paris, France, 2013* (JACoW, Geneva, Switzerland, 2014), pp. 836–843, http://accelconf.web.cern.ch/SRF2013/papers/thiob01.pdf.

[105] L. Doolittle, G. Huang, A. Ratti, C. Serrano, R. Bachimanchi, C. Hovater, S. Babel, B. Hong, D. V. Winkle, B. Chase, E. Cullerton, and P. Varghese, The LCLS-II LLRF system, in *Proceedings of the 6th International Particle Accelerator Conference, IPAC-2015, Richmond, VA, 2015* (JACoW, Geneva, Switzerland, 2015), pp. 1195–1197, 10.18429/JACoW-IPAC2015-MOPWI021.

[106] C. Serrano *et al.*, RF controls for high-Q cavities for the LCLS-II, in *Proceedings of the 9th International Particle Accelerator Conference, IPAC-2018, Vancouver, BC, Canada, 2018* (JACoW, Geneva, Switzerland, 2018), pp. 2929–2933, 10.18429/JACoW-IPAC2018-THYGBE3.

[107] C. H. Rode, D. Arenius, W. C. Chronis, D. Kashy, and M. Keesee, 2.0 K CEBAF cryogenics, in *Advances in Cryogenic Engineering: Part A & B*, edited by R. W. Fast (Springer, Boston, MA, 1990), pp. 275–286, 10.1007/978-1-4613-0639-9_34.

[108] D. Arenius, J. Creel, K. Dixon, V. Ganni, P. Knudsen, A. Sidi-Yekhlef, and M. Wright, An overview of the planned Jefferson Lab 12 GeV helium refrigerator upgrade, AIP Conf. Proc. **985**, 588 (2008).

[109] V. Ganni and P. Knudsen, Optimal design and operation of helium refrigeration systems using the Ganni cycle, AIP Conf. Proc. **1218**, 1057 (2010).

[110] V. Ganni, D. M. Arenius, B. S. Bevins, W. C. Chronis, J. D. Creel, and J. D. Wilson, Design, fabrication, commissioning, and testing of a 250 g/s, 2-K helium cold compressor system, AIP Conf. Proc. **613**, 288 (2002).

[111] P. Knudsen, V. Ganni, K. Dixon, R. Norton, and J. Creel, Performance testing of Jefferson Lab 12 GeV helium screw compressors, IOP Conf. Ser. **90**, 012072 (2015).

[112] P. Knudsen and V. Ganni, Simplified helium refrigerator cycle analysis using the 'Carnot step', AIP Conf. Proc. **823**, 1977 (2006).

[113] P. Knudsen, V. Ganni, N. Hasan, K. Dixon, R. Norton, and J. Creel, Modifications to JLab 12 GeV refrigerator and wide range mix mode performance testing results, IOP Conf. Ser. **171**, 012015 (2017).

[114] V. Ganni, P. Knudsen, D. Arenius, and F. Casagrande, Application of JLab 12 GeV helium refrigeration system for the FRIB accelerator at MSU, AIP Conf. Proc. **1573**, 323 (2014).

[115] K. Dixon, V. Ganni, P. Knudsen, and F. Casagrande, FRIB cryogenic plant status, IOP Conf. Ser. **101**, 012071 (2015).

[116] P. Knudsen, V. Ganni, N. Hasan, M. Wright, F. Casagrande, G. Vargas, and N. Joseph, FRIB helium refrigeration system commissioning and performance test results, IOP Conf. Ser. **755**, 012090 (2020).

[117] V. Ravindranath, H. Bai, V. Heloin, E. Fauve, D. Pflueckhahn, T. Peterson, D. Arenius, M. Bevins, C. Scanlon, R. Than, G. Hays, and M. Ross, Process simulations for the LCLS-II cryogenic systems, IOP Conf. Ser. **278**, 012106 (2017).

[118] D. Bullard, L. Harwood, T. Hiatt, J. Karn, E. Martin, W. Oren, C. Rode, K. Sullivan, R. Wines, and M. Wiseman, Modification of the CEBAF transport dipoles for energy upgrade considerations, in *Proceedings of the 18th Particle Accelerator Conference, New York, 1999* (IEEE, New York, 1999), Vol. 5, pp. 3309–3311, 10.1109/PAC.1999.792286.

[119] K. Baggett, L. Harwood, and T. Hiatt, 12 GeV dipole magnet measurement analysis using curved beam trajectories, Jefferson Lab Technical Note No. TN-07-050 (2007), https://jlabdoc.jlab.org/docushare/dsweb/Get/Document-33063/07-050.pdf.

[120] Y. Roblin, Incorporating magnet multipoles in ELEGANT using TOSCA, Jefferson Lab Technical Note No. TN-18-035 (2018), https://jlabdoc.jlab.org/docushare/dsweb/Get/Document-165054/18-035.pdf.

[121] M. Wiseman, T. Hiatt, and L. Harwood, 12 GeV accelerator upgrade, 2007 quadrupole magnet design summary, Jefferson Lab Technical Note No. TN-07-025 (2007), https://jlabdoc.jlab.org/docushare/dsweb/Get/Document-33065/07-025.pdf.

[122] T. Hiatt, K. Baggett, L. Harwood, J. Meyers, and M. Wiseman, Fabrication and measurement of 12 GeV prototype quadrupoles, Jefferson Lab Technical Note No. TN-08-055 (2008), https://jlabdoc.jlab.org/docushare/dsweb/Get/Document-33121/08-055.pdf.

[123] M. Tiefenback, Path length control status at 6 GeV and options for 12 GeV, Jefferson Lab Technical Note No. TN-10-020 (2010), https://jlabdoc.jlab.org/docushare/dsweb/Get/Document-68981/10-020.pdf.

[124] M. Tiefenback, A further analysis of the September 2010 CEBAF thermal expansion test, Jefferson Lab Technical Note No. TN-13-004 (2013), https://jlabdoc.jlab.org/docushare/dsweb/Get/Document-68857/13-004.pdf.

[125] S. Adhikari *et al.*, The gluex beamline and detector, Nucl. Instrum. Methods Phys. Res., Sect. A **987**, 164807 (2021).

[126] M. McCaughan, J. Benesch, Y. Roblin, and T. Satogata, First e-/photon commissioning results for the GlueX experiment/hall D at CEBAF, in *Proceedings of the 6th International Particle Accelerator Conference, IPAC-2015, Richmond, VA, 2015* (JACoW, Geneva, Switzerland, 2015), pp. 1916–1919, 10.18429/JACoW-IPAC2015-TUPMA036.

[127] J. Benesch, Hall D preliminary optics design, Jefferson Lab Technical Note No. TN-00-011 (2000), https://jlabdoc.jlab.org/docushare/dsweb/Get/Document-32227/00-011.pdf.

[128] J. Benesch, Hall D optics design, Jefferson Lab Technical Note No. TN-01-041 (2001), https://jlabdoc.jlab.org/docushare/dsweb/Get/Document-32317/01-041.pdf.

[129] J. Benesch, Hall D optics design, Jefferson Lab Technical Note No. TN-03-027 (2003), https://jlabdoc.jlab.org/docushare/dsweb/Get/Document-32544/03-027.pdf.

[130] T. Allison *et al.*, The Qweak experimental apparatus, Nucl. Instrum. Methods Phys. Res., Sect. A **781**, 105 (2015).

[131] Y. Roblin, Normal and skew multipole terms in the dipoles and quadrupoles of the 12 GeV CEBAF upgrade, Jefferson Lab Technical Note No. TN-08-042 (2008), https://jlabdoc.jlab.org/docushare/dsweb/Get/Document-33130/08-042.pdf.

[132] Y. Chao, Improved optimization of North linac momentum profile for CEBAF 12 GeV upgrade, Jefferson Lab Technical Note No. TN-05-004 (2005), https://jlabdoc.jlab.org/docushare/dsweb/Get/Document-32815/05-004.pdf.

[133] M. Sands, The physics of electron storage rings: An introduction, Report No. SLAC-121, 1970, https://www.osti.gov/servlets/purl/4064201.

[134] S. A. Bogacz, Double bend achromat arc optics for 12 GeV CEBAF, Jefferson Lab Technical Note No. TN-07-010 (2007), https://jlabdoc.jlab.org/docushare/dsweb/Get/Document-33016/07-010.pdf.

[135] S. A. Bogacz *et al.*, Design deck for 12 GeV optics, Jefferson Lab Technical Note No. TN-07-016 (2007), https://jlabdoc.jlab.org/docushare/dsweb/Get/Document-33033/07-016.pdf.

[136] T. Satogata, Y. Roblin, M. Tiefenback, and D. Turner, 12 GeV CEBAF transverse emittance evolution, in *Proceedings of the 6th International Particle Accelerator Conference, IPAC-2015, Richmond, VA, 2015* (JACoW, Geneva, Switzerland, 2015), pp. 640–642, 10.18429/JACoW-IPAC2015-WEBD1.

[137] M. F. Spata, 12 GeV CEBAF initial operational experience and challenges, in *Proceedings of the 9th International Particle Accelerator Conference, IPAC-2018, Vancouver, BC, Canada* (JACoW, Geneva, Switzerland, 2018), pp. 1771–1775, 10.18429/JACoW-IPAC2018-WEYGBD1.

[138] R. Kazimi, J. Fugitt, A. Krycuk, C. K. Sinclair, and L. Turlington, Test of a new RF separator structure for CEBAF, in *Proceedings of 16th International Linear Accelerator Conference, LINAC-1992, Ottawa, Canada* (JACoW, Geneva, Switzerland, 1992), pp. 244–246, https://accelconf.web.cern.ch/l92/papers/mo4-70.pdf.

[139] R. Kazimi, H. Wang, J. Hansknecht, and M. Spata, Source and extraction for simultaneous four-hall beam delivery system at CEBAF, in *Proceedings of the 4th International Particle Accelerator Conference, IPAC-2013, Shanghai, China* (JACoW, CERN, Geneva, Switzerland, 2013), pp. 2896–2898, https://accelconf.web.cern.ch/IPAC2013/papers/wepfi085.pdf.

[140] H. Wang, G. Cheng, L. Turlington, and M. Wissmann, Cavity design, fabrication and test performance of

750 MHz, 4-rod separators for CEBAF 4-hall beam delivery system, in *Proceedings of the 6th International Particle Accelerator Conference, IPAC-2015, Richmond, VA* (JACoW, Geneva, Switzerland, 2015), pp. 3548–3550, 10.18429/JACoW-IPAC2015-WEPWI029.

[141] R. Kazimi, J. M. Grames, A. Hofler, Y. Wang, J. Hansknecht, M. Spata, T. E. Plawski, M. F. Poelker, and A. Freyberger, Operational results of simultaneous four-beam delivery at Jefferson Lab, in *Proceedings of the 10th International Particle Accelerator Conference, IPAC-2019, Melbourne, Australia* (JACoW, Geneva, Switzerland, 2019), pp. 2454–2457, 10.18429/JACoW-IPAC2019-WEPMP053.

[142] J. R. Delayen and S. U. De Silva, Designs of superconducting parallel-bar deflecting cavities as deflecting/crabbing applications, in *Proceedings of the 15th International Conference on RF Superconductivity, Chicago, IL* (JACoW, Geneva, Switzerland, 2011), p. 219, http://accelconf.web.cern.ch/SRF2011/papers/mopo053.pdf.

[143] H. Park, S. U. De Silva, and J. R. Delayen, Characteristics and fabrication of a 499 MHz superconducting deflecting cavity for the Jefferson Lab 12 GeV upgrade, in *Proceedings of the 3rd International Particle Accelerator Conference, New Orleans, LA, 2012* (IEEE, Piscataway, NJ, 2012), p. 2450, https://accelconf.web.cern.ch/IPAC2012/papers/weppc101.pdf.

[144] S. U. De Silva, H. Park, K. E. Deitrick, and J. R. Delayen, Beam dynamics studies of 499 MHz superconducting RF-dipole deflecting cavity system, in *Proceedings of the 6th International Particle Accelerator Conference, IPAC-2015, Richmond, VA* (JACoW, Geneva, Switzerland, 2015), p. 3564, https://accelconf.web.cern.ch/IPAC2015/papers/wepwi035.pdf.

[145] A. S. Hofler, B. A. Bowling, C. S. Higgins, P. K. Kloeppel, G. A. Krafft, and K. L. Mahoney, Performance of the CEBAF arc beam position monitor, in *Proceedings of the 15th Particle Accelerator Conference, PAC-1993, Washington, DC, 1993* (IEEE, New York, 1993), pp. 2298–2300, https://accelconf.web.cern.ch/p93/PDF/PAC1993_2298.PDF.

[146] T. Powers, L. Doolittle, R. Ursic, and J. Wagner, Design, commissioning and operational results of wide dynamic range BPM switched electrode electronics, AIP Conf. Proc. **390**, 257 (1997).

[147] R. Ursic, R. Flood, C. Piller, E. Strong, and L. Turlington, 1 nA beam position monitoring system, in *Proceedings of the Particle Accelerator Conference, Vancouver, BC, Canada, 1997* (IEEE, New York, 1997), pp. 2131–2133, https://accelconf.web.cern.ch/pac97/papers/pdf/9P089.PDF.

[148] H. Feng, Beam profile monitor system (Harp), Jefferson Lab Technical Note No. TN-91-064 (1991), https://jlabdoc.jlab.org/docushare/dsweb/Get/Document-34046/91-064.pdf.

[149] C. Yan, P. Adderley, D. Barker, J. Beaufait, K. Capek, R. Carlini, J. Dahlberg, E. Feldl, K. Jordan, B. Kross, W. Oren, R. Wojcik, and J. VanDyke, Superharp—a wire scanner with absolute position readout for beam energy measurement at CEBAF, Nucl. Instrum. Methods Phys. Res., Sect. A **365**, 261 (1995).

[150] C. Seaton, 12 GeV Harp control chassis system overview document, Jefferson Lab Technical Note No. TN-22-024 (2014), https://jlabdoc.jlab.org/docushare/dsweb/Get/Document-257155/22-024.pdf.

[151] P. Kloeppel, Beam diagnostics at CEBAF, Jefferson Lab Technical Note No. TN-86-039 (1986), https://jlabdoc.jlab.org/docushare/dsweb/Get/Document-33476/86-039.pdf.

[152] P. Kloeppel, Transverse emittance measured by synchrotron light monitor, Jefferson Lab Technical Note No. TN-86-026 (1986), https://jlabdoc.jlab.org/docushare/dsweb/Get/Document-33456/86-026.pdf.

[153] B. Freeman, J. Gubeli, and M. Tiefenback, Multiple synchrotron light monitors for transverse matching and monitoring at CEBAF, in *Proceedings of 8th International Beam Instrumentation Conference, IBIC-2019* (JACoW, Geneva, Switzerland, 2019), pp. 439–443, 10.18429/JACoW-IBIC2019-TUPP044.

[154] Physics design, mechanical layouts, and implementation provided by Michael Tiefenback, Joe Gubeli and Brian Freeman.

[155] J. Yan and K. Mahoney, New beam loss monitor for 12 GeV upgrade, in *Proceedings of ICALEPCS-2009, Kobe, Japan* (JACoW, Geneva, Switzerland, 2009), pp. 582–584, http://accelconf.web.cern.ch/icalepcs2009/papers/wep092.pdf.

[156] K. Mahoney and H. Robertson, Jefferson Lab IEC 61508/61511 Safety PLC based safety system, in *Proceedings of ICALEPCS-2009, Kobe, Japan* (JACoW, Geneva, Switzerland, 2009), pp. 394–396, http://accelconf.web.cern.ch/icalepcs2009/papers/wec002.pdf.

[157] K. Davis, J. Matalevich, T. Powers, and M. Wiseman, Vibration response testing of the CEBAF 12 GeV upgrade, in *Proceedings of the 2012 Linear Accelerator Conference, Tel-Aviv, Isreal* (JACoW, Geneva, Switzerland, 2012), pp. 240–242, http://accelconf.web.cern.ch/LINAC2012/papers/mopb031.pdf.

[158] R. L. Geng, A. Freyberger, and R. A. Rimmer, Understanding and mitigation of field emission in CEBAF SRF linacs, in *Proc. of the 10th International Particle Accelerator Conference, Melbourne, Australia* (2019), pp. 3039–3042, http://accelconf.web.cern.ch/ipac2019/papers/weprb097.pdf.

[159] R. L. Geng, J. F. Fischer, E. A. McEwen, and O. Trofimova, Nature and implication of found actual particulates on the inner surface of cavities in a full-scale cryomodule previously operated with beams, in *Proceedings of 17th International Conference on RF Superconductivity, SRF-2015, Whistler, Canada* (JACoW, Geneva, Switzerland, 2015), pp. 164–168, http://accelconf.web.cern.ch/SRF2015/papers/mopb035.pdf.

[160] A. Freyberger, Summary report from the CEBAF OPS 2015 StayTreat, Jefferson Lab Technical Note No. TN-15-033 (2015), https://jlabdoc.jlab.org/docushare/dsweb/Get/Document-107190/15-033.pdf.

[161] A. Freyberger, R. L. Geng, G. Krafft, T. Michalski, and T. Reilly, Summary of mini-workshop on beamline field emitter particulates in CEBAF SRF linacs, Jefferson Lab

Technical Note No. TN-16-008 (2016), https://jlabdoc.jlab.org/docushare/dsweb/Get/Document-117729/16-008.pdf.

[162] R. L. Geng, G. Krafft, and A. Freyberger, Six Month Follow Up on Action Items of Feb 2016 CEBAF Field Emitter Workshop (2016), Jefferson Lab Technical Note No. TN-16-037, https://jlabdoc.jlab.org/docushare/dsweb/Get/Document-128350/16-037.pdf.

[163] R. L. Geng, Root causes of field emitters in SRF cavities placed in CEBAF tunnel, in *Proceedings of the 7th International Particle Accelerator Conference, IPAC-2016, Busan, Korea* (JACoW, Geneva, Switzerland, 2016), pp. 3198–3201, http://accelconf.web.cern.ch/ipac2016/talks/thobb03_talk.pdf.

[164] M. Drury, F. Humphry, L. King, M. McCaughan, and A. Solopova, Results of the 2015 helium processing of CEBAF cryomodules, in *Proceedings of the 3rd North American Particle Accelerator Conference, NA-PAC-2016, Chicago, IL* (JACoW, Geneva, Switzerland, 2017), pp. 1054–1057, 10.18429/JACoW-NAPAC2016-THA1IO02.

[165] G. Ciovati, R. Geng, Y. Lushtak, P. Manini, E. Maccallini, and M. Stutzman, Operation of a high-gradient superconducting radio-frequency cavity with a non-evaporable getter pump, Nucl. Instrum. Methods Phys. Res., Sect. A **842**, 92 (2017).

[166] J. K. Spradlin, O. Trofimova, C. Reece, and A.-M. Valente-Feliciano, Particulate sampling of cavity and warm beampipe surfaces removed from CEBAF, in *Proceedings of the oPS StayTreat Presentation, 2017* (unpublished).

[167] J. K. Spradlin, A.-M. Valente-Feliciano, O. Trofimova, and C. Reece, Analysis of particulates sampled from C100-6, 2019 (unpublished).

[168] M. Borland, elegant: A flexible SDDS-compliant code for accelerator simulation, Advanced Photon Source Report No. LS-287, 2000.

[169] T. L. Larrieu, M. Joyce, M. Keesee, C. Slominski, R. Slominski, and D. Turner, The CEBAF element database and related operational software, in *Proceedings of the 6th International Particle Accelerator Conference, IPAC-2015, Richmond, VA* (JACoW, Geneva, Switzerland, 2015), pp. 1256–1258, 10.18429/JACoW-IPAC2015-MOPWI045.

[170] T. Larrieu, M. Joyce, and C. Slominski, The CEBAF Element Database, in *Proceedings of the 24th Particle Accelerator Conference, PAC-2011, New York* (IEEE, New York, 2011), pp. 594–596, http://accelconf.web.cern.ch/PAC2011/papers/mop261.pdf.

[171] D. Turner, eDT and model-based configuration of 12 GeV CEBAF, in *Proceedings 6th International Particle Accelerator Conference (IPAC'15), Richmond, VA, USA, May 3-8, 2015*, International Particle Accelerator Conference No. 6 (JACoW, Geneva, Switzerland, 2015), pp. 1259–1261, 10.18429/JACoW-IPAC2015-MOPWI046.

[172] V. A. Lebedev, M. Bickley, J. Bisognano, S. Schaffner, J. van Zeijts, G. A. Krafft, W. A. Watson, and B. Yunn, Linear optics correction in the CEBAF accelerator, in *Proceedings of the APS Meeting Abstracts*, APS Meeting Abstracts (1997), https://ui.adsabs.harvard.edu/abs/1997APS..PAC..8W35L.

[173] D. Turner, Software tools for emittance measurement and matching for 12 GeV CEBAF, in *Proceedings of the 7th International Particle Accelerator Conference, IPAC-2016, Busan, Korea, 2016* (JACoW, Geneva, Switzerland, 2016), pp. 2792–2795, 10.18429/JACoW-IPAC2016-WEPOR053.

[174] M. G. Minty and F. Zimmermann, *Measurement and Control of Charged Particle Beams* (Springer, Berlin, 2012).

[175] M. McCaughan, M. Tiefenback, and D. Turner, Improvements to existing Jefferson Lab wire scanners, in *Proceedings of 4th International Particle Accelerator Conference, Shanghai, China* (JACoW, Geneva, Switzerland, 2013), pp. 855–857, https://accelconf.web.cern.ch/IPAC2013/papers/mopwa076.pdf.

[176] R. M. Bodenstein, M. G. Tiefenback, and Y. R. Roblin, Real beam line optics from a synthetic beam, in *Proceedings of 1st International Particle Accelerator Conference, Kyoto, Japan* (JACoW, Geneva, Switzerland, 2010), pp. 4629–4631, https://accelconf.web.cern.ch/IPAC10/papers/thpe050.pdf.

[177] R. M. Bodenstein, Y. R. Roblin, and M. G. Tiefenback, Further analysis of real beam line optics from a synthetic beam, in *Proceedings of 3rd International Particle Accelerator Conference, New Orleans, LA* (JACoW, Geneva, Switzerland, 2012), pp. 1269–1271, https://accelconf.web.cern.ch/IPAC2012/papers/tuppc046.pdf.

[178] D. Turner, New methods for dispersion measurement and correction for 12 GeV CEBAF, in *Proceedings of the 9th International Particle Accelerator Conference, IPAC-2018, Vancouver, BC, Canada* (JACoW, Geneva, Switzerland, 2018), pp. 4882–4884, 10.18429/JACoW-IPAC2018-THPML094.

[179] J. Zeijts, S. Witherspoon, and W. Watson, Design and implementation of a slow orbit control package at Thomas Jefferson National Accelerator Facility, in *Proceedings of the Particle Accelerator Conference, Vancouver, BC, Canada, 1997* (IEEE, New York, 1997), Vol. 2, pp. 2386–2388, https://accelconf.web.cern.ch/pac97/papers/pdf/6P064.PDF.

[180] A. Hofler, D. Bryan, L. Harwood, M. Joyce, and V. Lebedev, Empirically determined response matrices for on-line orbit and energy correction at Thomas Jefferson National Accelerator Facility, in *Proceedings of the 19th Particle Accelerator Conference, Chicago, IL, 2001* (IEEE, Piscataway, NJ, 2001), pp. 1273–1275, https://accelconf.web.cern.ch/p01/PAPERS/TPAH019.PDF.

[181] CDEV home page (2000), http://www.jlab.org/cdev.

[182] C. Slominski, Energy Locks User's Guide, Jefferson Lab internal document (2020), https://jlabdoc.jlab.org/docushare/dsweb/Get/Document-272875/23-035.pdf.

[183] C. Slominski, BEM User's Guide, Jefferson Lab internal document, https://jlabdoc.jlab.org/docushare/dsweb/Get/Document-272876/23-036.pdf (2022).

[184] B. Bevins and A. Hofler, A distributed feedback system for rapid stabilization of arbitrary process variables, in *Proceedings of the 8th International Conference on Accelerator and Large Experimental Physics Control*

Systems, ICALEPCS-2001, San Jose, CA (JACoW, Geneva, Switzerland, 2001), pp. 259–262, https://accelconf.web.cern.ch/ica01/papers/WECT004.pdf.

[185] M. Tiefenback and R. Li, Survey and analysis of line-frequency interference in the CEBAF accelerator, in *Proceedings of the 16th Particle Accelerator Conference and International Conference on High-Energy Accelerators, HEACC 1995: Dallas, TX* (IEEE, Piscataway, NJ, 1995), pp. 1870–1872, https://accelconf.web.cern.ch/p95/ARTICLES/WAQ/WAQ12.PDF.

[186] M. Chowdhary, G. Krafft, H. Shoaee, S. Simrock, and W. Watson, A prototype fast feedback system for energy lock at CEBAF, in *Proceedings, 16th Particle Accelerator Conference and International Conference on High-Energy Accelerators, HEACC 1995: Dallas, TX* (IEEE, Piscataway, NJ, 1995), pp. 2417–2419, https://accelconf.web.cern.ch/p95/ARTICLES/RAE/RAE11.PDF.

[187] J. Karn, M. Chowdhary, A. Hutton, V. Lebedev, R. Legg, P. Letta, H. Shoaee, W. Watson, and J. van Zeijts, Development of digital feedback systems for beam position and energy at the Thomas Jefferson National Accelerator Facility, in *Proceedings of the Particle Accelerator Conference, Vancouver, BC, Canada, 1997* (IEEE, New York, 1997), pp. 2383–2385, https://accelconf.web.cern.ch/pac97/papers/pdf/6P063.PDF.

[188] R. Dickson and V. Lebedev, Fast feedback system for energy and beam stabilization, in *Proceedings of the 7th International Conference on Accelerator and Large Experimental Physics Control Systems, ICALEPCS-1999, Trieste, Italy* (JACoW, Geneva, Switzerland, 1999), pp. 245–247, https://accelconf.web.cern.ch/ica99/papers/ta1o03.pdf.

[189] M. Chowdhary, G. A. Krafft, H. Shoaee, S. N. Simrock, and W. A. Watson, A prototype fast feedback system for energy lock at CEBAF, in *Proceedings of the 16th Particle Accelerator Conference and International Conference on High-Energy Accelerators, HEACC 1995: Dallas, TX* (IEEE, Piscataway, NJ, 1996), pp. 2417–2419, https://accelconf.web.cern.ch/p95/ARTICLES/RAE/RAE11.PDF.

[190] Y. Roblin, Performance and configuration of the hall D fast-feedback system, Jefferson Lab Technical Note No. TN-09-022, https://jlabdoc.jlab.org/docushare/dsweb/Get/Document-33304/09-022.pdf (2009),

[191] S. Higgins, Fast feedback system help, Jefferson Lab internal document (2018), https://jlabdoc.jlab.org/docushare/dsweb/Get/Document-272877/23-037.pdf.

[192] G. Krafft, B. Bowling, M. Crofford, and J. Hovater, Phase transfer measurements at the Jefferson Lab recirculated linacs, Nucl. Instrum. Methods Phys. Res., Sect. A **557**, 314 (2006).

[193] D. Hardy, J. Tang, R. Legg, M. Tiefenback, M. Crofford, and G. A. Krafft, Automated path length and M56 measurements at Jefferson Lab, in *Proceedings of the Particle Accelerator Conference, Vancouver, BC, Canada, 1997* (IEEE, New York, 1997), pp. 2265–2267, https://accelconf.web.cern.ch/pac97/papers/pdf/8P070.PDF.

[194] M. Tiefenback, On-line measurement and tuning of multi-pass recirculation time in the CEBAF linacs, in *Proceedings of the 19th Particle Accelerator Conference, Chicago, IL, 2001* (IEEE, Piscataway, NJ, 2001), pp. 553–555, https://accelconf.web.cern.ch/p01/PAPERS/ROAB012.PDF.

[195] J. R. Delayen, L. R. Doolittle, and C. E. Reece, Operational Optimization of Large-scale SRF Accelerators, in *Proceedings of the 18th Particle Accelerator Conference, New York, 1999* (IEEE, New York, 1999), pp. 940–942, http://accelconf.web.cern.ch/p99/PAPERS/MOP118.PDF.

[196] J. Benesch, A longitudinal study of field emission in CEBAF's SRF cavities 1995–2015, arXiv:1502.06877.

[197] C. Tennant, A. Carpenter, T. Powers, A. Shabalina Solopova, L. Vidyaratne, and K. Iftekharuddin, Superconducting radio-frequency cavity fault classification using machine learning at Jefferson Laboratory, Phys. Rev. Accel. Beams **23**, 114601 (2020).

[198] T. Powers and A. Solopova, CEBAF C100 fault classification based on time domain RF signals, in *Proceedings of the 19th International Conference of RF Superconductivity, Dresden, Germany* (JACoW, Geneva, Switzerland, 2019), pp. 763–769, https://accelconf.web.cern.ch/srf2019/papers/weteb3.pdf.

[199] A. Solopova, A. Carpenter, T. Powers, Y. Roblin, C. Tennant, L. Vidyaratne, and K. Iftekharuddin, SRF cavity fault classification using machine learning at CEBAF, in *Proceedings of the 10th International Particle Accelerator Conference, Melbourne, Australia* (JACoW, Geneva, Switzerland, 2019), pp. 1167–1170, http://accelconf.web.cern.ch/IPAC2019/papers/TUXXPLM2.pdf.

[200] A. Carpenter, T. Powers, Y. Roblin, A. Solopova, C. Tennant, L. Vidyaratne, and K. Iftekharuddin, Initial implementation of a machine learning system for SRF cavity fault classification at CEBAF, in *Proceedings of the 17th Biennial International Conference on Accelerator and Large Experimental Physics Control Systems, ICALEPCS-2019, New York, NY* (JACoW, Geneva, Switzerland, 2019), pp. 1131–1135, https://accelconf.web.cern.ch/icalepcs2019/papers/wepha025.pdf.

[201] L. Vidyaratne, A. Carpenter, T. Powers, C. Tennant, K. M. Iftekharuddin, M. M. Rahman, and A. S. Shabalina, Deep learning based superconducting radio-frequency cavity fault classification at Jefferson laboratory, Front. Artif. Intell. **4**, 718950 (2022).

[202] J. Duris, D. Kennedy, A. Hanuka, J. Shtalenkova, A. Edelen, P. Baxevanis, A. Egger, T. Cope, M. McIntire, S. Ermon, and D. Ratner, Bayesian optimization of a free-electron laser, Phys. Rev. Lett. **124**, 124801 (2020).

[203] J. Kirschner, A. Adelmann, N. Hiller, R. Ischebeck, A. Krause, M. Mutný, and M. Nonnenmacher, Bayesian optimisation for fast and safe parameter tuning of SwissFEL, in *Proceedings of the 39th Free Electron Laser Conference, FEL-2019*, (JACoW, Geneva, Switzerland, 2019), pp. 707–710, 10.18429/JACoW-FEL2019-THP061; see also arXiv:2203.13968.

[204] R. Michaud, Mobile diagnostic—Drone use in accelerator enclosures (2018), Jefferson Lab internal report https://jlabdoc.jlab.org/docushare/dsweb/Get/Document-272874/23-034.pdf.

[205] M. Di Castro, L. Buonocore, E. Matheson, and A. Masi, Robotic solutions for the remote inspection and

maintenance of particle accelerators, in *Proceedings of the International Particle Accelerator Conference, Venice, Italy, May 2023* (JACoW, Geneva, Switzerland, 2019), pp. 3916–3919, 10.18429/JACoW-IPAC2023-THOGA2.

[206] The SoLID Collaboration, SoLID (Solenoidal Large Intensity Device) Updated Preliminary Conceptual Design Report, 2019 (unpublished), https://hallaweb.jlab.org/12GeV/SoLID/files/solid-precdr-Nov2019.pdf.

[207] S. Adhikari *et al.*, Strange hadron spectroscopy with secondary K_l beam in hall D (2019), https://www.jlab.org/exp_prog/proposals/19/KLF_47.pdf.

[208] H. Wang, G. Cheng, F. Hannon, A. Hofler, R. Kazimi, J. Preble, and R. A. Rimmer, RF design optimization for new injector cryounit at CEBAF, in *Proceeedings of the 7th International Particle Accelerator Conference, IPAC-2013, Shanghai, China* (JACoW, CERN, Geneva, Switzerland, 2013), pp. 2471–2473, http://accelconf.web.cern.ch/IPAC2013/papers/wepwo073.pdf.

[209] G. Cheng, M. Drury, J. Fischer, R. Kazimi, K. Macha, and H. Wang, JLAB new injector cryomodule design, fabrication and testing, in *Proceedings of the 18th International Conference on RF Superconductivity, SRF-2017, Lanzhou, China* (JACoW, Geneva, Switzerland, 2017), pp. 158–162, http://accelconf.web.cern.ch/srf2017/papers/mopb045.pdf.

[210] P. A. Adderley, J. Clark, J. Grames, J. Hansknecht, K. Surles-Law, D. Machie, M. Poelker, M. L. Stutzman, and R. Suleiman, Load-locked dc high voltage GaAs photogun with an inverted-geometry ceramic insulator, Phys. Rev. ST Accel. Beams **13**, 010101 (2010).

[211] G. Palacios-Serrano, F. Hannon, C. Hernandez-Garcia, M. Poelker, and H. Baumgart, Electrostatic design and conditioning of a triple point junction shield for a −200 kV DC high voltage photogun, Rev. Sci. Instrum. **89**, 104703 (2018).

[212] G. Palacios-Serrano, P. Adderley, J. Grames, C. Hernandez-Garcia, and M. Poelker, High-gradient Wien spin rotators at Jefferson Lab, in *Proceedings of the North American Particle Accelerator Conference, NAPAC'22, Albuquerque, NM* (JACoW Publishing, Geneva, Switzerland, 2022), pp. 662–664, https://doi.org/10.18429/JACoW-NAPAC2022-WEPA20.

[213] R. Kazimi, J. Spradlin, A.-M. Valente-Feliciano, O. Trofimova, and C. Reece, CEBAF chopper system, 2019 (unpublished).

[214] J. Hansknecht and M. Poelker, Synchronous photoinjection using a frequency-doubled gain-switched fiber-coupled seed laser and ErYb-doped fiber amplifier, Phys. Rev. ST Accel. Beams **9**, 063501 (2006).

[215] R. Kazimi, J. K. Spradlin, A.-M. Valente-Feliciano, O. Trofimova, and C. Reece, Kazimi 6-slit chopper, 2019 (unpublished).

[216] A. Freyberger, M. Bickley, R. Michaud, S. Suhring, K. Baggett, and A. Kimber, The 12 GeV CEBAF performance plan, Jefferson Lab Technical Note No. TN-17-022 (2017), https://jlabdoc.jlab.org/docushare/dsweb/Get/Document-139158/17-022.pdf.

[217] S. Henderson, CEBAF reliability plan FY18-21 (2018), Jefferson Lab internal document submitted to DOE, https://jlabdoc.jlab.org/docushare/dsweb/Get/Document-285823/18-060.pdf.

[218] R. Michaud, CEBAF Performance Plan Implementation Summary, Jefferson Lab Technical Note No. TN-20-012 (2020), https://jlabdoc.jlab.org/docushare/dsweb/Get/Document-211978/20-012.pdf.

[219] G. Ciovati, G. Cheng, E. Daly, G. Davis, M. Drury, J. Fischer, D. Forehand, K. Macha, F. Marhauser, E. McEwen, A. Mitchell, A. Reilly, R. Rimmer, and S. Wang, Cavity production and testing of the first C75 cryomodule for CEBAF, in *Proceedings of the 20th International Conference on RF Superconductivity, East Lansing, MI* (JACoW, Geneva, Switzerland, 2022), pp. 250–254, https://doi.org/10.18429/JACoW-SRF2021-MOPCAV001.

[220] J. Arrington, M. Battaglieri, A. Boehnlein, S. Bogacz, W. Brooks, E. Chudakov, I. Cloët, R. Ent, H. Gao, J. Grames, L. Harwood, X. Ji, C. Keppel, G. Krafft, R. McKeown, J. Napolitano, J. Qiu, P. Rossi, M. Schram, S. Stepanyan, J. Stevens, A. Szczepaniak, N. Toro, and X. Zheng, Physics with CEBAF at 12 GeV and future opportunities, Prog. Part. Nucl. Phys. **127**, 103985 (2022).

[221] J. Benesch, A. Bogacz, A. Freyberger, Y. Roblin, T. Satogata, R. Suleiman, and M. Tiefenback, 12 GeV CEBAF beam parameter tables, Jefferson Lab Technical Note No. TN-18-022 (2018), https://jlabdoc.jlab.org/docushare/dsweb/Get/Document-154003/18-022.pdf.

Correction: Multiple reference links have been corrected, enabling access to the cited articles.